Ref.:.......

Thesis presented to obtain the degree of

Doctorate in Physics

Option : **Renewable Energy and Materials Sciences**

Entitled:

Study of gallium-oxide-based ultraviolet photo-detectors

Presented by
CHERROUN RIMA

Publicly defended on:10/02/2025

In front of the Jury committee composed of:

SENGOUGA NOUREDINE	Professor	University of Biskra	President
MEFTAH AFAK	Professor	University of Biskra	Supervisor
MEFTAH AMJAD	Professor	University of Biskra	Examiner
OUSSALAH SLIMANE	Research Director	CDTA research center Algiers	Examiner

Academic Year: 2024/2025

Dedications

I dedicate this thesis to my family's unwavering support and
encouragement, whose love has been my constant source of strength.
To my parents, your sacrifices and belief in my abilities have shaped my
academic path.
To all my friends who encourage and support me, this thesis is a testament
to your invaluable role in my academic pursuit.
Your unwavering belief in my abilities and the countless moments of shared
enthusiasm have been instrumental in reaching this milestone.
I am deeply grateful for the friendship and laughter that have fueled my
journey.
This work is dedicated to the wonderful individuals who have stood by me,
providing strength and inspiration.
Thank you for being the pillars of support in my life.

Acknowledgments

Abstract

This study presents a numerical simulation of an IZTO/β-Ga$_2$O$_3$ Schottky barrier ultraviolet photodetector (SB UV-PhD), commonly referred to as a solar-blind UV photodetector, designed to operate specifically at a wavelength of 255 nm. The simulations were performed using SILVACO-ATLAS, a renowned 2D and 3D modeling software. Key parameters investigated include the current density–voltage (J–V) characteristics, responsivity, and internal quantum efficiency (IQE), with an additional focus on detectivity and time-dependent photo response (T-D PhR). The study is organized into two main parts. Initially, efforts were directed towards replicating experimental J–V characteristics under various conditions: in the dark and illuminated with wavelengths of 500 nm, 385 nm, and 255 nm. Notably, the influence of shallow and deep traps, particularly on persistent photoconductivity (PPC), was examined. The most significant impact was observed from the deepest traps ($E_T = 0.74 eV$ and $E_T = 1.04 eV$), which contributed to a decay time of 0.05 s. Moreover, incorporating an (Al$_{0.39}$Ga$_{0.61}$)$_2$O$_3$ passivation layer on the device's surface significantly enhanced its performance. In the second part of the study, further optimization was pursued by substituting the β-Ga$_2$O$_3$:Sn substrate with 4H-SiC and introducing a buffer layer between the β-Ga$_2$O$_3$:Si drift layer and the new substrate. Additionally, the top contact IZTO was replaced with Graphene, considering the effect of work function and electronic affinity. These optimizations yielded enhanced device metrics: a photocurrent density of $7.38 \times 10^{-5} A/cm^2$, responsivity of 0.074 A/W, IQE of 0.57, and detectivity of $5 \times 10^{12} Jones$ at - 1 V under 255 nm illumination. Furthermore, the device demonstrated robustness at elevated operating temperatures. In summary, this research not only simulated the performance of the IZTO/β-Ga$_2$O$_3$ SB UV-PhD under specific operating conditions but also explored significant enhancements through material and structural optimizations, thereby improving its overall photodetection capabilities.

Keywords: IZTO/β-Ga$_2$O$_3$, SB UV-PhD, numerical simulation, traps, the persistent photoconductivity phenomenon, passivation layer (Al$_{0.39}$Ga$_{0.61}$)$_2$O$_3$, buffer layer, 4H-SiC substrate, Graphene, Schottky contact, high operating temperature.

الملخص

هذه الدراسة تقدم محاكاة عددية لمستشعر الأشعة فوق البنفسجية من نوع IZTO/β-Ga$_2$O$_3$ بمبدأ حاجز شوتكي، المعروف أيضًا بالمستشعر الشمسي الأعمى، الذي يعمل تحت طول موجة ضوئي يبلغ 255 نانومتر. تمت المحاكاة باستخدام برنامج SILVACO-ATLAS المعروف بقوته في التصميم ثنائي وثلاثي الأبعاد. الخصائص الرئيسية المحسوبة شملت الخاصية كثافة التيار-الجهد(J−V) ، الاستجابية، والكفاءة الكمية الداخلية(IQE) ، بالإضافة إلى الكشفية و الإستجابة الضوئية بدلالة الزمن(T-D PhR). جُمِّعَت الدراسة إلى جزأين رئيسيين. في الجزء الأول، تم التركيز على إعادة إنتاج خصائص J−V التجريبية تحت ظروف مختلفة: في الظلام وتحت إضاءة بأطوال موجية 500 نانومتر، 385 نانومتر، و 255 نانومتر. وقد تم دراسة تأثير المصائد السطحية والعميقة، خاصة على الموصلية الضوئية المستمرة (الثابتة) (PPC) لوحظ تأثير كبير من المصائد الأعمق (E$_T$ = 0.74 إلكترون فولت و E$_T$ = 1.04 إلكترون فولت)، مما ساهم في زمن انحلال قدره 0.05 ثانية. علاوة على ذلك، تم تحسين أداء الجهاز بشكل كبير باستخدام طبقة تخميل (Al$_{0.39}$Ga$_{0.61}$)$_2$O$_3$) على السطح. في الجزء الثاني من الدراسة، تمت محاولة تحسين إضافي عن طريق استبدال المسند Ga$_2$O$_3$:Sn بمادة 4 H-SiC وإدخال طبقة بينية (بافر) بين طبقة الانجراف Ga$_2$O$_3$: Si و المسند الجديد. بالإضافة إلى ذلك، تم استبدال جهة الاتصال العلوية IZTO بالجرافين، مع مراعاة تفاصيل دالة العمل و الألفة الإلكترونية. هذه التحسينات أسفرت عن تحسين ملموس لمعايير الجهاز: كثافة تيار ضوئي تبلغ 7.38 × 10^{-5} أمبير/سم^2، استجابية تبلغ 0.074 أمبير/واط، كفاءة كمية داخلية تبلغ 0.57، وكشفية تبلغ 5 × 10^{12} جونز عند جهد 1 - فولت تحت إضاءة 255 نانومتر. علاوة على ذلك، أظهر الجهاز قدرة ممتازة على التحمل في درجات حرارة التشغيل العالية. باختصار، هذه الدراسة لم تقم بمحاكاة أداء جهاز IZTO/β-Ga$_2$O$_3$ SB UV-PhD تحت ظروف تشغيل معينة فقط، بل استكشفت أيضًا تحسينات كبيرة من خلال الأمثلة المادية والهيكلية، مما أدى إلى تحسين قدراتها الكاملة في الكشف عن الضوء.

الكلمات المفتاحية

IZTO/β-Ga$_2$O$_3$ ، كاشف ضوئي للأشعة فوق البنفسجية بحاجز شوتكي الشمسي الأعمى ، المحاكاة العددية ، المصائد ، الموصلية الضوئية المستمرة ، طبقة التخميل (Al$_{0.39}$Ga$_{0.61}$)$_2$O$_3$) ، الطبقة البينية ، الركيزة 4H-SiC ، الجرافين، إتصال شوتكي، درجة حرارة التشغيل العالية.

Table of Contents

List of Figures

List of Tables

List of Abbreviations

Abbreviations and Symbols	Description
DLTS	Deep-level transient spectroscopy
DLOS	Deep-level optical spectroscopy
EPR	Electron paramagnetic resonance
CZT	Czochralski technique
EFG	Edge-defined film-fed growth
VBG	Vertical Bridgman growth
FZT	Floating zone technique
PLD	Pulsed laser deposition
MOCVD	Metal organic chemical vapor deposition
MEB	Molecular beam epitaxy
ALD	Atomic layer deposition
HVPE	Halide vapor phase epitaxy
RF	Radio frequency
LED_S	Light-emitting diodes
PMT	Photomultiplier tube
SB UV phDs	Schottky barrier ultraviolet photodetectors
FETs	Field-effect transistors
SBDs	Schottky barrier diodes
MSM	Metal-semiconductor-metal
λ_0	Cut-off wavelength
I_{ph}	Photocurrent
I_{dark}	Dark current
R	Responsivity
IQE	Internal quantum efficiency

List of Abbreviations

τ_r	Rise time
τ_d	Decay time
D	Detectivity
NEB	Noise equivalent power
RRR	Response rejection ratio
PDCR	Photo-to-dark current ratio
EQE	External quantum efficiency
PPC	Persistent photoconductivity
ΔE	Carrier capture barrier
K_B	Boltzmann's constant
T	Temperature
MIGS	Metal-induced gap states
E_{CNL}	Energy of charge neutrality level
E_{FM}	Metal Fermi level
R_{cn}	Capture rate of electron
C_n	Capture coefficient of electron
N_T	Total concentration of trapping centers
E_T	Traps energy
σ_n	Capture cross section of electron
σ_p	Capture cross section of hole
$f_F(E_T)$	Fermi function at the trap energy (The probability of trap occupancy)
R_{en}	Emission rate of electron
E_n	Emission constant of electron
n_i	Intrinsic concentration
μ_o	Chemical potential
E^f	Formation energy
J_s	Saturation current density
R_s	Series resistance
η	Ideality factor
RT	Room temperature
q	Elementary charge

List of Abbreviations

D_n	Diffusion coefficient for electrons
D_p	Diffusion coefficient for holes
A^*	Effective Richardson's coefficient
$F_s(E')$	Maxwell-Boltzmann distribution of semiconductor
$F_m(E')$	Maxwell-Boltzmann distribution of metal
$\Gamma(E')$	Probability of tunneling
ϵ	Permittivity
ψ	Electrostatic potential
ρ	Space charge density
G_n	Generation rates for electrons
G_P	Generation rates for holes
n	Concentrations of electrons
p	Concentrations of holes
R_n	Recombination rates for electrons
R_P	Recombination rates for holes
μ_n	Electron mobility
μ_p	Hole mobility
$\vec{J}_n$	Electrons current density
$\vec{J}_p$	Holes current density
E_g	Band gap
χ_{sc}	Semiconductor electronic affinity
ΔE_c	Offset discontinuity at the bottom of the conduction band
ΔE_V	Offset discontinuity at the top of the valence band
E_F	Fermi energy
ϕ_M	Metal work function
SBH	Schottky barrier height
P_{OP}	Light power density
ϕ_B	Schottky barrier
N_C	Effective density of states for the edges of conduction band
N_V	Effective density of states for the edges of valance band
WBG	Wide band gap

List of Abbreviations

UWBG	Ultrawide band gap
SRH	Schottky Read Hall
BBT	Band to band tunneling
TEF	Thermionic field emission
FE	Field emission
TE	Thermionic emission
4H-SiC	Hexagonal silicon carbide
ITO	Indium tin oxide
IZTO	Indium zinc tin oxide
β-Ga$_2$O$_3$	Beta-gallium oxide
V_O	Oxygen vacancies
V_{Ga}	Gallium vacancies
DUV	Deep ultraviolet
UV	Ultraviolet
NIR	Near-infrared
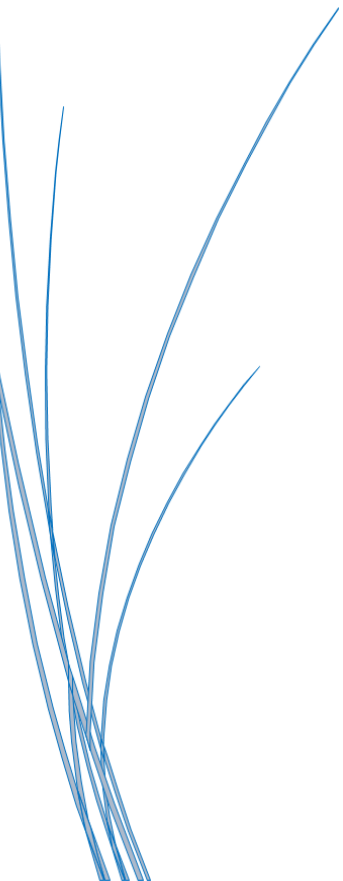
Introduction

Introduction

UV radiation has gained significant interest owing to its widespread application in civilian infrastructure, military settings, and scientific research [1]. As is widely known, the sun is the primary natural source of UV radiation, emitting UV rays across the entire wavelength spectrum. However, all UV radiation from the sun is absorbed by diatomic oxygen (100-200)nm or by ozone (triatomic oxygen) (200-280) nm present in the atmosphere. Therefore, the UV region with wavelengths (200-280) nm is a "solar-blind" zone, meaning it can be detected without the influence of solar radiation [2]. Detectors with a cut-off below 280 nm can be classified as solar blind since they exclusively detect UV radiation with wavelengths shorter than the solar energy that can pass through the Earth's atmosphere. If they are exposed to regular outdoor lighting, they do not generate any detectable signal. Highly stable and reliable DUV photodetectors that are insensitive to solar radiation have been widely used in a range of applications, including monitoring ozone depletion, flame detection, space communication, missile guidance, biochemical detection, and UV leakage inspection [2].

One benefit of WBG semiconductors, which encompass GaN (3.40 eV) [3], ZnO (3.29 eV) [4], ZnS (3.76 eV) [5], ZnSe (2.82 eV) [6], SiC (2.3-3.2) eV [7], AlN (6.20 eV) [8], diamond (5.5 eV) [9], BN (4.5-5.5) eV [10], and Ga_2O_3 (4.5-5.3) eV [11], (and their combinations for example $Al_xGa_{1-x}N$) [12], are that they can be transformed into solar-blind UV photodetectors. Furthermore, WBG materials are well-suited for applications that include high temperatures and high power [13]. Due to the high breakdown field strength, they are the most commonly used materials for photodetectors. Binary compound semiconductors such as GaN, SiC, and ZnO are well-suited for developing solar-blind UV photodetectors. These detectors need to have a larger responsivity in the UV region compared to lower energy ranges [2]. $Al_xGa_{1-x}N$ [14] and $Mg_xZn_{1-x}O$ [15], are WBG ternary semiconductor alloys utilized in developing solar-blind UV photodetectors, significant advancements have been made including the creation of a high-performance avalanche.

The challenges arise from the process of growing $Al_xGa_{1-x}N$ alloying films with high Al content, which necessitates a minimum growth temperature of 1350°C or higher [16], than $Mg_xZn_{1-x}O$, has a magnesium content exceeding 37%. This results in phase separation and a transition from the wurtzite structure to the rock salt structure. In addition, this will result

in the introduction of defects and dislocations in the vicinity of the separated domains, leading to a degradation in the performance of a detector [17]. Diamond being a UWBG semiconductor is a very promising material for the advancement of solar-blind UV photodetectors [18]. Nevertheless, the task of engineering E_g, in this basic semiconductor is challenging [9]. This limits its tunable photo-response spectral range. The absence of diamond bulk material in the form of large-area single crystals further impedes its practical utilization [19]. Ga_2O_3 is a potential contender for detecting solar radiation in the DUV range.

The material has a wavelength range of (258–280) nm and is anticipated to exhibit solar-blind sensitivity across the majority of the solar-blind UV area. Thanks to the presence of abundant Ga_2O_3 bulk single crystals of significant size [20], the optoelectronic potential of Ga_2O_3 in UV detection can be realized by the homoepitaxy development of epitaxial layers with high crystalline quality, specified doping, and E_g engineering [21].

H. Kim et al. have recently shown the successful development of entirely transparent β-Ga_2O_3 Schottky photodiodes utilizing a high-quality amorphous IZTO material as the Schottky contact and ITO material as the Ohmic contact [22]. The elevated work function of IZTO (4.9–6.1) eV [23] results in a substantial SBH, leading to a significant rectification ratio and minimal off-current, even without additional thermal treatment. The utilization of the linear facing target sputtering technique throughout the deposition process has resulted in the creation of a device that exhibits a consistently stable photo response performance. Due to their low dark current, quick photodetection, high responsivity, and self-powered nature [22].

This thesis aims to obtain the best fit to experimental measurements of an SB UV-PhD based on IZTO/β-Ga_2O_3/ITO by simulation using SILVACO-ATLAS and performing various optimizations to achieve optimal device performance.

The structure of this thesis is as follows:

Chapter 1: An overview of Ga_2O_3 properties.

This chapter comprehensively reviews the basic properties of Ga_2O_3, a promising material for various electronic and optical applications, especially in photodetectors and UV-sensitive devices. It covers the crystal structure, electrical, optical, and thermal properties of Ga_2O_3, with an overview of its native and extrinsic defects, as well as its most important deposition methods and various applications.

Chapter 2: Solar-blind ultraviolet photodetectors based on Ga_2O_3.

This chapter first reviews the classifications of photodetectors and their working principle. Focusing exclusively on photodetectors using Ga_2O_3, we will also discuss their limitations as photodetectors and suggest improvements that will help alleviate these limitations.

Chapter 3: Basics of Schottky device simulation by SILVACO-ATLAS.

This chapter provides a detailed introduction to the simulation of Schottky devices using the SILVACO-ATLAS software. It includes the theoretical background for simulating devices, how to use the software to determine device characteristics, and how factors like voltage difference and material properties affect the device performance. The chapter also covers how to simulate Schottky devices.

Chapter 4: Results and discussion.

This chapter presents and analyzes the results obtained from simulations, with emphasis on comparison with experimental results. With a discussion of the factors affecting efficiency and performance under different operating conditions.

Chapter 1: An overview of Ga$_2$O$_3$ properties

Chapter 1

An overview of Ga$_2$O$_3$ properties

1.1 Introduction

This chapter covers various aspects of Ga$_2$O$_3$, including its structural, electrical, optical, and thermal characteristics, as well as native and extrinsic defects, and Ga$_2$O$_3$ films deposition techniques. The chapter will conclude by highlighting key applications of Ga$_2$O$_3$, potential applications might include power electronics, UV photodetectors, gas sensors, high-power devices, and more, depending on the material's properties and performance.

1.2 History of Ga$_2$O$_3$

Ga$_2$O$_3$ has a history rooted in materials science and semiconductor research, with a growing emphasis on its potential for power electronics and related applications. Its unique properties and promising characteristics have made it a subject of considerable interest in the 21st century, and its development continues to evolve [24].

1.2.1 Discovery and early studies (1960s - 1990s)

Ga$_2$O$_3$ has been a familiar material with a long history spanning several decades. The discovery of the element Ga and its compounds can be attributed to the French scientist L. de Boisbaudran [24]. The beginning of Ga$_2$O$_3$ research goes back to R. Roy et al. who conducted an in-depth investigation of the phase equilibrium of the Al$_2$O$_3$-Ga$_2$O$_3$-H$_2$O system, which greatly advanced the understanding of this compound [25]. Expanding on his work in 1952, he confirmed the presence of five Ga$_2$O$_3$ polymorphs and provided insights into the relationships governing their stability [26]. Building on advancements, H. Tippins discerned E_g of 4.7 eV for bulk single crystals of Ga$_2$O$_3$ in 1965 by closely examining optical absorption and photoconductivity [27].

During the initial phases of Ga$_2$O$_3$ research, the primary focus was on fundamental char-

acteristics such as crystal structures, E_g, and N_C. Notably, scientific research from the 1960s to the 1980s frequently underscored the challenges of achieving high crystal quality, with many reports describing materials in suboptimal states, ranging from poor to amorphous forms [28].

1.2.2   Emergence of Ga$_2$O$_3$ (1990s - 2010s)

During the period spanning the 1990s to the 2010s, there were remarkable strides in the successful growth of high-quality, large-sized Ga$_2$O$_3$ bulk single crystals. One noteworthy achievement was the realization of a substantial Ga$_2$O$_3$ single crystal measuring 70 $mm{\times}50mm{\times}3mm$ through the EFG method, this accomplishment solidified EFG as one of the most promising techniques for large-scale production [29].

Utilizing the FZT, researchers successfully grew large single crystals of Ga$_2$O$_3$ with an impressive diameter of 1 in. The establishment of stable growth conditions was achieved through a thorough examination of the crystal structure [30]. Also, The CZT has enabled the commercial production of sizable β-Ga$_2$O$_3$ bulk crystals and wafers, reaching sizes of up to 2 in. and 4 in. respectively [31].

The presence of expansive substrates has, in turn, stimulated advancements in the homoepitaxy growth of top-tier Ga$_2$O$_3$ thin films. This progress involves a more sophisticated control over parameters such as doping, defects, modulation doping, Superlattice structures, and other intricate factors [21]. The growth of large-size bulk crystals has spurred research into Ga$_2$O$_3$ based devices, including FETs [32], SBDs [33], and solar-blind UV photodetectors [34]. In that particular era, researchers were able to cultivate high-quality epitaxial thin films of Ga$_2$O$_3$, which played a pivotal role as integral elements within more sophisticated devices [35]. Furthermore, the rapid strides in science and technology have not only propelled the growth techniques and fundamental attributes of diverse Ga$_2$O$_3$ nanomaterials but have also significantly expanded their applications in various devices. This surge in progress is underscored by their nano-scale size in at least one dimension [36].

1.2.3   Commercial and industrial interest (2010s - present)

In recent years, Ga$_2$O$_3$ has attracted attention from the electronics industry and government agencies due to its potential in power electronics. Power electronic devices made from Ga$_2$O$_3$ are envisioned to be more energy-efficient and capable of handling higher voltages and temperatures [37]. Various research groups and companies have been working on device prototypes and exploring applications in fields like electric vehicles, renewable energy, and defense technologies. Research on Ga$_2$O$_3$ continues to expand, focusing on improving material quality, and device performance, and finding new applications [38, 39].

1.3   Fundamental properties of Ga$_2$O$_3$

1.3.1   Structural properties

Ga$_2$O$_3$ exhibits various polymorphs, denoted as α, β, γ, δ, ε, and κ. The polymorphs exhibit variations in both the coordination number of Ga ions and the crystal space groups. Under specific conditions, Ga$_2$O$_3$ can be formed in any of these phases. The first polymorph, α-Ga$_2$O$_3$, adopts a rhombohedral structure with the space group R$\bar{3}$c. It shares a corundum-like arrangement with Al$_2$O$_3$. Synthesis of this polymorph involves heating GaO(OH) in air within the temperature range of 450 to 700°C [26].
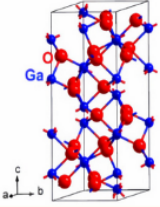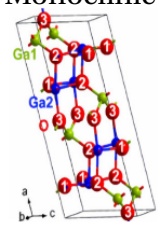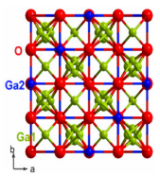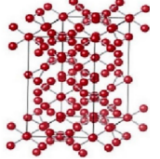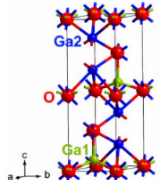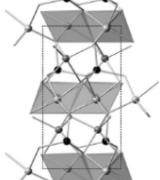
The monoclinic structure of the second polymorph, β-Ga$_2$O$_3$ falls under the space group C2/m. This particular phase can be achieved by subjecting any other polymorph of β-Ga$_2$O$_3$ in the air to a sufficiently high temperature. It holds significance for researchers due to its stability under ambient conditions [39].

There is a consensus that the third polymorph, γ-Ga$_2$O$_3$, adopts a defective cubic spinel-type structure akin to MgAl$_2$O$_4$, characterized by the Fd$\bar{3}$m space group. The process for preparing this polymorph is relatively straightforward, involving the oxidation of Ga in amino alcohol, such as ethanolamine [39].

The fourth and fifth polymorphs, referred to as δ-Ga$_2$O$_3$ (cubic) and ε-Ga$_2$O$_3$ (orthorhombic), were initially synthesized and elucidated by R. Roy et al [26]. Initially, the polymorph δ-Ga$_2$O$_3$ structure was mistaken for ε-Ga$_2$O$_3$ phase, assumed to be a nano-crystalline form of ε-Ga$_2$O$_3$. However, subsequent confirmation revealed that it is not a nanostructure or an alternate phase but rather a distinct cubic structure. On the other hand, ε-Ga$_2$O$_3$ can maintain stability under high-pressure conditions. Additionally, upon heating, it can transform into the α phase, and notably, it exhibits ferroelectric properties [39].

There's also mention of a transient κ-Ga$_2$O$_3$ orthorhombic polymorph, following successive solvothermal oxidation reactions, a novel oxyhydroxide Ga$_5$O$_7$(OH) emerges. The thermal decomposition of this compound reveals another previously undocumented Ga$_2$O$_3$ polymorph, the transient κ-Ga$_2$O$_3$ [40]. Indeed, the fluctuations in lattice parameters are pivotal in shaping the overall structure of the material. Given the inherently 3D nature of κ-Ga$_2$O$_3$ structures, the increase in lattice parameters expands the realm of potential structures. However, it's crucial to recognize that not all of these structures endure as stable configurations. The dynamic interplay of lattice parameters contributes to the nuanced landscape of stable and unstable configurations within the diverse polymorphs of Ga$_2$O$_3$ [39]. Table 1.1 presents the different polymorphs and crystal structures of Ga$_2$O$_3$.

Table 1.1: Various polymorphs of Ga_2O_3 and their corresponding crystal structures.

Polymoraph	Structure	Space group	Lattice parameter	Refs
α	Rhombohedral	$R\bar{3}c$	a=b=4.9825 Å c=13.433Å	[40]
β	Monoclinic	C2/m	a=12.214Å b=3.0371Å c=5.7981Å β=103.83°	[41]
γ	Cubic	$Fd\bar{3}m$	a=8.22Å	[42]
δ	Cubic	$Ia\bar{3}$	a=9.491Å	[43]
ε	Orthorhombic	$P6_3mc$	a=2.9036 Å c=9.2554 Å	[44]
κ	Orthorhombic	$Pna2_1$	a=5.0463 Å b=8.7020 Å c=9.2833 Å	[44]

The transition to β-Ga$_2$O$_3$ occurs at temperatures exceeding 500°C, as illustrated in Figure 1.1. R. Roy et al. were pioneers in delineating all the polymorphs of Ga$_2$O$_3$ in their research, including providing insights into their respective stabilities [26].
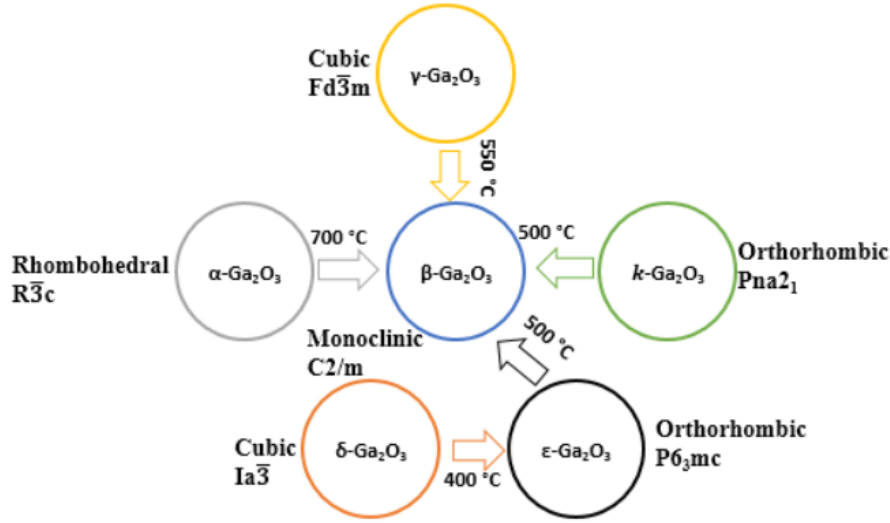
Figure 1.1: Characterization of Ga$_2$O$_3$ crystal phases and their transformation conditions [26].

1.3.2 Electrical properties

1.3.2.1 Electronic structure

Until now, numerous theoretical studies have been released regarding the electrical structure of β-Ga$_2$O$_3$. In the mentioned studies, the DFT approach was employed. Where DFT modeling can provide a satisfactory qualitative explanation of the electronic structure. However, it often tends to underestimate the values of E_g. The underestimation of E_g values in DFT is attributed to its foundation in ground state theory, leading to an undervaluation of the exchange-correlation potential between excited electrons [45]. Hybrid DFT was employed to achieve more precise results that facilitate the generation of data for structure, energetics, and E_g aligns much more accurately with experimental observations [46, 47]. The findings from various studies consistently showed that in β-Ga$_2$O$_3$ the CBM was located at the Γ point, and the valence band exhibited a nearly flat profile [47] as shown in Figure 1.2.

However, there was a lack of consensus among researchers regarding the exact position of the VBM. Nonetheless, the precise location of the valence band has minimal impact on the E_g size due to the limited dispersion of the valence band, as elucidated by H. He et al [48]. The VBM in β-Ga$_2$O$_3$ is nearly degenerate at both the Γ and M points, with the energy at Γ being 0.03 eV lower than that at M. Conversely, the CBM is situated at Γ resulting in a direct gap of 4.69 eV at Γ and an indirect gap of 4.66 eV at M. The limited strength of indirect transitions and the slight energy difference between indirect and direct gaps effectively categorize

β-Ga$_2$O$_3$ as a direct-gap material. This is consistent with the experimentally observed sharp absorption onset at approximately 4.9 eV [47, 48].
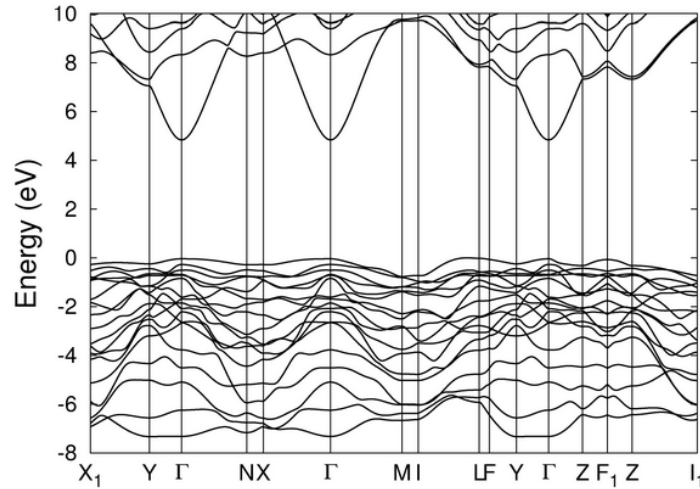
Figure 1.2: The band structure for β-Ga$_2$O$_3$ is calculated using the primitive unit cell of the base-centered monoclinic [47].

1.3.2.2   Controlling conductivity and doping

Ga$_2$O$_3$ is inherently categorized as an insulator due to its WBG, when subjected to synthesis under reducing conditions it displays strong n-type conductivity. It is widely understood that the presence of ionized V_O acting as donors is responsible for the manifestation of n-type semi-conductivity in such cases [49]. By adjusting the oxygen content in the growth atmosphere, the conductivity of β-Ga$_2$O$_3$ crystals can be precisely adjusted within a range of 10^{-9} to 38 $(\Omega.cm)^{-1}$. Interestingly, the conductivity shows an upward trend with lower oxygen content. However, it's noteworthy that the growth becomes unstable under conditions of reduced oxygen [50].

Z. Galazka et al. noted a comparable relationship between the growth conditions and conductivity in Ga$_2$O$_3$ crystals produced via the CZT . The prevalence of V_O was often considered the primary factor behind the n-type conductivity in Ga$_2$O$_3$ crystals [51]. On the other hand, J. B. Varley et al. confirmed the opposite. Their research highlights that V_O is not responsible for the n-type conductivity of β-Ga$_2$O$_3$ [52]. Those who conducted first-principle calculations using the hybrid DFT on various impurities and V_O in β-Ga$_2$O$_3$ have contested this assumption. These calculations demonstrate that V_O does not contribute to n-type conductivity because it is a deep donor with ionization energies greater than 1 eV. According to the authors, hydrogen is most likely to be blamed for the electrical conductivity of accidentally doped Ga$_2$O$_3$ [48].

Doping has a profound influence on the electrical conductivity and free electron concentration of Ga$_2$O$_3$ crystals. Introducing elements from group IV such as Si, Ge, and Sn

which can replace Ga in specific structures, can significantly impact the electrical properties. Similarly, group VII elements like Cl and F, acting as shallow donors, contribute to the modulation of electrical characteristics when they substitute at the O site. It seems that coordination preferences play a significant role in doping dynamics. Si, and Ge, for instance, favor the tetrahedral coordination of the Ga (1) site, while Sn specifically leans towards the octahedral coordination of the Ga (2) site. On the other hand, both F and Cl exhibit a preference for the triple coordination of the O (1) site [52].

N. Suzuki et al's. work on the development of Sn-doped Ga_2O_3 crystals in the FZT provides intriguing insights, using Ga_2O_3 rods doped with 2–10 $mol\%$ SnO_2 in the FZT procedure resulted in the creation of highly conductive crystals, where despite the crystals growing in an oxygen atmosphere, they exhibited conductivity values of 0.96 $(\Omega.cm)^{-1}$ [53]. It's interesting to note the challenges encountered in the crystal development process. The vaporization of a significant portion of Sn atoms from the feed rods during crystal growth resulted in a relatively low integration efficiency. Despite this, the remaining Sn atoms proved adequate to sustain a concentration of free electrons in the mid-10^{18} cm^{-3} range. The mobility in this study exhibited a range from 50 to 100 $cm^2/V.s$ [54].

Si emerges as another potential donor impurity in Ga_2O_3, the significant atomic radius difference of around 40% between Si^{4+} and Ga^{3+} distinguishes it from the relative atomic radii differences between Ge^{4+} and Sn^{4+} which are -16% and +14%, respectively. Interestingly, Ge^{4+} and Sn^{4+} fit more seamlessly into the Ga^{3+} cationic site when considering the atomic radius. However, Si, despite its larger atomic radius difference, can be considered an n-type dopant in crystals produced from melt. Unlike Ge and Sn, this is attributed to its advantage of not readily evaporating [52, 55].

The work by E. G. Víllora et al. concentrates on Si-doped Ga_2O_3 crystals created through the FZT, they developed feed rods by sintering a mix of SiO_2 and Ga_2O_3 powders with Si concentrations ranging from 0 to 0.2 $mol\%$, the resulting β-Ga_2O_3 single crystals exhibited Si concentrations between 10^{16} and 10^{18} cm^{-3}. Interestingly, nearly all of the Si is incorporated into the crystal at low doping levels, but at higher levels, the Si concentration in the crystal is only about 5% of that in the feed rod. The crystals' conductivity steadily increased with rising Si concentration in the feed rod, ranging from 0.03 $(\Omega.cm)^{-1}$ for undoped crystals to 50 $(\Omega.cm)^{-1}$ for highly doped ones. Although the mobility fluctuated around 100 $cm^2/V.s$.The free-carrier concentration systematically increased with Si concentration by over three orders of magnitude, reaching 10^{16} to 10^{18} cm^{-3} [54]. This experimental evidence, demonstrating the correlation between Si doping and electrical conductivity, challenges the notion that ionized V_O is the primary contributor. The alignment of these findings with theoretical calculations confirms [55].

Mg doping appears to induce the formation of insulating β-Ga_2O_3 crystals, as evidenced

by various publications. X. Feng et al. utilized the FZT approach to generate crystals of Mg-doped β-Ga$_2$O$_3$, the samples, with an Mg content ranging from 4×10^{18} to 10^{19} cm^{-3}, exhibited a semi-insulating tendency and a resistivity of 6×10^{11} $\Omega.cm$. Not ably, Mg is also employed as a compensatory acceptor in this context. Additionally, the introduction of Mg doping was observed to contribute to stabilizing growth and diminishing the likelihood of spiral formation. The impact of high Mg doping on Ga$_2$O$_3$ films is quite intriguing, the E_g of Ga$_2$O$_3$ films produced via MOCVD on MgO substrates experiences a monotonic increase with the escalation of Mg content, where observed optical E_g of 4.93, 5, 5.09, 5.21, and 5.32 eV for Ga$_2$O$_3$ films doped with 1, 3, 5, 7, and 10% of Mg, respectively. This systematic variation in E_g highlights the tenability of material properties through controlled doping, offering avenues for tailored applications [56].

The quest for p-type conductivity in Ga$_2$O$_3$ continues, and it seems like there's an interesting twist in the study. L. Liu et al. report that nitrogen-doped Ga$_2$O$_3$ nanowires exhibit p-type conductivity, this adds more complexity to the discussion on Ga$_2$O$_3$'s conductivity characteristics and opens up new possibilities for its application in electronic devices [57].

Z. Wu et al. theoretical modeling provides valuable insights into the behavior of nitrogen as a dopant in Ga$_2$O$_3$. Their findings suggest that nitrogen introduces a shallow acceptor impurity level, and the Fermi level intersects with it near the CBM [58]. This alignment of energy levels sheds light on the potential for nitrogen to act as a p-type dopant in Ga$_2$O$_3$ supporting the experimental observations of p-type conductivity in nitrogen-doped Ga$_2$O$_3$ nanowires [59].

Theoretical simulations often serve as critical tools in understanding material properties, and in the case of Ga$_2$O$_3$, some simulations suggest that achieving p-type conductivity might be inherently challenging. The high self-localization of holes, influenced by the iconicity of metallic oxides, is identified as a significant factor, this phenomenon adds a layer of complexity, making it difficult for carriers to move freely and contribute to p-type conductivity. If substitution doping is successful, for example, a positive hole localizes on a single oxygen atom and remains immobile inside the crystal lattice even when an electric field is applied [58]. The anticipation of very low hole mobility on the scale of 10-6 $cm^2/V.s$ at RT suggests a considerable challenge in achieving appreciable p-type conductivity in Ga$_2$O$_3$. The limitation posed by the low mobility implies that even if holes could be introduced into Ga$_2$O$_3$ their ability to contribute significantly to p-type conductivity would be hindered. This aligns with the theoretical simulations indicating attaining p-type conductivity proves challenging due to the elevated self-localization of holes [50].

1.3.3 Optical properties

In its stoichiometric form without impurities, β-Ga$_2$O$_3$ is colorless and displays excellent transparency reaching into the UV-C (280-200) nm range of the light spectrum due to its WBG [60, 61]. Colorless or mildly yellowish hues characterize insulating β-Ga$_2$O$_3$ crystals, this correlation was attributed to minimal absorption in the blue region of the visible spectrum. Conversely, n-type conductive crystals exhibit a bluish tint due to heightened absorption of free carriers in the red and NIR bands. The absorption in the red and NIR ranges is linked to conduction electron plasma absorption. Additionally, impurities, notably carbon, contribute to a greyish tint [51, 62]. As shown in Figure 1.3.

Figure 1.3: Colorless characterize insulating β-Ga$_2$O$_3$ crystals (on the right), while those containing carbon impurities exhibit a gray color (in the middle), conductive n-type β-Ga$_2$O$_3$ crystals display a bluish hue (on the left) [51].

Figure 1.4 illustrates the transmittance spectra of the insulating sample doped with Mg and samples doped with Sn at various concentrations. The sample featuring low electron concentration displays a distinct absorption edge at (255-260) nm and nearly total transparency in the NIR wavelength range, as the free electron concentration increases transmittance decreases at visible and NIR wavelengths. The absorption spectra typically show a shoulder around 270 nm and a pronounced absorption edge at approximately (255-260) nm. The transition from the valence band to the conduction band is the fundamental reason behind the observed absorption at (255-260) nm [51, 62].

In Figure 1.5, the absorption spectrum of β-Ga$_2$O$_3$ at RT is depicted, upon the tangent intersecting the energy scale (the black line) it becomes evident that the optical Eg of β-Ga$_2$O$_3$ is approximately 4.73 eV in the ($\bar{2}$01) direction, as elucidated by N. Ueda and colleagues [63].
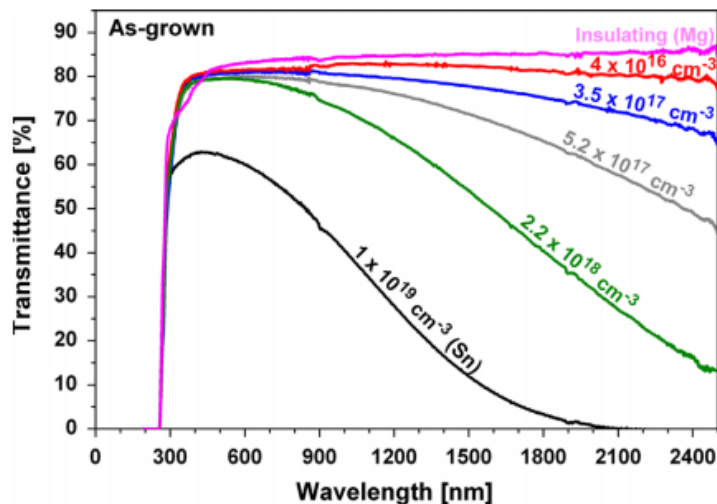
Figure 1.4: The transmittance spectra of single crystals of β-Ga$_2$O$_3$ grown using the CZT are presented for an insulating sample doped with Mg and samples doped with Sn with different free electron concentrations [51].
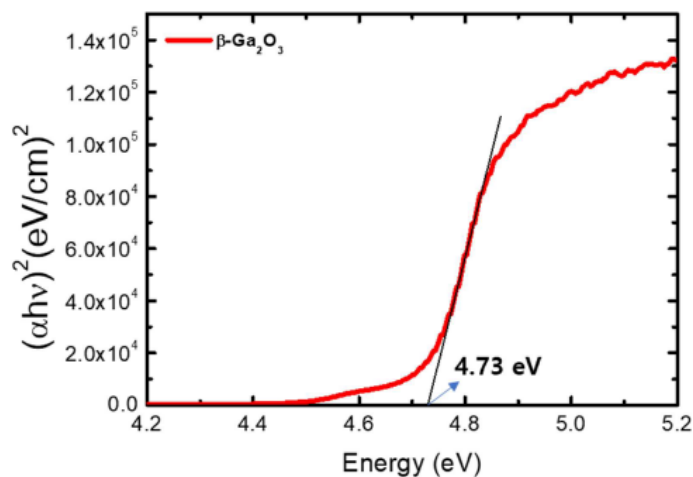
Figure 1.5: Absorption spectrum of β-Ga$_2$O$_3$ at RT [63].

1.3.4 Thermal properties

In the realm of semiconductors, β-Ga$_2$O$_3$ stands out for its comparatively low heat conductivity, its thermal conductivity is approximately one order of magnitude lower than that of GaN and roughly half that of Al$_2$O$_3$. The thermal conductivity in β-Ga$_2$O$_3$ shows significant variation along different crystal orientations attributable to crystallographic anisotropy, They are measured using laser flash methods and are specifically determined along the [100] direction to be 13 W/mK [64], and 21 W/mK along the [010] direction [65].

$$K(T) = AT^m \tag{1.1}$$

15

The equation(1.1) represents the temperature dependence of thermal conductivity. In the lower temperature range (80-200)K the exponent "m" is approximately 3.5, while in the higher temperature range (200-495)K it is around 1.2 [49]. At lower temperatures, the thermal conductivity of β-Ga₂O₃ diverges from the expected $T^{-\frac{3}{2}}$ temperature dependency showing that free electron scattering as well as phonon scattering limit heat conduction [64, 65].

1.4 Overview of Ga₂O₃ defects

This section specifically examines the native defects and extrinsic defects (impurities) in Ga₂O₃ that could have an impact on its electrical and optical characteristics.

1.4.1 Native defects in Ga₂O₃

1.4.1.1 Oxygen vacancies

In oxide semiconductors, a missing oxygen atom or V_O is hard to detect, perhaps because of this elusiveness V_O often gets blamed for unintentional n-type conductivity. Most of the information we have for V_O in Ga₂O₃ comes from DFT, this "first-principles" technique calculates quantities based on the electron density distribution and positions of the nuclei. Recently, hybrid DFT has been employed to obtain reasonably accurate energy levels and E_g. To compute the V_O formation energy, the initial step involves determining the total electron energy (comprising potential and kinetic energy) of the intrinsic semiconductor after removing the oxygen atom and placing it in the reservoir. The energy of V_O is acquired by considering in μ_0. The E^f is then calculated as the energy difference between a substance containing one defect and a pure (intrinsic) substance. The magnitude of q for the defect is pivotal, when $q = 1$ it signifies that the defect has supplied one electron to the reservoir, with the energy of this electron aligning with E_F. Conversely, if $q = 2$ the defect has contributed two electrons [66].

In the broader context, the E^f is influenced by q contributing a term of qE_F. When all factors are accounted for, the E^f is computed as a composite of these diverse elements [66].

$$E^f = E(Ga_2O_3 : V_O) - E(Ga_2O_3) + \mu_0 + qE_F \tag{1.2}$$

Where $E(Ga_2O_3 : V_O)$ and $E(Ga_2O_3)$ are the calculated energies for the defective and pure semiconductor, respectively. These energies are relative to VBM. According to the research conducted by J. B. Varley et al. the value of the E^f is around 3.5 eV. A decrease in E^f leads to an increase in the concentration of V_O [52].

1.4.1.2 Gallium vacancies

Considered V_{Ga} are common defects in Ga$_2$O$_3$, given that Ga possesses three valence electrons, the absence of Ga atom results in three O dangling bonds capable of accepting electrons. This is significant as V_{Ga} can act as compensators for donors, thereby reducing the concentration of free electrons. B. E. Kananen et al's. calculations indicate that the Ga(1) vacancy has a lower E^f compared to Ga(2) [67].

1.4.1.3 Native deep traps

The identification of several deep-level states in both bulk crystals and thin films of β-Ga$_2$O$_3$ has been accomplished through the utilization of DLTS and DLOS, as well as a combination of other techniques and DFT calculations. K. Irmscher et al. utilized DLTS to identify three deep trap states in undoped β-Ga$_2$O$_3$ crystals formed using the CZT, these trap states are E_1, located at an energy level of 0.54 eV below the conduction band ($E_c - 0.54eV$), E_2 at 0.72 eV below the conduction band ($E_c - 0.72eV$), and E_3 at 1.04 eV below the conduction band ($E_c - 1.04$ eV). The E_2 trap with a concentration ranging from 2 to 4×10^{16} cm^{-3} is present in all samples and has a dominant effect. E_3 is detected in select samples processed under certain conditions exhibiting a concentration similar to that of E_2. The concentration of E_1 is one order of magnitude lower than that of E_2 and E_3, ranging from 3×10^{14} to 6×10^{15} cm^{-3}, the deep-level states can function as compensatory acceptors. Further research is needed to determine the precise microscopic and chemical characteristics of the deep-level states. However, K. Irmscher et al. suggested that transition metal impurities, specifically Fe^{3+} and Co^{2+}, could potentially account for certain deep traps, this hypothesis is supported by the detection of Fe^{3+} and Co^{2+} in their samples using EPR [68].

1.4.2 Extrinsic defects in Ga$_2$O$_3$

1.4.2.1 Shallow donors

Considered Si, Sn, and Ge are all shallow donors [52]. In this case, we will take Si as an illustrative example, with its four valence electrons, Si replaces trivalent Ga, resulting in Si$_{Ga}$ gaining one additional valence electron compared to the Ga it replaces. The extra electron orbits the positively charged Si$_{Ga}$ impurity, showing behavior similar to the Bohr model of the hydrogen atom. The energy needed to release this electron is called E_d and its estimation follows the principles described in the Bohr model [69].

$$E_d = 13.6(\frac{m^*}{m})(\frac{1}{\varepsilon^2}) \tag{1.3}$$

Where $\frac{m^*}{m} \approx 0.28$ and the relative dielectric constant is $\varepsilon \approx 11$ [69], inserting those values

into equation (1.3) yields $E_d \approx 30\ meV$. In an energy-level diagram as shown in Figure 1.6, the (0/+) donor level is represented as a horizontal line denoted as E_d positioned just below CBM, given its proximity to the CBM is categorized as a shallow donor.
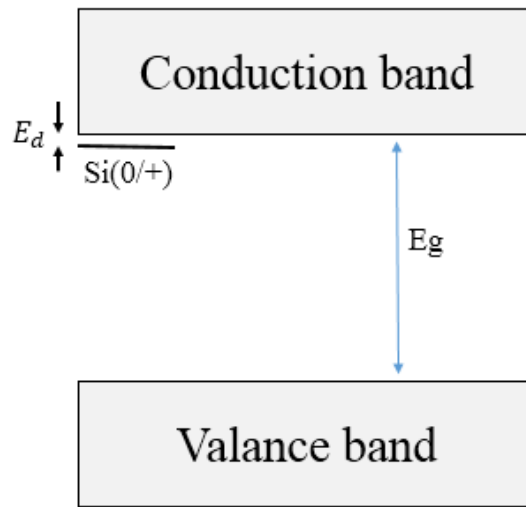
Figure 1.6: The anticipated energy level for a chosen Si impurity in Ga$_2$O$_3$ [52].

Targeted Si doping can result in free electron concentrations in the range of 10^{16} to 10^{18} cm^{-3}, this intentional introduction of Si contributes significantly to the electrical properties of the material [70]. Based on previous studies, it has been observed that Si and Ge show a preference for the Ga (1) site, while Sn tends to occupy the Ga (2) site, this insight into site preferences contributes to a better understanding of crystalline arrangements in the material [51]. In the bulk form of Ga$_2$O$_3$, Zr classified as a transition metal, assumes the role of a shallow donor. This implies that it readily contributes electrons to the material, impacting its electrical characteristics [71].

1.4.2.2   Deep acceptors

Mg stands out as a potential dopant for semi-insulating Ga$_2$O$_3$, occupying a Ga (2) site, with two valence electrons one less than Ga, and Mg functions as an acceptor [72]. The acceptor level is determined to be deep situated $1.0-1.5\ eV$ above VBM [56]. In the case of neutral Mg, the hole is highly localized, being situated on an O (1) atom adjacent to Mg [73], where found that bulk crystals can incorporate high concentrations of Mg (10^{18}–10^{19}) cm^{-3} surpassing compensatory donors. This proves highly advantageous for the semi-insulating material, although achieving p-type conductivity becomes impractical due to the deep nature of the acceptor [56].

1.5   Growth mechanisms in Ga$_2$O$_3$

Intriguingly, bulk single crystals of Ga$_2$O$_3$ can be created without the necessity for elevated pressures. The process involves melting Ga$_2$O$_3$ powder in a heated iridium crucible using the CZT by immersing a seed crystal into the melt and gradually lifting it, leading to the cooling of the melt and the formation of crystals, rotation of the seed and/or crucible helps in the development of a symmetric cylindrical ingot. Optimal O$_2$ partial pressure is maintained by using a CO$_2$ and O$_2$ mixture during growth to prevent breakdown. Common impurities such as Ga and O vacancies, as well as Ir, Fe, and Si, are often present in CZT grown Ga$_2$O$_3$ [31]. In the EFG, the second technique involves utilizing a die with a slit, capillary action comes into play as the liquid Ga$_2$O$_3$ film is pulled through the slit when the die is submerged in the melt. This process initiates cooling, leading to the crystallization of the material [29].

The specific configuration of the slit pattern is instrumental in shaping the final form of the alloy [29]. During VBG, the crucible and starting powder experience a thermal gradient. With the temperature increasing, crystal formation takes place as a consequence of the solid-liquid interface gradually moving upward when the crucible is lowered Ga$_2$O$_3$ produced in a Pt-Rh crucible in the surrounding air containing Si, Pt, and Rh impurities within the (1-10) ppm range [74]. In FZT the procedure commences with a polycrystalline rod subjected to melting via halogen heating lamps. Vertical translation of the rod ensues allowing the molten zone to traverse its length ultimately yielding single-crystal Ga$_2$O$_3$. Crystals produced using this method often exhibit free-electron densities of approximately 10^{17} cm^{-3} a characteristic likely linked to the presence of Si impurities [30]. Figure 1.7 shows a schematic representation illustrating different techniques employed in the growth of Ga$_2$O$_3$ crystals.
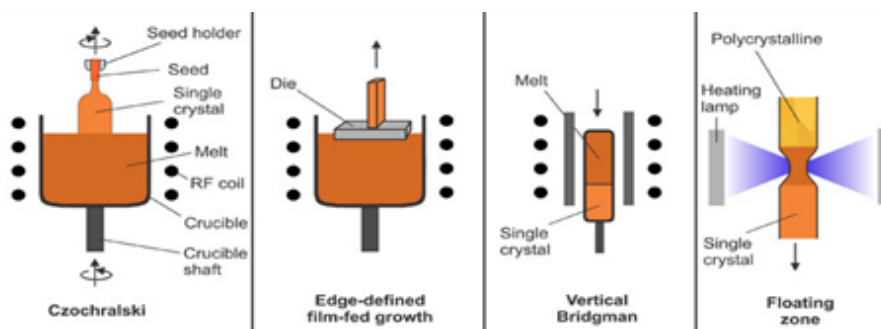
Figure 1.7: Techniques for the bulk crystal growth of Ga$_2$O$_3$ [75].

Different approaches have been utilized in the production of Ga$_2$O$_3$ thin films, with sputtering being a notable technique among them, this cost-effective method utilizes an Ar$^+$ plasma to dislodge, or sputter, atoms from a Ga$_2$O$_3$ target [76]. PLD the application of a high-intensity laser for ablating target atoms has also been employed in the fabrication of Ga$_2$O$_3$ thin films [77]. Epitaxial growth is typically not achieved through sputtering or PLD. Epitaxy is the process wherein a crystalline film forms on a crystalline substrate establishing precise

atomic bonds between the film and substrate, growing Ga$_2$O$_3$ on Ga$_2$O$_3$ substrates where single-crystal substrates can be created is known as homoepitaxy. On the other hand, when Ga$_2$O$_3$ is grown on a different substrate, such as Al$_2$O$_3$ it is an example of heteroepitaxy [78]. Within the realm of epitaxial growth techniques, MOCVD takes precedence, this method initiates with the deployment of organometallic compounds, encompassing Ga, O, and other crucial elements, serving as the customary starting molecules or precursors. This meticulous approach ensures a controlled and precise deposition of crystalline films on a crystalline substrate [79]. Within epitaxial growth methodologies, MBE shines as an ultrahigh-vacuum technique renowned for its unparalleled precision in controlling atomic layers. The vacuum environment plays a pivotal role in facilitating the seamless transit of atoms from source to substrate devoid of collisions that might compromise the exactness of the deposition process. This meticulous approach underscores MBE's capability to deliver finely tuned and well-defined crystalline films on substrates [80].

1.6 The most important applications of Ga$_2$O$_3$

Ga$_2$O$_3$ finds diverse and crucial applications across various fields, with notable uses including:

➢ **Power electronics:** Ga$_2$O$_3$ revolutionizes power electronics with its remarkable breakdown voltage. Its expansive E_g and elevated critical electric field render it well-suited for managing high voltages, a pivotal attribute for power applications involving transistors and diodes. This feature not only boosts the efficiency of these devices but also paves the way for creating sturdier and high-performance power electronic systems [81].

➢ **UV optoelectronics:** Ga$_2$O$_3$'s optical characteristics make it well-suited for use in optoelectronic devices like LEDs and solar-blind UV photodetectors [82].

➢ **Cas sensors:** Ga$_2$O$_3$ finds application in sensor technologies, specifically in the realm of gas sensors and environmental monitoring [83].

➢ **Solar cells:** The semiconductor properties of Ga$_2$O$_3$ contribute to its use in solar cell technology, aiding in efficient energy conversion [84].

➢ **Catalysis:** Ga$_2$O$_3$ finds application as a catalyst in certain chemical processes [85].

➢ **Scintillators:** Ga$_2$O$_3$ is explored for scintillation applications, such as radiation detectors in medical imaging [86].

➢ **High-frequency devices:** The high electron mobility of Ga$_2$O$_3$ makes it a key player in the advancement of high-frequency devices, particularly in the realm of RF components. The concept of electron mobility revolves around the velocity at which electrons can traverse

a material when subjected to the influence of an electric field [87].

➢ **Thin-film coatings:** Ga$_2$O$_3$ is utilized for thin-film coatings, providing protective and functional layers in various applications [88].

➢ **Transparent conductive films:** Ga$_2$O$_3$'s thin films find application in transparent conductive coatings, serving purposes such as touchscreens and solar cells [89].

Chapter 2: Solar-blind UV photodetectors based on Ga$_2$O$_3$

Chapter 2

Solar-blind UV photodetectors based on Ga$_2$O$_3$

2.1 Introduction

More than 99% of the solar radiation spectrum lies within the wavelength range of 150 to 4000 nm, and roughly 7% of notable wavelengths are found in the UV spectral region. The UV light region is further categorized into distinct segments: UVA (400-320) nm, UVB (320-280) nm, UVC (280-200) nm, UVD (200-100) nm, and UVV (100-10) nm [90]. The solar-blind UV ray is characterized by its specific wavelength range which spans from 200 to 280 nm [91].

The inherent advantages of solar-blind UV photodetectors technology, such as low background noise, high sensitivity, and robust anti-interference capabilities, indicate its potential application in the emerging era of short-distance communication [92]. Moreover, the potential of solar-blind UV photodetectors technology extends to critical areas of everyday life, including power grid safety monitoring, medical imaging, life sciences, and environmental and biochemical testing [93].

Continued research and development have focused on identifying materials suitable for constructing solar-blind UV photodetectors. Notably, studies consistently highlight Ga$_2$O$_3$ as a prime choice. The excellent electrical and optical properties of Ga$_2$O$_3$ contribute to devices with reduced conduction loss and enhanced power conversion efficiency, this positions them favorably for applications in high-voltage and high-power devices, indicating a promising future in these fields [94].

In this chapter, we will first define the classifications of photodetectors and generally explain their working principle and the basic parameters that control photodetector performance. After that, our focus will be exclusively on photodetectors using Ga$_2$O$_3$, delving into their diverse configurations. In addition, we will briefly discuss recent research results regarding the classification of Ga$_2$O$_3$-based photodetectors, we will also discuss its constraints

as a photodetector and propose enhancements that help mitigate these constraints.

2.2 Classification of UV photodetectors and its working principle

Photodetectors can be broadly classified into two classifications. The first classification encompasses detectors that rely on the external photoelectric phenomenon, in this type photons trigger the photocathode generating photoelectrons which are then captured by an external anode. This operational principle is commonly found in vacuum tube photodetectors, notably in devices like photomultipliers, where amplification plays a crucial role. The second classification of photodetectors these devices operate on the internal photoelectric phenomenon, in this type the absorption of electromagnetic radiation initiates the release of electrically charged particles specifically electrons and holes within a material [95].

The second classification encompasses solid-state detectors crafted from materials like Si, as well as detectors constructed using WBG semiconductors such as AlGaN and SiC. Within this realm, photovoltaic detectors utilize various structures like P-N junctions, Schottky barriers, or MSM junctions. These structures establish an electrical field that effectively separates the generated electron-hole pairs resulting in the generation of a photocurrent importantly. The magnitude of this photocurrent is directly linked to the intensity of the incident radiation providing a quantitative measure of the detected light [95]. Figure 2.1 shows the classification of UV photodetectors.
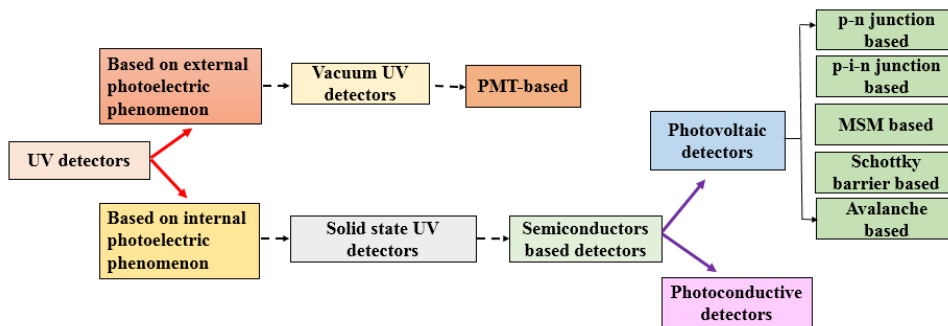
Figure 2.1: Classification of UV photodetectors [96].

2.2.1 Photodetectors based on external photoelectric phenomenon

2.2.1.1 Photo emissive detector (vacuum UV detector)

The photoelectric effect is observed when a photocathode is illuminated by optical radiation, electrons are emitted from the photocathode if the incoming photons possess sufficient

kinetic energy to surpass the vacuum-level barrier. Once this threshold is exceeded the electrons gain the freedom to leave the photocathode and become free electrons. When there's a significant electric field between the cathode and anode in a photoelectric phenomenon the emitted electrons experience acceleration as they move toward the anode, this acceleration results in a photocurrent essentially a flow of electrons that is proportional to the intensity of the incident photons, the higher the intensity of the incoming light the greater the number of photons and consequently the higher the photocurrent produced [95].

This relationship between the intensity of light and the generated photocurrent is a key aspect of the photoelectric effect. The PMT is a fascinating device that amplifies the detection of light signals, where photo-emitted electrons from the photocathode are accelerated and directed toward a series of dynodes, these dynodes are electrically biased to create an electron multiplication cascade through a process known as secondary emission. As the primary photo-emitted electrons strike the first dynode, they release several secondary electrons. Each of these secondary electrons then goes on to impact the next [95]. Figure 2.2 shows the structure and energy band diagram of the photo emissive detector.
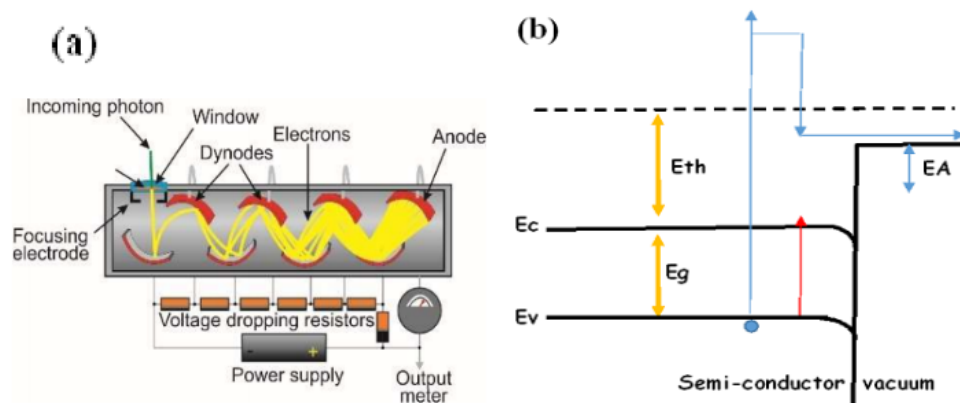
Figure 2.2: **(a)** Photo emissive detector structure. **(b)** Energy band diagram of photo emissive detector [95].

2.2.2 Photodetectors based on internal photoelectric phenomenon

2.2.2.1 Solid state UV detectors (semiconductors based photodetectors)

a. Photoconductor detector

Operating as an optical radiation-sensitive photoresist, it generates electron-hole pairs in a consistent semiconductor material when exposed to incident radiation, spanning the E_g directly, the spectral response is intricately tied to this E_g. Concurrently, in a connected process, a quantum-well photoconductor triggers the excitation of elec-

trons or holes from the potential well within the semiconductor's E_g regions [97]. Figure 2.3 shows the structure and energy band diagram of the photoconductor detector.
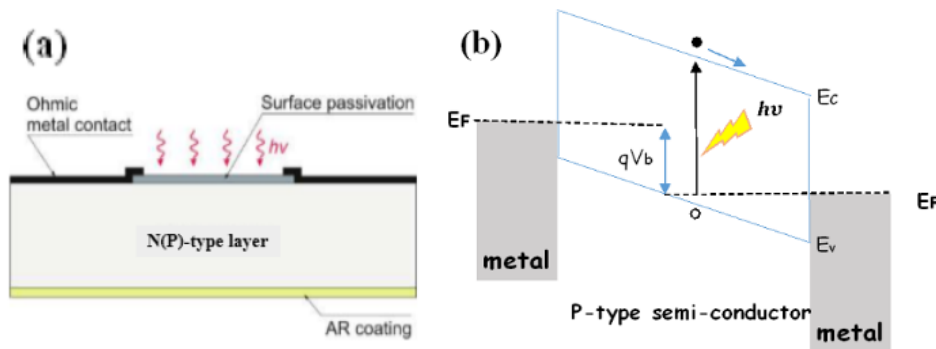
Figure 2.3: **(a)** Photoconductor detector structure. **(b)** Energy band diagram of photoconductor detector [95].

b. Photovoltaic detector

• P–N junction photodetector

It's a commonly employed photodetector commonly found in a standard P-on-N setup, featuring a shallowly diffused P-region on the N-type active layer. Alternatively, there's an available N-on-P structure. The mechanism involves an electric field segregating photo-induced electron-hole pairs on both sides of the junction within the space charge region, this segregation results in a photocurrent that, in turn, modifies the open-circuit junction voltage or the short-circuit junction current [94]. Figure 2.4 shows the structure and energy band diagram of the P–N junction photodetector.
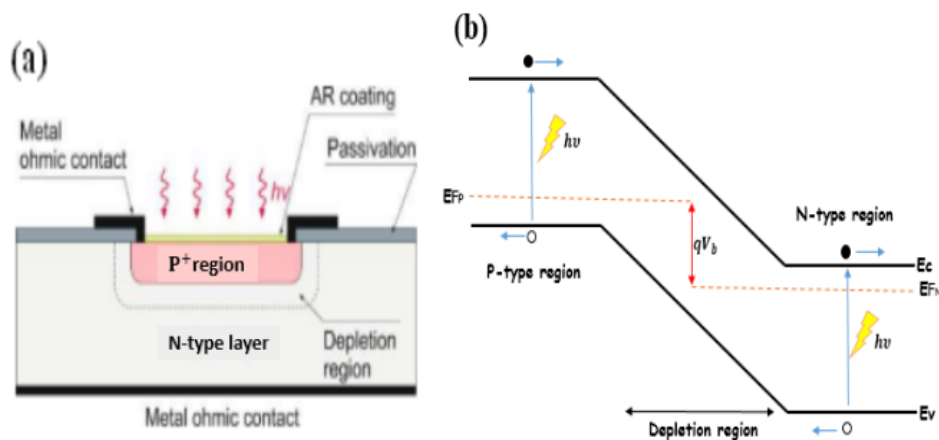
Figure 2.4: **(a)** P–N junction photodetector structure. **(b)** Energy band diagram of P–N junction photodetector [95].

- **P-I-N junction photodetector**

  In the P-I-N configuration, the photodetector follows a standard structure with an intrinsic I-region strategically placed between the P and N sides of the junction. The depletion region spans the entire intrinsic volume when subjected to a reverse bias voltage, it's crucial to note that incident photons only trigger electron-hole pair generation within this depletion region. The absence of an electrically neutral volume leads to zero diffusion current in the device, and the dark current is then formed by minority carriers generated through defect centers within the diode's depletion region [94]. Figure 2.5 shows the structure and energy band diagram of the P-I-N junction photodetector.
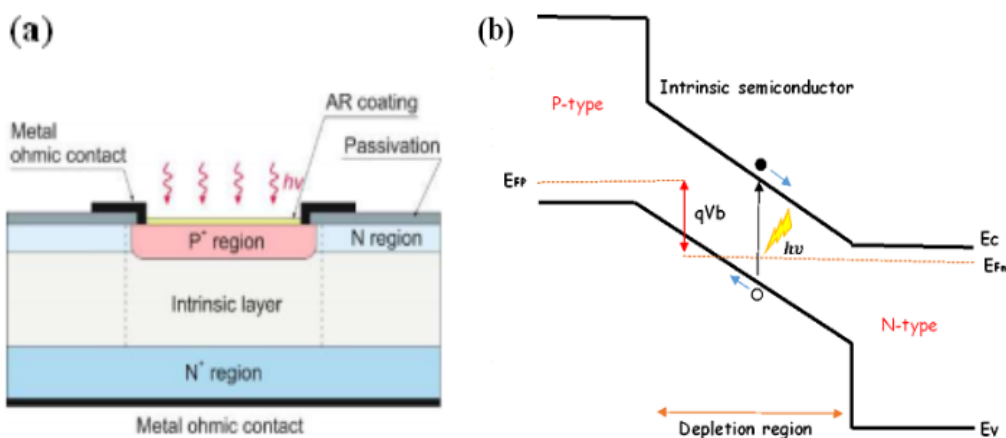
Figure 2.5: **(a)** P-I-N junction photodetector structure. **(b)** Energy band diagram of P-I-N junction photodetector [95].

- **Schottky barrier photodetector**

  This device predominantly carrying majority carriers takes shape at the junction where metal meets semiconductor. Analogous to the P-N junction this juncture establishes a potential barrier that effectively segregates photo-excited electron-hole pairs within the semiconductor or at the interface of metal and semiconductor. Contrasted with a P-N photodetector a Schottky barrier photodetector boasts certain advantages, these include the ease of fabrication achieved by depositing the metal barrier onto the N (P) semiconductor, utilization of lower-temperature diffusion processes, and a heightened reaction rate. However, it's essential to note that a Schottky junction is generally marked by a more substantial dark current [96]. Figure 2.6 shows the structure and energy band diagram of the Schottky barrier photodetector.
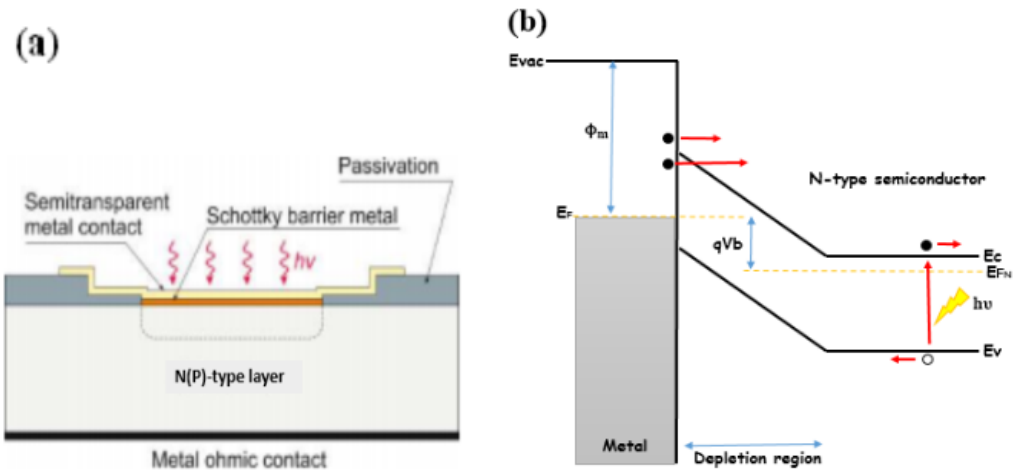
Figure 2.6: **(a)** Schottky barrier photodetector structure. **(b)** Energy band diagram of Schottky barrier photodetector [95].

- **MSM photodetector**

  The MSM photodiode structure resembles the interdigitated photoconductor, where Schottky barriers form the M/S junctions instead of using Ohmic contacts. The manufacturing process closely mirrors the steps employed for crafting FETs, yielding a planar structure with integrated MSM photodetectors functionality. Noteworthy advantages of this design include a reduced dark current when contrasted with an SBD and a swifter response speed compared to a P-I-N photodetector. This intricate yet efficient configuration showcases the continuous evolution of photodetector technology [95]. Figure 2.7 shows the structure and energy band diagram of the MSM photodetector.
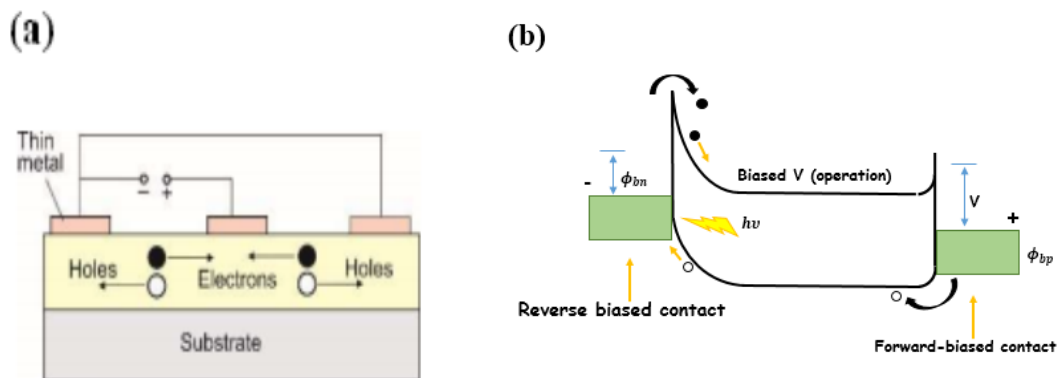
Figure 2.7: **(a)** MSM photodetector structure. **(b)** Energy band diagram of MSM photodetector [95].

- **Avalanche photodetector**

  The avalanche photodetector is specially crafted to identify minute traces of radiation, its N$^+$-N$^-$-P structure features meticulously regulated doping profiles and a well-designed geometry ensuring a consistent electric field streamlines the manufacturing process, under a substantial reverse bias, a depletion layer spans the N$^+$-N$^-$ region, while photon absorption takes place in the P region. The applied electric field impels minority carrier electrons, generated at the periphery of the depletion region by incident light, to collide with the crystal lattice, triggering a cascade of ionization and an avalanche effect [95].

  This phenomenon introduces fresh carriers, resulting in a rapid surge of reverse currents. Consequently, the avalanche photodetector exhibits a remarkable synergy of swift responsiveness, heightened sensitivity, and exceptional quantum efficiency making it a standout in its class [95]. Figure 2.8 shows the structure and energy band diagram of the avalanche photodetector.
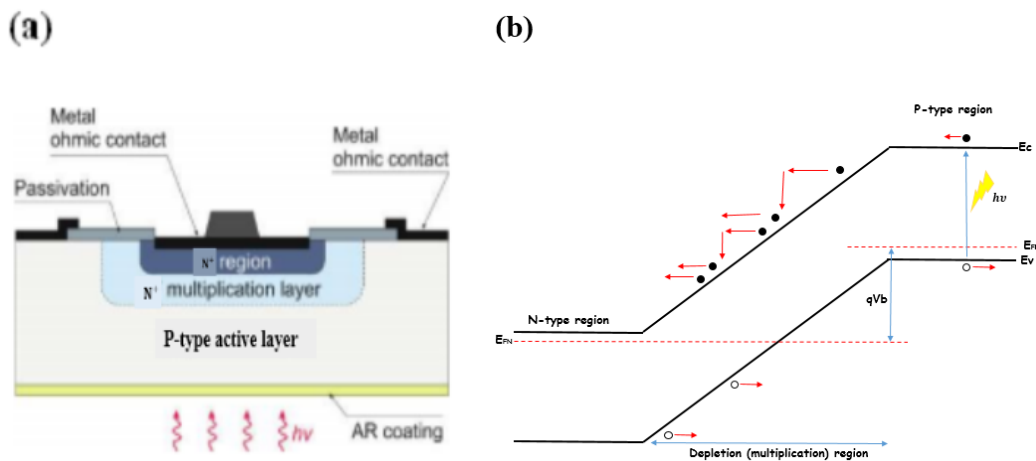
Figure 2.8: **(a)** Avalanche photodetector structure. **(b)** Energy band diagram of avalanche photodetector [95].

2.3 Primary parameters of UV photodetectors

To evaluate the performance of any device, specific parameters are necessary. For a photodetector, the value of the following characteristics determines its performance [98–104]:

➢ **Cut-off wavelength** λ_0**:** The maximum wavelength λ_0 that the UV detector can detect, as indicated in equation (2.1), can be determined through absorption and transmittance spectra. Here, h represents Planck's constant, c is the speed of light, and E_g denotes the band gap.

$$\lambda_0 = \frac{hc}{E_g} \tag{2.1}$$

➤ **Photocurrent I_{ph}:** It is the external circuit current that can be examined under different biases by performing I-V measurements in the presence of UV light. This comprehensive testing provides insights into photodetector performance across a range of operating conditions.

➤ **Dark current I_{dark}:** This refers to the residual current flowing through the detector when there is no incident light.

➤ **Responsivity R:** It is the effectiveness of the photodetector in converting incident light into an electrical signal. This efficiency is expressed as the ratio of the generated photocurrent to the incident light power by relationship:

$$R = \frac{I_{ph}}{P_{op}} \tag{2.2}$$

Where I_{ph} and P_{op} are the photocurrent at a given voltage, and the light power density, respectively.

➤ **Internal quantum efficiency IQE:** Each incident UV photon attempts to create an electron-hole pair; however, the actual number of generated electron-hole pairs is typically less than the number of photons. Where the IQE is defined as the yield of carriers per absorbed photon.

$$IQE = R_\lambda \frac{hc}{q\lambda g} \tag{2.3}$$

Where R_λ, h, c, q, λ_0 are the responsivity, Planck's constant, speed of light, electronic charge, and wavelength of the incident light, respectively and g is the gain is the number of carriers passing contacts per one generated pair.

➤ **Response time:** The time it takes for the detector output to change in response to variations in input light intensity is referred to as its photo response or response time. This parameter is typically evaluated through two distinct components: the rise time (τ_r) and the decay time (τ_d). The rise time denotes the duration for the photodetector output level to transition from 10 to 90% of the peak output level, while the decay time represents the duration for the output level to shift from 90 to 10% of the peak output level. Alternatively, response time can be determined by fitting the photo response with a suitable function that includes rise and decay time constants. This measurement is expressed in seconds.

➤ **Detectivity D:** This parameter essentially measures the signal detection capability relative to the inherent noise in the detector. The expression for D in equation (2.4) provides a quantitative representation of this characteristic, shedding light on the detector's sensitivity and performance in discerning weak signals amidst background noise.

$$D = \sqrt{\frac{A_{op}}{2qI_{dark}}} R_{\lambda} \tag{2.4}$$

In the given formula, A_{op} represents the effective area under illumination, I_{dark} is the dark current, q is the electronic charge, and R_{λ} is the responsivity. Detectivity is commonly measured in $Jones$ (or $cm\sqrt{HZ}W^{-1}$).

➤ **Noise equivalent power NEP:** She represents the optical input power at which the signal-to-noise ratio equals one. In situations where detector performance is influenced by background radiation and thermal generation is significantly lower than the background level, the NEP under these conditions is expressed as:

$$NEP = \frac{\sqrt{A_{op}\Delta f}}{D} \tag{2.5}$$

Where A_{op} is the effective radiation area of detectors, Δf is the frequency bandwidth, and D is detectivity.

➤ **Response rejection ratio RRR:** This parameter is for comparing the response at different wavelengths, also called wavelength rejection ratio, and is a measure of how well a photodetector responds to light at a specific wavelength compared to another. The formula for RRR is:

$$RRR = \frac{Responsivity UV}{Responsivity Visible} \tag{2.6}$$

Where $Responsivity UV$ and $Responsivity Visible$ are the responsivity of the photodetector at UV wavelength and the visible wavelength, respectively.

A high RRR indicates that the photodetector is more responsive to UV light compared to visible light. This parameter is important in applications to detect or selectively filter light for a specific wavelength range.

2.4 Development of UV detector materials

Historically, the exploration of materials for solar-blind UV photodetectors has primarily concentrated on single crystal thin films including SiC [105], diamond [106], AlN [107], and GaN [108]. However, the attainment of detectors based on these materials is hindered by technical complexities, particularly in achieving top-notch single crystals. Additionally, challenges may arise due to high costs and limited economic benefits, or when E_g falls short of the ideal range, leading to the coverage of only specific bands in solar-blind UV photodetectors [105–108]. Presently, research on materials for solar-blind UV photodetectors is predominantly centered on specific WBG semiconductors renowned for their sensitivity to the solar-blind ultraviolet spectrum, and the most important of them $Al_xGa_{1-x}N$ [109], $Mg_xZn_{1-x}O$ [110], Ga_2O_3 [111–113].

2.4.1 Ga_2O_3 solar-blind UV photodetectors

a. Photoconductor UV detectors based on Ga_2O_3

Among all types of detectors, photoconductor detectors garner the most comprehensive study focus owing to their practicality and convenience. P. Feng et al. employed the evaporation technique to cultivate Ga_2O_3 nanowires on Si substrates that were coated with a 10 nm Au layer, N_2 gas was used as a carrier in the process, and the entire procedure occurred at a temperature of 980°C for one hour. Next, a nanowire of about 50 nm in thickness was positioned on the Au electrode to form the structural arrangement of the Au–Ga_2O_3–Au photodetector. The device's dark current was measured to be approximately $10^{-12}A$ when subjected to 254 nm UV light the photocurrent experienced a three-fold rise, shifting from the pA range to the nA range. The rise time was 0.22s, whereas the decay time, was 0.09s [114].

In 2016, X. Liu et al. utilized Ga vapor in a conventional closed Knudsen cell (K cell) and injected monoatomic oxygen to deposit Ga_2O_3 films. To improve the device's performance, they integrated a self-assembling buffer layer while growing the Ga_2O_3 films, utilizing Au/Ti as the electrodes. The detector exhibited excellent performance characteristics, with a notable picture responsivity of 259 A/W and an amazing EQE of 7.9×10^4 %, and exhibits a low dark current of $10^{-11}A$, and a high PDCR of 10^4 [115]. In the growth process, achieving high-quality Ga_2O_3 single crystals poses a technical challenge due to issues related to dislocations and polycrystallization [29].

Q. Feng et al. utilized the EFG process, employing 99.99% pure Ga_2O_3 as the raw material. They achieved successful growth of large Ga_2O_3 crystals on an intrinsic Ga_2O_3 bulk substrate with a (100) orientation and performed a comparative examination with

Ga$_2$O$_3$ crystals produced on sapphire substrates. The experimental findings showed that the former had a much higher responsivity (0.05 A/W) compared to the latter (0.009 A/W) at a bias voltage of $40V$. Simultaneously, the response times exhibited similarity, with the former being $0.45s/0.24s$ and the latter being $0.40s/0.18s$. After conducting a thorough comparison, it was determined that Ga$_2$O$_3$ crystals produced on homogenous substrates exhibited greater performance [116].

b. Photovoltaic UV detectors based on Ga$_2$O$_3$

- **P-N junction UV photodetectors based on Ga$_2$O$_3$**

  Once the identification of Ga$_2$O$_3$ as the N-type material was established, the subsequent phase was the selection of the P-type material. Over time, extensive research has been conducted on potential P-type materials, with a notable focus on compounds like GaN [117], SiC [118], Si [119], ZnO [120], Graphene [121], diamond [122], MoS$_2$ [123]. P. Li et al. utilized PLD technology to apply a Ga$_2$O$_3$ layer onto a 4 mm thick Mg-doped P-type GaN film in their work. Afterward, they proceeded to create electrodes utilizing In/Ag materials, when no external bias was applied, the results were remarkable; a responsivity of 54.43 mA/W, a decay time of $0.08s$, a PDCR of 152, and a detectivity of $1.23 \times 10^{11} cm\sqrt{HZ}W^{-1}$ [124].

  B. Zhao et al. fabricated ZnO-Ga$_2$O$_3$ core-shell heterostructure microwires and converted them into photodiodes by aligning Ga$_2$O$_3$ along the (201) lattice plane. Their objective was to mitigate flaws occurring at the interface between the two materials, ultimately improving the performance of the photodetectors. The researchers utilized a simple one-step CVD technique in their study. The responsivity measured at 251 nm under zero bias was 9.7 mA/W and the UV/visible rejection ratio (R_{251nm}/R_{400nm}) was measured as 6.9×10^2, and the rise/decay time was found to be less than 100 ms /900 ms [34].

  Y. C. Chen et al. took a pioneering approach by integrating diamond as a P-type material. They successfully achieved the homogeneous expansion of diamond wafers on (100) diamond surfaces inside a high-temperature and high-pressure setting. Afterward, researchers used a plasma-enhanced CVD device to apply a layer of Ga$_2$O$_3$ onto the diamond wafer, resulting in the creation of a diamond/Ga$_2$O$_3$ heterojunction. At a bias of 0 V, the heterojunction exhibited a maximum responsivity of 0.2 mA/W, with a cut-off wavelength of 270 nm and the UV/visible rejection ratio surpassed 100-fold, emphasizing the strong self-powered solar-blind UV sensing capabilities of this heterojunction [122].

- **P-I-N junction UV photodetectors based on Ga₂O₃**

  Solar-blind UV P-I-N detectors have been successfully manufactured by researchers through meticulous fabrication efforts. Y. An et al. utilized L-MBE technology to fabricate a P-Si/N-Ga₂O₃ heterojunction and a P-Si/I-SiC/N-Ga₂O₃ heterojunction, they conducted a thorough performance analysis to compare the two heterojunctions. To improve the quality of the P-Si/I-SiC/N-Ga₂O₃ heterojunction, the research team made deliberate adjustments to the oxygen pressure during the retreat phase, resulting in a significant reduction in V_O levels. The meticulous tuning led to notable outcomes, as the rectification ratio of the P-Si/I-SiC/N-Ga₂O₃ heterojunction achieved an amazing value of 36 at 4.5 V. Unlike the P-Si/N-Ga₂O₃ heterojunction, the P-Si/I-SiC/N-Ga₂O₃ heterojunction showed a significant decrease in dark current by a factor of 1000. In addition, the rectification behavior experienced a significant change transitioning from reverse to forward. Furthermore, the photosensitivity achieved a value of 5.4×10^5% when exposed to 254 nm light at - 4.5 V [125].

- **Schottky barrier UV photodetectors based on Ga₂O₃**

  T. Oshima et al. employed POEDT-PSS to form a Schottky contact with the high-resistance layer of semi-Ga₂O₃. An electrically non-conductive layer was used to separate this contact from a low-resistance connection that connected the N-type Ga₂O₃ to two electrodes on the back side of the substrate. The device demonstrated an impressive rejection ratio (R_{250nm}/R_{300nm}) of around 1.5×10^4 at wavelengths. In addition, the IQE at a wavelength of 250 nm achieved an estimated value of 18% [126].

  X. Chen et al. used Ga metal as a starting material to produce arrays of Ga₂O₃ nanowires through a straightforward thermal oxidation procedure. To enhance the structure they applied a 20 nm thick layer of Au onto the nanowires creating photodetectors with a vertical configuration of Au/Ga₂O₃ nanowires in a Schottky-type arrangement. The device exhibited a cut-off wavelength of roughly 270 nm for photoresponsivity with the highest photo-responsivity at 258 nm and 0 V which was measured to be 0.01 mA/W, the device demonstrated a rapid response time, with a rise time of around 1 ms and a decay time of approximately 64 ms [127].

  Most Schottky barriers work under bias to achieve higher performance. In previous research, there were cases where researchers replaced the metal in the Schottky junction, exploring alternative materials for improved performance or spe-

cific functionalities we take examples of this: Au [128], Ni [129], Graphene [121], Pt [130].

T. Oshima et al. conducted a study in which they fabricated Schottky-type solar-blind UV detectors utilizing a single crystal of Ga$_2$O$_3$ oriented along the (100) direction. The procedure commenced by subjecting Ga$_2$O$_3$ single crystals to thermal annealing to stabilize surface V_O and create a layer with high electrical resistance. Subsequently, scientists utilized Au/Ni and Au/Ti electrodes in the front and back to create Schottky and Ohmic contacts, respectively. The strategic approach was crucial in developing an optimized configuration for solar-blind photodetectors. The photodetector demonstrated a rectification ratio of 10^6 at -3V, demonstrating a substantial DUV photoelectric response when exposed to reverse bias. In addition, the photo-responsivity of the photodetector varied from 2.6 to 8.7 A/W when it was exposed to wavelengths ranging from 200 to 260 nm, this confirms the device's efficacy in detecting and reacting to DUV radiation [131].

- **MSM UV photodetectors based on Ga$_2$O$_3$**

S. Oh et al. illustrated the exceptional capabilities of MSM solar-blind photodetectors, through the integration of β-Ga$_2$O$_3$ microlayers with Graphene. Graphene chosen for its dual transparency to DUV light and conductivity played a crucial role as the electrode in this study. Despite the inherent challenges of MSM-structured photodetectors, such as typically low responsivity, the combination of β-Ga$_2$O$_3$ and Graphene electrodes resulted in remarkable features. These included a significantly elevated responsivity $\approx$ of 29.8 A/W, an impressive PDCR $\approx$ 1×10^6, a high rejection ratio of $R_{254nm}/R_{365nm} \approx$ 9.4×10^3, and detectivity $\approx$ 1×10^{12} $Jones$, and swift operating speed in the UV-C wavelength range. These measurements surpassed the performance of conventional MSM photodetectors equipped with standard metal electrodes. The deliberate integration of Graphene with β-Ga$_2$O$_3$ ensures minimal shading, and maximized exposure to incident photons, highlighting its tremendous potential for applications in DUV optoelectronics [132].

T. Oshima et al. presented findings on MSM Ga$_2$O$_3$ photodetectors, crafted by applying a thin β-Ga$_2$O$_3$ layer onto sapphire substrates through molecular beam spectroscopy, for the metal-semiconductor DUV photodetector, Ti/Au electrodes (50nm/100nm) were deposited to establish ohmic contacts. The device exhibited a minimal dark current of 1.2 nA at a bias voltage of 10 V, upon exposure to 254 nm light the current witnessed an increase, and the resultant photo responsivity

stood at 0.037 A/W, corresponding to an IQE of 18% [133].

- **Avalanche UV photodetectors based on Ga$_2$O$_3$**

  To address the problem of weak solar-blind signals, it is crucial to create solar-blind avalanche photodiodes that possess significant internal avalanche gain. X. Chen et al. described the process of producing α-Ga$_2$O$_3$ thin films with a single crystal structure on the nonpolar ZnO (11$\bar{2}$0) crystal plane using molecular laser beaming, they then designed a high-performance diode called a Schottky barrier avalanche diode, which used a heterojunction structure consisting of Au/α-Ga$_2$O$_3$/ZnO [134].

  The device demonstrated its ability to generate its power by producing a small electric current at the pA level with no applied voltage, it also exhibited an excellent ability to reject unwanted UV/visible light with a rejection ratio of 10^3. Additionally, it showed a high detectivity of 9.66×10^{12} $cm\sqrt{HZ}W^{-1}$. When a bias voltage of -5 V was applied the detector operated as a device that responded to two different wavelengths of light, it showed the highest sensitivity at wavelengths of 255 nm and 365 nm, with corresponding values of 0.50 A/W and 0.071 A/W, respectively. When exposed to a bias of - 40 V the device exhibited a significant increase in electrical current due to the avalanche effect, it achieved an impressive photo-responsivity of 1×10^4 A/W when exposed to 254 nm DUV light, surpassing a total gain of 10^5 [134].

2.4.2 Comparison of UV detectors and their parameters based on Ga$_2$O$_3$ with different configurations (The most recent research)

Recent advancements in UV detectors based on Ga$_2$O$_3$ have focused on optimizing device performance across several configurations, including photoconductive, Schottky junction, and PN junction detectors. The following table (Table 2.1) summarizes key metrics from recent research, showcasing improvements in responsivity, response time, and wavelength range for different Ga$_2$O$_3$ based UV detectors.

These configurations demonstrate how recent research has achieved significant improvements in detector performance, particularly in terms of responsivity and response times. The advancements highlight the versatility of Ga$_2$O$_3$ as a material for UV detection, with each configuration offering unique advantages depending on the specific application.

These studies indicate that while Ga$_2$O$_3$ based UV detectors are highly promising, ongoing research is crucial to optimize material growth techniques and device architectures to fully exploit their potential in various UV detection applications [2, 36, 94].

Table 2.1: Illustrates a comparison of the latest research on UV detectors and their standards based on Ga_2O_3 with various configurations.

Type configuration	Bias(V)	Wavelenght (nm)	Responsivity (AW^{-1})	IQE (%)	Rejection ratio	$\tau_r(s)$	$\tau_d(s)$	Refs	Year
Photoconductor	20	250	1099	5438	/	≤ 9	≤ 9	[135]	2019
N-P β-Ga₂O₃/Graphene heterojunction	0	254	10.3×10^{-3}	/	2.28×10^2	2.24×10^{-6}	2.24×10^{-6}	[136]	2019
N-P β-Ga₂O₃/CuBiI₄ heterojunction	5	254	20.68	/	1.14×10^4	/	/	[137]	2022
N-P ε-Ga₂O₃/diamond heterojunction	20	254	0.38	/	259	0.323	0.171	[138]	2022
N-P Ga₂O₃/GaN heterojunction	20	254	44.98×10^{-3}	/	/	$383\times10-3$	383×10^{-3}	[139]	2023
N-P-N β-Ga₂O₃/NiO/β-Ga₂O₃ heterojunction	-10	290	10^{-3}	/	2.8×10^4	2×10^{-6}	2×10^{-6}	[140]	2023
P-I-N ZnO/Ga₂O₃/Ga₂O₃	-5	250	0.73	/	2.5×10^4	/	/	[141]	2019
P-I-N Graphene/γ-Ga₂O₃/SiC	0	250	5.8×10^{-3}	/	10^3	0.108	0.108	[142]	2020
Schottky junction Au/Ni/β-Ga₂O₃	0	212	9.78	42.5	10^4	$<5\times10^{-6}$	$<5\times10^{-6}$	[143]	2020
Schottky junction Pt/β-Ga₂O₃	-5	254	/	/	/	113×10^{-3}	1.5	[132]	2021

Structure								Ref.	Year
Schottky junction IZTO/β-Ga$_2$O$_3$	0	255	17.80×10^{-3}	0.09	/	/	/	[144]	2022
Schottky junction Pt/α-Ga$_2$O$_3$/ITO	-3	254	671	/	/	27×10^{-3}	11×10^{-3}	[145]	2023
Schottky junction W/Graphene/β-Ga$_2$O$_3$	-10	255	14.49	7044	4.56×10^{6}	0.139	0.2	[146]	2024
MSM Au/Ti-β-Ga$_2$O$_3$/Ti/Au	20	254	107.2	/	/	5.4	2.1	[147]	2020
MSM Au/Ti /ε-Ga$_2$O$_3$/ Au/Ti/ Ti/Au	20	254	1300	/	1.87×10^{4}	0.166	0.075	[148]	2023
Avalanche α-Ga$_2$O$_3$/ITO heterojunction	-40	254	5.9×10^{4}	2.9×10^{7}	/	/	/	[149]	2021
Avalanche β-Ga$_2$O$_3$/La$_{0.8}$Ca$_{0.2}$MnO$_3$ heterojunction	-37.9	254	586	3.0×10^{5}	/	/	/	[150]	2023

2.4.3   Constraints of the Ga₂O₃ UV photodetectors

Ga₂O₃ materials exhibit certain limits in their application as UV detectors, the most notable being PPC. The PPC or persistent photocurrent, refers to the continued generation of electric current after removing the light source. This is seen in Figure 2.9 resulting in photocurrent decay times on the order of hours to days [151].
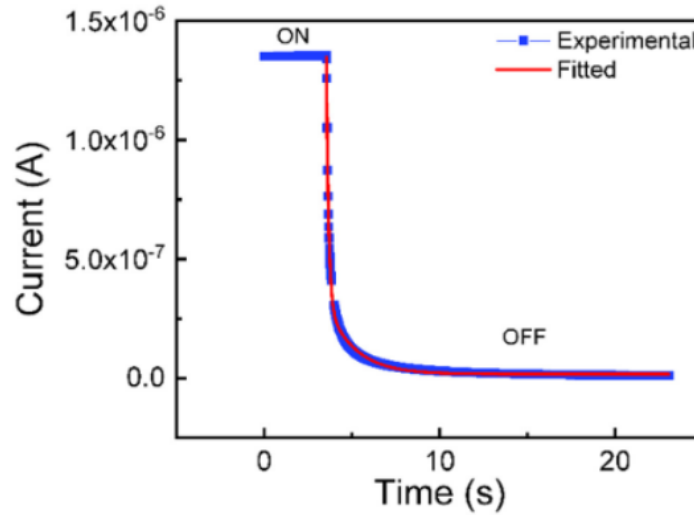
Figure 2.9: The photocurrent decay as a function of time after turning off the illumination [151].

The PPC has been attributed to excitons, negatively charged surface states, metastable defects, V_{Ga}, V_O, nitrogen antisites, deep-level defects, and trapping photo-generated carriers [152].

The falling transient is frequently modeled by a stretched exponential function expressed as [152]:

$$I_{ppc}(t) = I_0 + \exp\left[\left(\frac{t}{\tau}\right)^{\beta}\right] \tag{2.7}$$

Where I_0 is the photocurrent before the illumination source is removed, τ is the decay time constant, and β is the decay exponential ($0 < \beta < 1$) [153].

Experimental results indicate that at high temperatures, thermal energy can release confined photo-generating carriers, thus reducing the PPC [154]. To accommodate this temperature sensitivity, the decay time constant has been represented as a mathematical model expressed as [152]:

$$\tau = \tau_0 exp(\frac{\Delta E}{K_B T}) \tag{2.8}$$

Where ΔE the carrier is capture barrier, K_B is Boltzmann's constant, and T is the temper-

ature.

B. R.Tak et al. prove that deep-level traps are responsible for PPC in β-Ga$_2$O$_3$ thin films by PLD, where the photocurrent persisted for a longer time in β-Ga$_2$O$_3$ material [151].

This photocurrent follows a biexponential equation it is given by the relation [151]:

$$I = I_0 + A \exp\left(-\frac{t}{\tau_1}\right) + B \exp\left(-\frac{t}{\tau_2}\right) \qquad (2.9)$$

Where I_0 is the steady state current, A and B are fitting constants, and τ_1 and τ_2 are the fast and slow decay time components, respectively.

2.4.4 Enhancing the performance of the Ga$_2$O$_3$ UV photodetectors by applying a (Al$_x$Ga$_{1-x}$)$_2$O$_3$ passivation layer

(Al$_x$Ga$_{1-x}$)$_2$O$_3$ films with a WBG can enhance the critical field strength in power electronic devices [155], and the insertion of Al atoms can significantly alter the E_g of intrinsic Ga$_2$O$_3$ and carrier concentration [156]. Moreover, the (Al$_x$Ga$_{1-x}$)$_2$O$_3$ film can be utilized in modulation doped (Al$_x$Ga$_{1-x}$)$_2$O$_3$/Ga$_2$O$_3$ heterostructure. This arrangement allows for greater separation between the ionized donor impurities and the two-dimensional electron gas, enhancing electron mobilities [157]. Several techniques have been investigated for the growth of (Al$_x$Ga$_{1-x}$)$_2$O$_3$ films, including MBE and PLD [158], MOCVD [159], and magnetron sputtering [160]. While there has been some interest in (Al$_x$Ga$_{1-x}$)$_2$O$_3$ films, there is a lack of research on how to prepare detectors for passivating Ga$_2$O$_3$ film surfaces using (Al$_x$Ga$_{1-x}$)$_2$O$_3$ films.

Among these studies, J. Y. Yue et al. fabricated solar-blind UV photodetectors by creating semiconductor metal-structured devices, these devices were made using a layer of β-(Al$_{0.25}$Ga$_{0.75}$)$_2$O$_3$, which was formed via MOCVD, it is established that various surface states augment the dark current, whereas multiple flaws can impede the transfer of carriers, resulting in a reduced switching ratio and diminished device response. To address this issue, β-(Al$_{0.25}$Ga$_{0.75}$)$_2$O$_3$ films were employed as surface passivation materials, due to its WBG achieving exceptional light transmission and strong lattice matching with β-Ga$_2$O$_3$, and when exposed to 254 nm light with a bias of 5 V the β-(Al$_{0.25}$Ga$_{0.75}$)$_2$O$_3$/β-Ga$_2$O$_3$ photodetectors exhibit a dark current of 18 pA and a significant PDCR of 2.16×10^5. After the β-Ga$_2$O$_3$ surface is passivated the dark current is experiencing a significant decrease of 50 times what it was while the PDCR sees a doubling. Undoubtedly, β-Ga$_2$O$_3$ detectors equipped with surface passivation using β-(Al$_{0.25}$Ga$_{0.75}$)$_2$O$_3$ can offer exceptional detector performance [155].

Figure 2.10 (a) illustrates the energy band alignment to gain a deeper understanding of

the charge carrier transport mechanism (before contact). Figure 2.10 (b) displays the energy band structure of β-(Al$_{0.25}$Ga$_{0.75}$)$_2$O$_3$ /β-Ga$_2$O$_3$ heterojunction in the dark case (after contact), the charge carriers continue to move until the E_F level becomes uniform, resulting in the formation of a depletion layer and a potential electric field, this electric field helps sustain the movement of the equilibrium electron and hole carriers through drift and diffusion. The β-(Al$_{0.25}$Ga$_{0.75}$)$_2$O$_3$ passivation layer which has high resistance forms with a minimal number of free electrons at the interface. This layer effectively covers the defect states on the surface leading to exceptionally low levels of dark currents. Nevertheless, when exposed to UV radiation at a wavelength of 254 nm, a significant quantity of electron-hole pairs are produced, resulting in a substantial alteration of the carrier transport mechanism, as depicted in Figure 2.10 (c) when the electron-hole pair formed by light moves and spreads out in the electric field that is already there the electrons and holes quickly split and transform into free carriers, electrons are moved from β-Ga$_2$O$_3$ to β-(Al$_{0.25}$Ga$_{0.75}$)$_2$O$_3$ whereas holes are drifted from β-(Al$_{0.25}$Ga$_{0.75}$)$_2$O$_3$ to β-Ga$_2$O$_3$ and collected at the Ti/Au electrode due to an electric field [155].
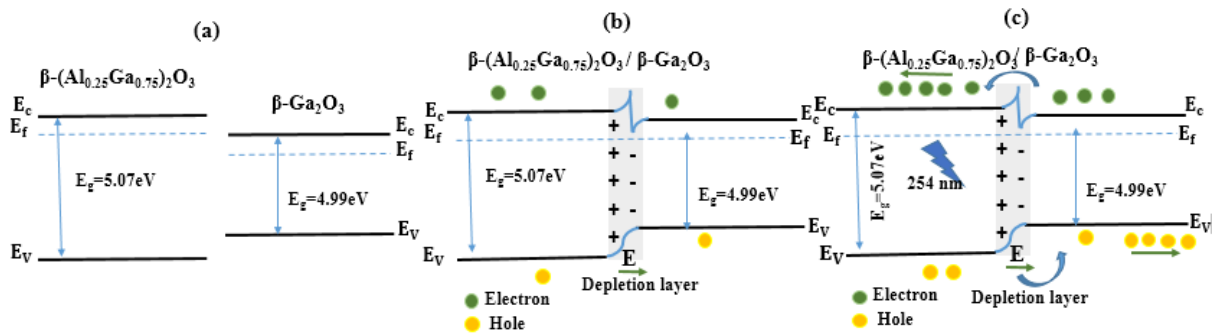
Figure 2.10: The energy band alignment of the β-(Al$_{0.25}$Ga$_{0.75}$)$_2$O$_3$ to β-Ga$_2$O$_3$ heterojunction is as follows: **(a)** before contact, **(b)** after contact in the dark case, and **(c)** after contact under 254 nm illumination at 5 V [155].

2.4.5 The optimal substrates (semi-insulators) for the deposition of the Ga$_2$O$_3$ UV photodetectors

Although bulk Ga$_2$O$_3$ was an ideal substrate for the epitaxial growth of high-quality Ga$_2$O$_3$ thin films, its expensive cost and poor thermal conductivity still hindered the commercialization of homoepitaxy. Therefore, the heteroepitaxy of Ga$_2$O$_3$ films on low-cost and large-sized substrates was still important. Therefore the task of choosing the appropriate substrate is a crucial obstacle in the production of Ga$_2$O$_3$-based devices of superior quality, where the substrate and Ga$_2$O$_3$ films should have a similar atomic arrangement with a small mismatch [161]. Table 2.2 displays a lattice mismatch comparison between Ga$_2$O$_3$ films and various materials that can act as a substrate with them.

When considering Ga$_2$O$_3$ photodetectors the choice of substrate greatly affects device performance. Al$_2$O$_3$ remains a strong option due to its high transparency and low absorption across UV-visible wavelengths, which is beneficial for photodetectors, though lattice mismatch can still lead to defects its efficiency in the UV region is limited by its E_g [161]. GaN has a WBG and good electron mobility making it advantageous for photodetectors, though it may still present challenges with lattice mismatch [161].

Table 2.2: Comparison of lattice mismatch between Ga$_2$O$_3$ films and various substrates.

Substrate	Lattice mismatch (%)	Epitaxial relationship	Refs
GaN	+4.67	$[010] \parallel [11\bar{2}0]$	[161]
Al$_2$O$_3$	+1.610	$[010] \parallel [10\bar{1}0]$	[161]
Si	- 6.3	$[\bar{2}01] \parallel [111]$	[162]
MgO	+2.5	$[10\bar{1}0] \parallel [111]$	[163]
GaAs	+1.36	$[010] \parallel [011]$	[164]
4H-SiC	+6.9	$[102] \parallel [\bar{1}100]$	[165]
MgAl$_2$O$_3$	-3.18	$[100] \parallel [100]$	[166]
AlN	+2.4	$[\bar{2}01] \parallel [2000]$	[167]
ZnO	+5	$[\bar{2}01]\bar{1}[01\bar{1}0]$	[168]
SrTiO$_3$	+5.51	$[\bar{2}01] \, \bar{1} \, [111]$	[169]

'+': tensile strain, '-': compressive

Si offers cost-effective processing and transparency but the lattice mismatch and its E_g can limit the detection range [162]. MgO is transparent in the UV-visible spectrum and has a good lattice match with Ga$_2$O$_3$ though chemical reactivity can pose problems [163]. GaAs provide high electron mobility and direct E_g for efficient charge transport but may struggle with transparency and thermal stability issues [164]. 4H-SiC offers high thermal conductivity and lattice matching, making it suitable for high-performance photodetectors though it can be costly [165]. MgAl$_2$O$_3$ offers transparency in the UV-visible range and good lattice matching but potential chemical compatibility issues may arise [166].

AlN has a WBG and good lattice match making it suitable for UV detectors but it may face cost and compatibility issues [167]. ZnO is naturally transparent in UV-visible wavelengths and has good lattice matching though chemical reactivity and stability issues could affect performance [168]. SrTiO$_3$ has good dielectric properties and moderate lattice matching, but its high dielectric constant may affect detector performance while its limited transparency in the UV range may pose challenges [169]. Therefore, we can deduce that GaN, AlN, and 4H-SiC substrates possess the capacity to offer enhanced sensitivity and performance for

UV photodetector applications, despite the manufacturing cost. To address the mismatch, recent research has demonstrated that buffer layers are now being used to minimize the discrepancy between the substrate and the active layer, to reduce dislocations, stress, and other issues during growth this, in turn, enhances the device's performance, it will be explained in the following part.

2.4.6 Enhancing the performance of the Ga$_2$O$_3$ UV photodetectors by adding a buffer layer between the Ga$_2$O$_3$ epitaxial layer and substrate

Due to its corundum structure, Al$_2$O$_3$ is commonly employed as the substrate for the heteroepitaxial deposition of β-Ga$_2$O$_3$ thin films. β-Ga$_2$O$_3$ has a monoclinic structure, causing a significant lattice mismatch between the epitaxial layer and the substrate during heteroepitaxial growth, this mismatch is a crucial feature that impacts the quality of β-Ga$_2$O$_3$ epitaxy [170], and it is widely recognized that the performance of the optoelectronic device is intricately linked to the crystalline quality of the film [171]. Nevertheless, the process of directly forming high-quality β-Ga$_2$O$_3$ films onto routinely utilized substrates like glass, Al$_2$O$_3$, and Si has proven challenging due to the lattice mismatch and disparate coefficient of thermal expansion [172, 173].

Inserting a buffer layer, either a hetero-buffer layer or a homo-buffer layer, is a widely recognized method to enhance the quality of film crystallization, this buffer layer helps reduce the mismatch in lattice structure between the films and substrates [174, 175]. J. Huang et al. conducted a study on the fabrication of β-Ga$_2$O$_3$ films using the RF magnetron sputtering technique, a study was conducted on the effect of the β-Ga$_2$O$_3$ homo-buffer layer and annealing treatment on the textural, optical, morphological, and electrical characteristics of β-Ga$_2$O$_3$ films, the results revealed an improvement in crystalline quality and transmittance of annealed β-Ga$_2$O$_3$ films prepared with homo-buffer layers. A novel technique was employed to create β-Ga$_2$O$_3$ films UV photodetectors, utilizing newly developed B and Ga co-doped ZnO films (BGZO) with Au interdigitated electrodes. An excellent Ohmic contact is established between the film and the electrode. The detector utilizing β-Ga$_2$O$_3$ films with homo-buffer layers achieved a greater photo responsivity value and faster response times [176].

Alternatively, C. Gao et al. improved the efficiency of blind solar UV photodetectors by employing thin films composed of β-Ga$_2$O$_3$, their methodology consisted of enhancing the quality of β-Ga$_2$O$_3$ by implementing an AlN hetero-buffer layer, and the technique of MOCVD was used to fabricate thin coatings of β-Ga$_2$O$_3$ on P-Si substrates, adding an AlN hetero-buffer layer and removing the amorphous SiO_x surface layer on the Si substrate significantly improves the photodetection performance in the β-Ga$_2$O$_3$/AlN/Si heterojunction. The PDCR is 2.7×10^3, the responsivity at a bias voltage of 5V is 11.84 A/W, and the detectivity is 8.31×10^{13} $cm\sqrt{HZ}W^{-1}$ [177].

2.4.7 Enhancing the performance of the Ga$_2$O$_3$ UV photodetectors by using Graphene as Schottky contact

The selection of contact material is essential in determining the performance of UV photodetectors, using typical designs with simple metallic Schottky contacts, the migration of contact atoms to the interface and then into the drift zone can be induced by high-energy UV photons, has the potential to impact the reliability of the device [178]. To address this problem, researchers have investigated translucent conductors as potential substitutes that provide enhanced resistance to heat effects caused by UV radiation [179]. Nevertheless, it has been noted that certain transparent conductors despite their resistance to thermal damage can nevertheless absorb UV photons thereby affecting the efficiency of the detector [180], a more favorable solution arises by utilizing Graphene as a Schottky contact, in recent years it has garnered significant research interest [181, 182].

Graphene demonstrates remarkable resistance to heating caused by UV radiation and retains its high transparency, this makes it an excellent choice for improving the performance of UV photodetectors while minimizing any negative impact on device efficiency [183]. In addition to its exceptional optical transparency in the UV-visible range, mechanical durability, and chemical stability, Graphene possesses a distinctive electrical structure that sets it apart from both metals and semiconductors [181, 182], the overall transparency of the material is a result of its low absorbance and effective electronic transitions [184].

M. Chen et al. demonstrate that a solar-blind Graphene/β-Ga$_2$O$_3$ vertical photodetector can be fabricated by mechanically transferring monolayer Graphene to the cleaved (100) surface of a 30 μm thick β-Ga$_2$O$_3$ single-crystal substrate, under zero bias conditions the photodetector demonstrated a response time of 2.24s and a maximum responsivity of 10.3 mA/W when exposed to 254 nm light with an incident light power of 2.06 W/cm^2. Over three months the detectors' performance remained consistent while stored in a normal environment. The zero-bias Graphene/β-Ga$_2$O$_3$ photodetector has great potential for future photoelectric applications because of its extremely quick response and outstanding stability [136].

2.4.8 The impact of high operating temperature on the Ga$_2$O$_3$ UV photodetectors performance

UV photodetectors that operate at high temperatures are greatly sought after for demanding environmental applications, such as flame detection in conditions with elevated surface temperatures [185–187]. Recently there has been a significant focus on researching high-temperature photodetectors using Ga$_2$O$_3$ [188–190]. This experimentally proves that Ga$_2$O$_3$ is a promising high-temperature solar-blind UV detector material, where thin films offer sev-

eral advantages over one-dimensional and bulk materials, including easy device integration, excellent repeatability, and the ability to be fabricated over large areas [191, 192].

Despite notable advancements in the creation of high-temperature photodetectors with Ga$_2$O$_3$ films, the performance of these devices remains below anticipated levels. B. R. Tak et al. fabricated β-Ga$_2$O$_3$ film-based Schottky barrier photodetector using PLD, these devices exhibited a significant dark current of approximately 1000 nA and a low PDCR of around 2.3 at 250°C [189]. Constructing β-Ga$_2$O$_3$ film high-temperature photodetectors with low dark current, high PDCR, and quick response recovery speed is challenging due to the decrease in the dark current and photo response properties. However, it can be achieved by effective methods, due to the inherent stability of the crystalline β-Ga$_2$O$_3$ layer it is well-suited for the fabrication of high-temperature devices. Nevertheless, the majority of documented crystalline β-Ga$_2$O$_3$ films often necessitate elevated growth temperatures (ranging from 600 to 800°C) when employing direct vacuum deposition [193].

In the commercial production process of crystalline Ga$_2$O$_3$ films, high-temperature growth may limit their large-area manufacture and further reduce costs. Typically, the process of depositing materials at high temperatures necessitates the use of costlier vacuum apparatus such as MBE and MOCVD, less expensive equipment such as ALD and magnetron sputtering faces challenges in achieving the elevated growth temperatures required, equipment parts at a high temperature may be more likely to age diminish their service life raise maintenance expenses [194].

The high temperature of the heating plate necessitates the inclusion of thermal insulation in the design and production of the growing equipment. Additionally, modules must be incorporated to cool other components of the equipment that are near the heating plate, maintaining a high vacuum and steady oxygen partial pressure in the growth chamber may be compromised by the elevated temperature. On the other hand, deposition at RT can successfully overcome the restrictions of high-temperature deposition. However, the Ga$_2$O$_3$ film obtained at RT deposition has an amorphous structure with poor thermal stability, which is not suitable for fabricating UV devices that operate at high temperatures [194].

Chapter 3: Basics of Schottky device simulation by SILVACO - ATLAS

Chapter 3

Basics of Schottky device simulation by SILVACO-ATLAS

3.1 Introduction

The crux of the "Schottky barrier" concept lies in the unique rectifying properties observed at the M/S interface. The most prominent distinction between the Schottky barrier and the P-N interface lies in the fundamental characteristics of their structures, the Schottky barrier exhibits a lower interface voltage compared to the P-N junction, and a notable feature is the relatively thin, almost negligible width of the depletion layer at the metal end in the Schottky barrier configuration, this unique combination of lower interface voltage and a thin depletion layer contributes significantly to Schottky barrier devices' distinct behavior and performance compared to the P-N junction [96]. The first part of this chapter will mainly delve into understanding the physical mechanisms of Schottky contact. The second part will focus on the simulation process using the SILVACO-ATLAS software.

3.2 The functional physical mechanisms in Schottky contact

Electronic devices typically comprise various materials with distinct properties such as insulators, conductors, and semiconductors, the amalgamation of these materials results in the formation of critical interfaces, and one example is the Schottky junction, this junction arises between a metal and a semiconductor due to the E_F mismatch resulting from differences in their work functions. Consequently, a barrier known as the Schottky barrier ϕ_B is established with its height being a critical determinant of the electrical properties at the M/S interface. In-depth discussions and interpretations of ϕ_B often commence by examining the Schottky-Mott rule [195].

$$\phi_B = \phi_M - \chi_{SC} \tag{3.1}$$

Where ϕ_M and χ_{sc} are the metal work function and electronic affinity of the semiconductor respectively, in recent experimental investigations of Schottky dualities it has become increasingly apparent that the Schottky interface as envisioned by the Schottky-Mott rule deviates from its idealized image. This departure from the anticipated correlation between ϕ_B and ϕ_M is attributed to the presence of various new phenomena that control the Schottky contact [195], Included in these phenomena we mention:

3.2.1 Fermi-level pinning

Fermi-level pinning theory suggests that in an M/S contact wave functions of electrons in the metal can decay into the semiconductor in the E_g as shown in Figure 3.1, creating intrinsic states known as $MIGS$. The energy level in the E_g at which the dominant character of the interface states changes from donor to acceptor is called E_{CNL}. In an M/S junction, charge transfer generally occurs across the interface charging of these states creates a dipole that tends to drive the band lineup toward a position that would give zero dipole charge, effectively pulling E_{FM} towards the E_{CNL}. So then strongly E_{FM} will be pinned towards E_{CNL} is determined by the pinning factor "S", where S is defined by $\dfrac{d\phi_B}{d\phi_M}$, using S for n-type semiconductors can be expressed ϕ_B as [196].

$$\phi_B = S(\phi_M - \chi_{SC}) + (1 - S)(E_C - E_{CNL}) \tag{3.2}$$

Where ϕ_M represents the metal work function and χ_{sc} represents the electronic affinity of the semiconductor, when S=1 corresponds to the Schottky-Mott limit, and S =0 corresponds to the completely pinned limit, often referred to as the Bardeen limit [196]. The Fermi-level pinning stands as a primary catalyst for the degradation of semiconductor devices.
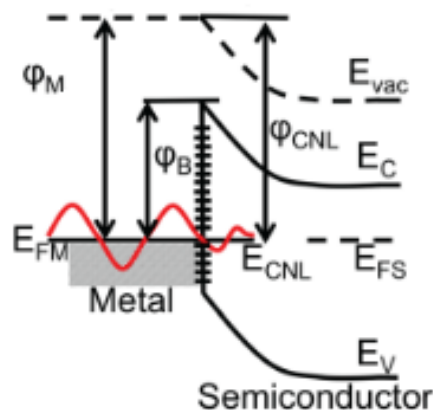
Figure 3.1: Fermi-level pinning in M/S contact, where the Fermi level is pinned at the charge neutrality level. This is the case where S = 0 [196].

3.2.2 Image-force lowering

Image-force lowering, commonly recognized as the Schottky effect or Schottky-barrier lowering, refers to the reduction in the barrier energy for the emission of charge carriers under the influence of an electric field. Considering the vacuum-metal system the fundamental energy required for an electron to move from the initial energy state at the Fermi level to the vacuum is the $q\phi_M$, when an electron is situated x distance away from the metal, it induces a positive charge on the metal surface. The attractive force between the electron and the induced positive charge is comparable to the force that would be present between the electron and an equivalent positive charge positioned at -x, this referred to positive charge is termed the image charge. The attractive force towards the metal is known as the image force, and because the created force is attractive the potential difference created is negative, thus corresponding to a lowering of the existing barrier [197], which is expressed by the following relationship:

$$F = \frac{-q^2}{4\pi\varepsilon_0(2x)^2} = \frac{-q^2}{16\pi\varepsilon_0 x^2} \tag{3.3}$$

Where q , ε_0 are image charge, permittivity of vacuum space, respectively.

3.2.3 Carrier recombination

3.2.3.1 SRH recombination

Within the forbidden E_g a dependent energy state known as a trap can act as a recombination center capturing electrons and holes. The recombination theory proposed by SRH postulates the existence of a single recombination center or trap at the energy level E_T within E_g [198].

Assume the trap functions as an acceptor-type trap essentially adopting a negative charge in the presence of an electron and remaining electrically neutral when unoccupied, four basic processes occur for this trap [198]. As shown in Figure 3.2:

1. The capture of an electron.

2. The emission of an electron.

3. The capture of a hole.

4. The emission of a hole.
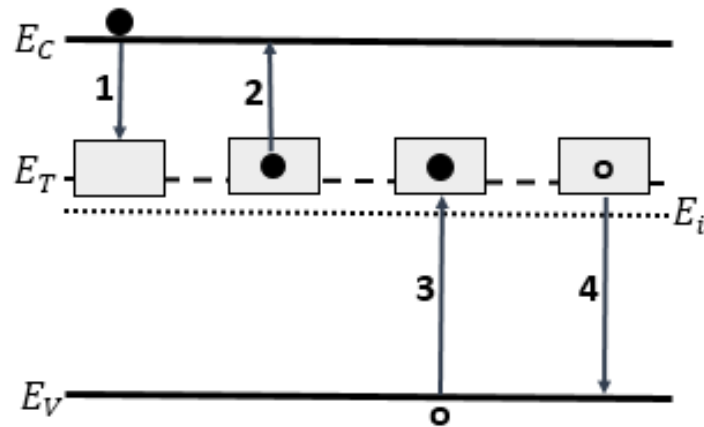
Figure 3.2: The four basic processes for the case of an acceptor-type trap [198].

In the process of electron capture the rate at which electrons from the conduction band are taken in by the acceptor-type trap correlates directly with the electron density in the conduction band and the density of available empty trap states. This allows the electron capture rate to be formulated as follows [198]:

$$R_{cn} = C_n N_T \left[1 - f_F(E_T) \right] n \tag{3.4}$$

Where R_{cn} represents the capture rate to the electron, C_n is the capture coefficient proportional to the electron-capture cross-section, N_T stands for the total concentration of trapping centers, n denotes the electron concentration in the conduction band, and $f_F(E_T)$ represents the Fermi function at the trapped energy E_T. The Fermi function at the trapped energy is given by [198]:

$$f_F(E_T) = \frac{1}{1 + \exp\left(\dfrac{E_T - E_F}{K_B T}\right)} \tag{3.5}$$

When electrons are emitted from a filled trap the rate of emission into the conduction band is proportional to the number of filled traps. The expression for the emission rate is as follows [198]:

$$R_{en} = E_n N_T f_F(E_T) \tag{3.6}$$

Where E_n represents the emission constant, and $f_F(E_T)$ denotes the probability of trap occupancy [198].

In a state of thermal equilibrium, a delicate balance is maintained where the rates of electron capture from the conduction band and electron emission back into the conduction band are precisely equal, this equilibrium signifies a state of harmony ensuring that the sys-

tem remains stable and that the population of electrons in the conduction band remains constant over time [198].

$$R_{cn} = R_{en} \tag{3.7}$$

$$C_n N_T \left[1 - f_{F0}(E_T)\right] n_0 = E_n N_T f_{F0}(E_T) \tag{3.8}$$

The thermal-equilibrium Fermi function is represented by $f_{F0}(E_T)$, with n_0 being the equilibrium electron density. Employing the Boltzmann approximation for the Fermi function allows us to express E_n in terms of C_n [198].

$$E_n = n' C_n \tag{3.9}$$

$$n' = N_C \exp\left(-\frac{E_C - E_T}{K_B T}\right) \tag{3.10}$$

Where n' corresponds to an electron concentration that would be found in the conduction band if the trapped energy E_T were in alignment with the E_F.

In a non-equilibrium state, where excess electrons are present the net rate at which electrons are captured from the conduction band can be expressed as [198]:

$$R_n = R_{cn} - R_{en} \tag{3.11}$$

$$R_n = C_n N_T \left[1 - f_F(E_T)\right] n - E_n N_T f_F(E_T) \tag{3.12}$$

$$R_n = C_n N_T \left[1 - f_F(E_T)\right] n - n' C_n N_T f_F(E_T) \tag{3.13}$$

$$R_n = C_n N_T \left[n \left(1 - f_F(E_T)\right) - n' f_F(E_T)\right] \tag{3.14}$$

By employing the same mechanism of capturing and emitting a hole, we can deduce the following equation [198]:

$$R_p = C_p N_T \left[p \left(1 - f_F(E_T)\right) - p' f_F(E_T)\right] \tag{3.15}$$

where

$$p' = N_V \exp\left(-\frac{E_T - E_V}{K_B T}\right) \tag{3.16}$$

So we find it in the end [198]:

$$R_n = R_p = \frac{c_n c_p (np - n_i^2)}{c_n(n + n') + c_p(p + p')} \tag{3.17}$$

where

$$n_i^2 = n'.p' \tag{3.18}$$

3.2.3.2 Auger recombination

In the Auger recombination process an electron combines with a hole. However, instead of emitting a photon this interaction leads to the elevation of another carrier to a higher-energy state, it can also be interpreted as two electrons encountering each other near a hole causing a non-radiative recombination event between electron and hole. The second electron absorbs the energy from this event and the power is eventually transferred non-radioactively from the third carrier via phonon emission to the lattice [199], it is expressed by the following relationship [200]:

$$R_{Auger} = AUGN(pn^2 - nn_i^2) + AUGP(np^2 - pn_i^2) \tag{3.19}$$

Where $AUGN$ and $AUGP$ are the Auger coefficients, n_i is the intrinsic concentration, n and p are the electrons and holes concentration in the conduction and valance bands, respectively.

3.2.4 Thermionic emission

The TE refers to the process in which electrons overcome the Schottky barrier by gaining enough thermal energy to move from a lower energy level to a higher one, it means that the metal has an excess of electrons, and the semiconductor has a deficiency. The difference in shipping creates a potential barrier, thanks to TE the electrons on the metal side can obtain enough energy from the heat to jump over this barrier and move to the semiconductor. Thus the flow of electrons creates a current called TE current [201].

The TE characteristics are established under the assumption that the barrier height significantly exceeds $K_B T$, allowing the application of the Maxwell-Boltzmann approximation, and it is further assumed that thermal equilibrium remains unaffected by this process. Consequently, TE current is the aggregate of the current density resulting from the flow of electrons from the semiconductor to the metal and the current density originating from electrons moving from the metal to the semiconductor. Following certain approximations the TE current density can be expressed as [202]:

$$J_{TE} = J_S \exp\left(\frac{q(V - R_s J)}{\eta K_B T}\right) \tag{3.20}$$

Where J_S is the saturation current density, q is the elementary charge, R_s series resistance, η the ideality factor, K_B is the Boltzmann constant, and T is the absolute temperature.

Where

$$J_S = A^* T^2 \exp\left(-\frac{q\phi_B}{K_B T}\right) \tag{3.21}$$

Where A^* denotes the Richardson constant, which is specified as 41.11 $Acm^{-2}K^{-2}$ for β-Ga$_2$O$_3$ [203]. Additionally, ϕ_B represents the SBH.

Carrier tunneling occurs in strongly doped semiconductors at energies below the entire barrier. The phenomenon in question is referred to as TFE and is particularly prevalent in semiconductors with a high doping concentration of approximately $10^{18} cm^{-3}$. The M/S interface is primarily characterized by FE, which is influenced by a significant presence of defect densities [204]. The various current transfer processes in M/S Schottky diodes are depicted in Figure 3.3.
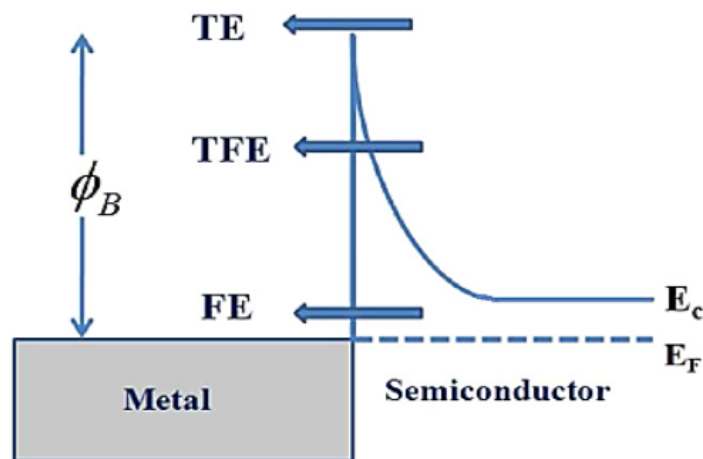
Figure 3.3: The current transmission mechanisms in M/S Schottky diodes [204].

3.2.5 Diffusion

This process is essentially a natural response to restore equilibrium in carrier concentration, as carriers diffuse across the gradient the system seeks a balanced distribution. Fick's law governs this flux articulating the rate of carrier diffusion to the concentration gradient. The diffusion theory assumes that the barrier height is much larger than $K_B T$. The movement of carriers in this flux gives rise to a diffusion current density of electrons n and holes p, which can be expressed as [197]:

$$\overrightarrow{J_{Dn}} = qD_n \frac{d\Delta n}{dx} \tag{3.22}$$

$$\overrightarrow{J_{Dp}} = qD_p \frac{d\Delta p}{dx} \tag{3.23}$$

Where q elementary charge of an electron, D_n and D_p diffusion coefficient for electrons

and holes, $\frac{d\Delta n}{dx}$ and $\frac{d\Delta p}{dx}$ gradient of the electrons and holes concentration a function of distance, respectively.

3.2.6 Tunneling

Tunneling in semiconductors is a quantum phenomenon where electrons can traverse barriers considered impassable in classical physics. In semiconductors, electrons can overcome potential obstacles through quantum mechanics. When an electron encounters a barrier with insufficient energy to surmount it conventionally, tunneling introduces a non-zero probability for the electron to emerge on the other side, bypassing the usual energy requirement. The relationship determines the tunneling current density flowing through the tunnel [205]:

$$\overrightarrow{J_T} = \frac{A^* T_L}{K_B} \int_\epsilon^\infty \Gamma(E') \ln\left(\frac{1 + F_S(E')}{1 + F_m(E')}\right) dE' \tag{3.24}$$

Where A^* the effective Richardson's coefficient, T_L lattice temperature, K_B Boltzmann constant, ϵ electron energy, $F_S(E')$ and $F_m(E')$ the Maxwell-Boltzmann distribution of semiconductor and metal, respectively, $\Gamma(E')$ it is the probability of tunneling, expressed as [205]:

$$\Gamma(E') = \exp\left[-2\frac{\sqrt{2m^*}}{\hbar} \int_{x_1}^{x_2} \sqrt{E_C(x) - E'}\, dx\right] \tag{3.25}$$

Where $E_C(x)$ corresponds to the potential energy distribution across the Schottky barrier diode, and (x_1, x_2) signifies the classical turning points associated with the system.

3.2.6.1 Band to band tunneling

BBT is a quantum mechanical phenomenon in semiconductors where charge carriers (electrons or holes) can tunnel from the valence band to the conduction band or vice versa as shown in Figure 3.4. This process usually occurs in high electric fields by internal FE the rate of tunneling generation is [206]:

$$G_{BBT} = B_1 E^{B_2} \exp\left(-\frac{B_3}{E}\right) \tag{3.26}$$

Where B_1, B_2 and B_3 represent the BBT parameters, and E denotes the local electric field.
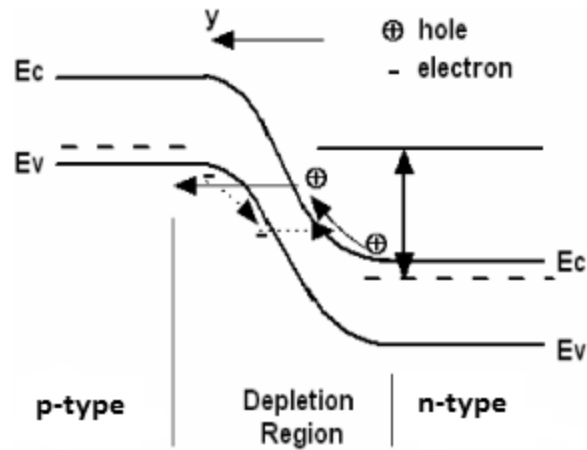
Figure 3.4: A graphical illustration depicting the process of BBT [207].

3.3 Simulation by SILVACO-ATLAS software

3.3.1 Definition

SILVACO-TCAD software short for Silicon Valley Corporation Technology Computer-Aided Design encompasses a simulation package for semiconductor device processes, it incorporates various physically based simulators like ATHENA, ATLAS, MERCURY, SSUPREM3, etc...., grouped within the DECK BUILD environment, each simulator plays a distinct role in simulating different processes. In the scope of this work, ATLAS stands out as the most appropriate module. ATLAS is a physically based two and three-dimensional device simulator forecasting the electrical behavior of designated semiconductor structures and offering insights into the internal physical mechanisms governing the device's operation. The results obtained from the simulation are graphically represented and analyzed using a dedicated tool called TONYPLOT is a conceptual tool that charts the simulation results providing scientific visualization capabilities including XY plots with both linear and logarithmic axes [208], Figure 3.5 illustrates the inputs and outputs of the SILVACO-ATLAS simulation.

The SILVACO-ATLAS program operates by inputting device parameters and working conditions and then solving a series of equations at each node within the device's network, these equations based on Maxwell's laws include Poisson's equation, carrier continuity equations, and transport equations [208].

Poisson's equation establishes a connection between electrostatic potential and space charge density, and it is expressed as follows [208]:

$$div(\varepsilon \nabla \psi) = -\rho \tag{3.27}$$

Where ε is the permittivity, ψ the electrostatic potential, and ρ the space charge density.
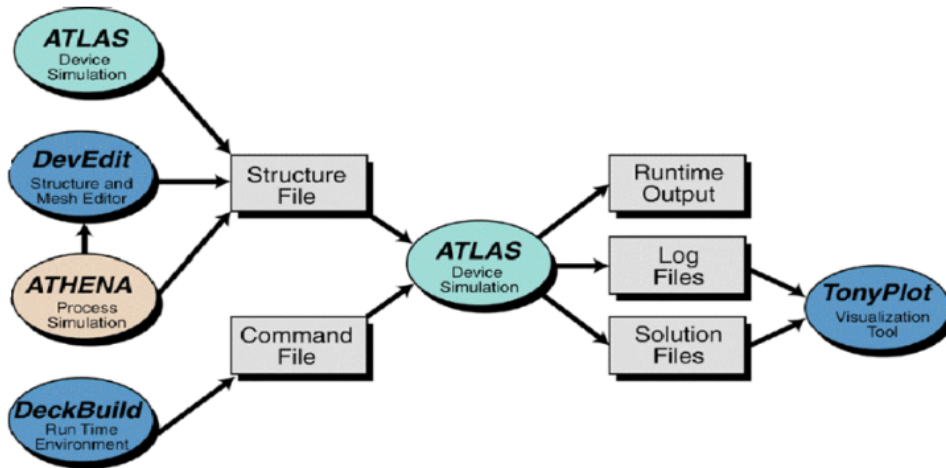
Figure 3.5: Illustrates the inputs and outputs of the SILVACO-ATLAS simulation [208].

Equations defining the continuity for electrons and holes are given by [208]:

$$\frac{dn}{dt} = -\frac{1}{q}div\vec{J}_n + G_n + R_n \tag{3.28}$$

$$\frac{dp}{dt} = -\frac{1}{q}div\vec{J}_p + G_p + R_p \tag{3.29}$$

Where n, p are the concentrations of electrons and holes, $\vec{J}_n$ and $\vec{J}_p$ are the electron and hole current densities, G_n and G_p the generation rates for electrons and holes, R_n and R_p are the recombination rates for electrons and holes, and q electron charge, respectively.

The transport equations typically arise through the application of approximations and simplifications to the Boltzmann transport equation, this process gives rise to various transport models including the drift-diffusion model, the energy balance transport model, and the hydrodynamic model. Among these, the drift-diffusion model stands out as the simplest [208].

The current densities in the continuity equations can be approximated using the drift-diffusion model, as indicated by derivations rooted in the Boltzmann transport theory. Hence, this thesis employs the drift-diffusion model to characterize the current density, the model is expressed as [208]:

$$\vec{J}_n = qn\mu_n\vec{E}_n + qD_n\nabla n \tag{3.30}$$

$$\vec{J}_p = qp\mu_p\vec{E}_p + qD_p\nabla p \tag{3.31}$$

Where μ_n, μ_p are the electron and hole mobilities, $\vec{E}_n$, $\vec{E}_p$ are the electric field for electrons and holes, D_n, D_p are the diffusion coefficients corresponding to electrons and holes,

and ∇n, ∇p the gradients of electron and hole concentrations, respectively.

3.3.2 Deckbuild

Deckbuild serves as the primary application overseeing the simulation accepting required input files, it acts as the central for controlling all simulations as shown in Figure 3.6. Deckbuild consists of two windows the first window facilitates entering and modifying commands, while the second window manages exit modes and displays simulation results [208], the code within the input file triggers the execution of SILVACO-ATLAS as shown in Figure 3.6 with the command:

```
go atlas
```
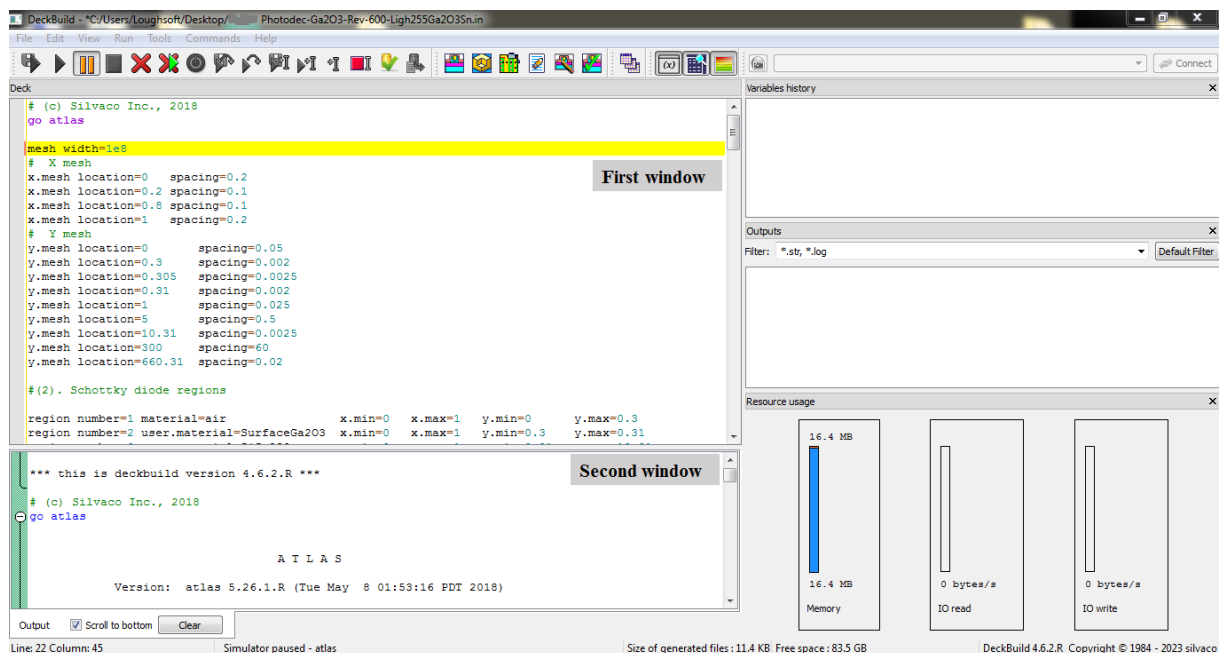

Figure 3.6: Deckbuild.

The order of data in the SILVACO-ATLAS input file is crucial since it must adhere to the precise sequence of five consecutive steps illustrated in Figure 3.7, any deviation from this prescribed sequence may lead to an error message, potentially causing the program to function improperly or terminate abruptly.

Figure 3.7: SILVACO-ATLAS command groups with the primary statements in each group [208].

3.3.2.1 Structure specification

In the SILVACO-ATLAS commands file, the initial step involves defining the simulated structure, comprising four statements arranged in the following manner [208]:

1. Mesh.

2. Region.

3. Electrode.

4. Doping.

To initiate the simulation you should start by choosing "mesh", a mesh encompasses a collection of elements that collectively define the device, it is constructed by intersecting two sets of lines one parallel and the other perpendicular to create a grid resembling the device's shape. To establish the grid three crucial pieces of information: are the line's direction "x" or "y", the localization of lines "l", and the spacing between them "s", representing the distance between the minor lines in μm [208].

```
x.mesh  location=0      spacing=0.2
x.mesh  location=1      spacing=0.2
# y mesh
y.mesh  location=0      spacing=0.05
y.mesh  location=0.3    spacing=0.002
y.mesh  location=0.31   spacing=0.002
y.mesh  location=10.31  spacing=0.0025
```

```
y.mesh   location=300    spacing=60
y.mesh   location=660.31 spacing=0.02
```

Following that, we specify the types of materials employed accomplished through "region" statements [208].

```
region number=1 material=air x.min=0   x.max=1  y.min=0     y.max=0.3
region number=2 user.material=surfaceGa2O3 x.min=0 x.max=1  y.min=0.3 \
 y.max=0.31
region number=3 user.material=SiGa2O3   x.min=0 x.max=1   y.min=0.31   \
y.max=10.31
region number=4 user.material=SnGa2O3 x.min=0 x.max=1 y.min=10.31 \
 y.max=660.31
region number=5 user.material=IZTO x.min=0.2 x.max=0.8 y.min=0 y.max=0.3
```

The term material defines the composition of the material and the statement "user" is used in the case of unknown material in the SILVACO-ATLAS database, the parameters "x.min", "x.max", "y.min", and "y.max" are used to specify the location, dimensions, and geometry of the region in μm, and the parameter "number = n" specifies the number of this region [208].

The next step is represented by an "electrode" statement, which involves specifying electrodes, this statement designates the locations and names of electrodes within a mesh previously defined. The electrode identifier should consist of an n-digit integer, each number in the sequence denotes a distinct electrode number [208].

```
electrode name=anode user.material=IZTO x.min=0.2 x.max=0.8  y.min=0 \
y.max=0.3
electrode name=cathode bottom material=ITO
```

The Schottky barrier is identified as the barrier height at the junction for injecting electrons from the metal to the semiconductor conduction band, it equals the difference between ϕ_M and χ_{SC}. Consequently, whether the contact is rectifying or Ohmic is determined by ϕ_M. The term "contact" in SILVACO-ATLAS instructs how to handle the electrode, by default an electrode in contact is considered Ohmic, if the electrode is intended to be treated as a Schottky contact, the relevant work function must be defined accordingly [208].

```
contact name=anode workfunction=4.79
```

Figure 3.8 illustrates the device mesh and structure generation, achievable with the code provided earlier.
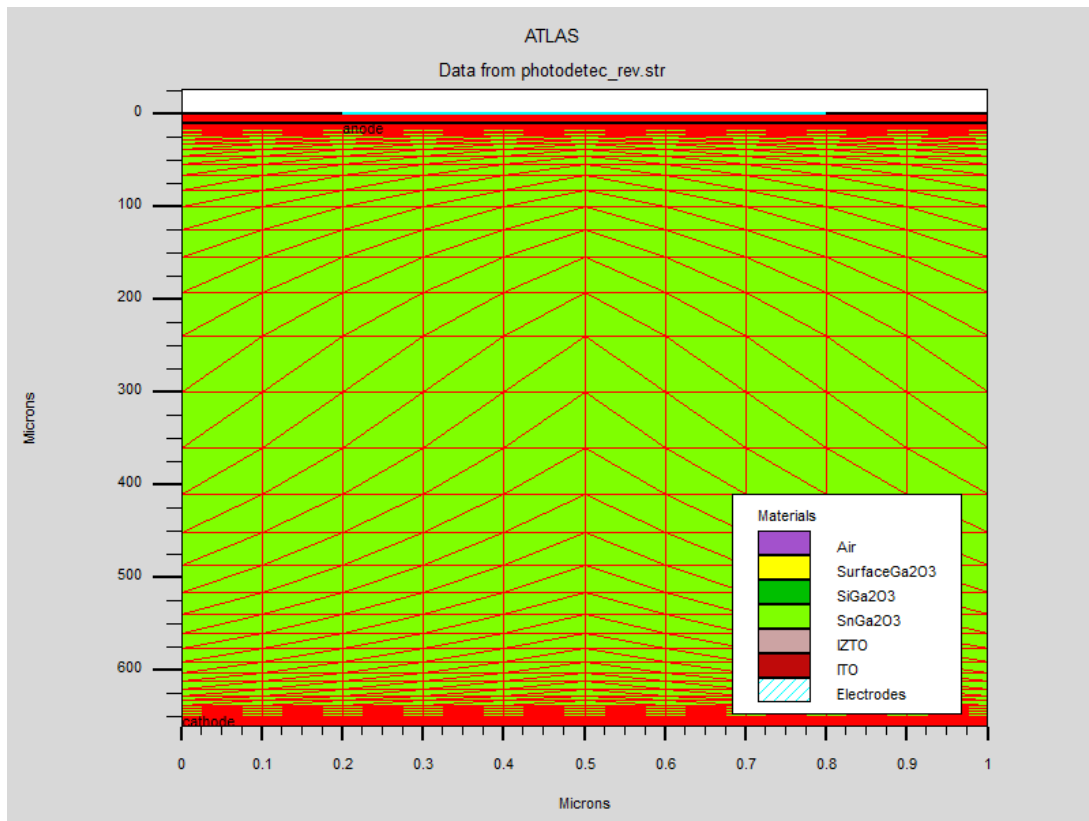
Figure 3.8: Creating a mesh and generating the structure.

The "doping" statement serves to elucidate the doping profiles within a device structure, each building element is characterized by a unique "doping" statement, its specified location through "x.min", "x.max", "y.min", and "y.max", its doping type "n-type", and its doping concentration "conc". Additionally, the parameter "uniform" plays a key role in determining the type of doping distribution [208]. Figure 3.9 shows the uniform doping profile for the different layers constituting the device.

```
doping conc=2.80e20 n.type uniform x.min=0.2 x.max=0.8 y.min=0 y.max=0.3
doping conc=3e16 n.type uniform x.min=0 x.max=1 y.min=0.3 y.max=10.31
doping conc=1e18  n.type uniform  x.min=0 x.max=1 y.min=10.31 y.max=660.31
```

Typically, for enhancing the realism of simulations, profound imperfections are considered, these imperfections wield a notable influence on the electrical characteristics of the device. The "trap" statement triggers bulk traps at specific energy levels within the semiconductor E_g, featuring a consistent distribution and specifying their parameter values, it is defined in the SILVACO-ATLAS code as follows [208]:

```
trap acceptor x.min=0 x.max=1 y.min=0.3 y.max=0.31 e.level=0.75    \
density=9e15  sign=5.4e-11 sigp=5.4e-13 degen=1
```
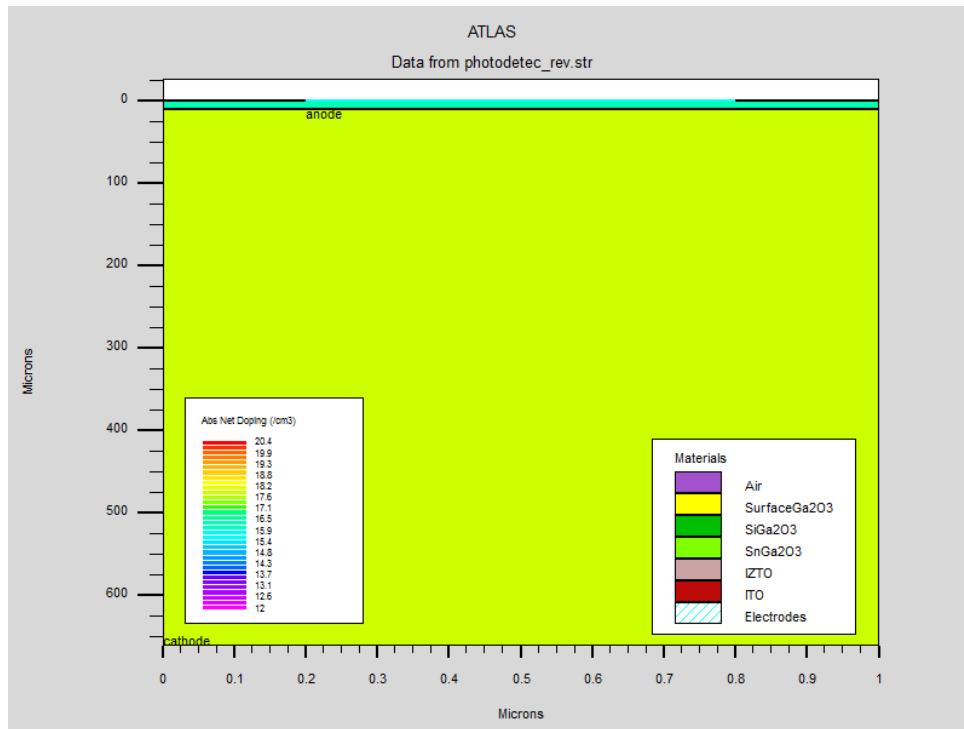

Figure 3.9: Doping profile.

In this statement, the acceptor designates the type of trap, while "x.min", "x.max", and "y.min", "y.max" specify the edges of the region where the traps are located, "e.level" pinpoints the energy level of traps concerning the conduction band for acceptor traps or the valence band for donor traps in eV, "density" specifies the concentration of trap centers in cm^{-3}, "degen" denotes the degeneracy factor, and "sign", and "sigp" define the capture cross-sections for electrons and holes in cm^2, respectively.

3.3.2.2 Materials and models specification

Once the structure is defined, it's crucial to specify the material characteristics, especially when the material is not predefined in the SILVACO-ATLAS database, the following line of code exemplifies the SILVACO-ATLAS syntax for material definition [208]:

```
material mat=SnGa2O3 EG300=4.8 affinity=4 user.Default=GaN USER.GROUP= \
SEMICONDUCTOR MUN=172 MUP=10 Nc300=3.7e18 Nv300=5e18 permittivity=12.6  \
VSATN=1e7 TAUN0=1e-9 TAUP0=1e-9  d.tunnel=1e-5  INDX.IMAG=Ga2O3.k INDX.REAL\
=Ga2O3.n
```

Where "mat" serves as the identifier for the material, "EG300" represents the semiconductor band gap in eV, while "affinity" indicates the electronic affinity in eV. "MUN" and "MUP" correspond to the electron and hole mobilities in $cm^2/V.s$, "Nc300" and "Nv300" refer to the effective density of states for electrons and holes in cm^{-3}, respectively. In addition "permittivity" stands for the relative dielectric permittivity of the material, "VSATN" denotes the saturation velocity for electrons in cm/s, "TAUN0" and "TAUP0" specify the SRH lifetime for electrons and holes respectively, "d.tunnel" sets the maximum tunneling distance for UST model in cm. Finally, "INDX.IMAG=Ga2O3.k" "INDX.REAL=Ga2O3.n" is the refractive index nk of the material.

To achieve simulation results that closely align with reality it's essential to consider numerous intricate dependencies of device properties, SILVACO-ATLAS offers independent models that describe each device property dependency individually allowing them to be activated separately, the results' precision relies on the selection and implementation of accurate physical models throughout the simulation process [208].

Physical models are specified through the models statement, as in the following example:

```
models print temp=300 kla srh bgn fldmob conmob Auger UST BBT.STD bb.a=8e7 \
bb.b=9e6 bb.gamma=2.6 incomplete inc.ion FERMIDIRAC
impact selb AN1=7.03e5 AN2=7.03e5 AP1=6.71e5 AP2=1.58e6  BN1=1.231e6 \
BN2=1.231e6 BP1=1.693e6 BP2=2.03e6 BETAN=1 BETAP=1 EGRAN=4e5
impact aniso e.side be0001=2.18e4 bh0001=2.03e4 ae0001=3.82e4 ah0001=3.10e4
```

The following is an explanation of the different models that were used in this thesis:

➤ **Kla:** Klassen's model offers a comprehensive depiction of both majority and minority carrier mobilities, this encompassing description accounts for lattice scattering, impurity scattering (with screening from charged carriers), carrier-carrier scattering, and the effects of impurity clustering at elevated concentrations [209].

➤ **Srh:** Specifies SRH recombination model utilizing predetermined lifetimes (see section 3.2.3.1).

➤ **Bgn:** Bandgap narrowing model in the presence of substantial doping the energy range undergoes a dependence on the doping level [210, 211], as the doping concentration rises, there is a concurrent reduction in the separation of E_g, this phenomenon arises from the conduction band experiencing a lowering effect approximately equal to the rise observed in the valence band. The SILVACO-ATLAS system captures this behavior through simulation employing a spatially varying intrinsic concentration by relationship:

$$n_{ie}^2 = n_i^2 \exp\left(\frac{\Delta E_g}{K_B T}\right) \tag{3.32}$$

Where n_i is intrinsic concentration, ΔE_g is variation in E_g, T is temperature, and K_B is Boltzmann constant.

➤ **Fldmob:** Parallel electric field-dependent mobility model, when carriers experience acceleration in an electric field their velocity tends to saturate as the electric field magnitude increases, to accurately represent this, it's essential to consider a reduction in effective mobility, this is because the magnitude of the drift velocity is the product of mobility and the electric field component in the direction of the current flow. The dependence of parallel electric field mobility of electrons and holes in this model is articulated as follows [212]:

$$\mu_n(E) = \mu_{n0}\left[\frac{1}{1+\left(\frac{\mu_{n0}E}{V_{\text{satn}}}\right)^{\gamma_n}}\right]^{\frac{1}{\gamma_n}} \tag{3.33}$$

$$\mu_p(E) = \mu_{p0}\left[\frac{1}{1+\left(\frac{\mu_{p0}E}{V_{\text{satp}}}\right)^{\gamma_p}}\right]^{\frac{1}{\gamma_p}} \tag{3.34}$$

Where γ_n and γ_p are constants, E is the electric field, μ_{no} and μ_{po} are the total electron and hole mobilities, V_{satn} and V_{satp} are the electron and hole saturation velocities, respectively.

➤ **Conmob:** The concentration-dependent mobility model specifies the adoption of a mobility model contingent on concentration for semiconductors [208], it is often expressed using the following expression:

$$\mu = \mu_0\left(\frac{n}{n_0}\right)^{-\alpha} \tag{3.35}$$

Where represents μ the mobility of charge carriers, μ_0 is intrinsic mobility, n is the carrier concentration, n_0 is intrinsic carrier concentration, and α is the experimentally determined mobility exponent varying with the material.

➤ **Auger:** Specifies that Auger recombination model (see section 3.2.3.2).

➤ **UST:** The universal Schottky tunneling model (see section 3.2.6).

➤ **BBT.STD:** Band-to-band tunneling (standard) model (see section 3.2.6.1).

➤ **Incomplete inc.ion:** Incomplete ionization model, at RT during simulations, the semi-

conductor is typically assumed to be fully ionized with impurities. However, with decreasing temperature, the assumption of complete ionization becomes untenable. In such instances, the temperature-dependent behavior of ionized impurities is represented using Fermi-Dirac statistics, and the concentrations of ionized donor and acceptor impurities are then determined as follows [198]:

$$N_d^+ = \frac{N_d}{1 + G_{CB}\exp\left(\dfrac{E_{Fn} - (E_C - E_{DB})}{K_B T}\right)} \tag{3.36}$$

$$N_a^- = \frac{N_a}{1 + G_{VB}\exp\left(\dfrac{E_V - (E_{Fp} - E_{AB})}{K_B T}\right)} \tag{3.37}$$

Where E_{DB} and E_{AB} are the dopant activation energies, GCB and GVB are the degeneracy factors for the conduction and valence bands, N_d and N_a are the net compensated n-type and p-type doping, respectively.

➤ **FERMIDIRAC:** Fermi-Dirac model, indicates the utilization of Fermi-Dirac carrier statistics, electrons in thermal equilibrium at temperature "T" with a semiconductor lattice adhere to Fermi-Dirac statistics, this implies that the probability denoted as $f(E)$ of an available electron state with energy "E" being occupied by an electron is given by [213]:

$$f(E) = \frac{1}{1 + \exp\left(\dfrac{E - E_F}{K_B T}\right)} \tag{3.38}$$

Where E_F represents a spatially independent reference energy known as the Fermi level, and K_B is Boltzmann's constant, T is the temperature.

➤ **Impact selb:** The impact ionization model outlined by Selberherr, Selberherr's impact ionization model serves to elucidate the avalanche breakdown phenomenon, this breakdown transpires when electrons and/or holes traversing the space charge region garner adequate energy from the electric field, generating electron-hole pairs through collisions with atomic electrons within the depletion region, the newly formed electrons and holes propelled in opposite directions by the electric field give rise to a reverse-biased current. Furthermore, these newly generated electrons and/or holes may amass enough energy to ionize other atoms, initiating the cascade effect known as the avalanche process. Selb model, applied to elucidate avalanche breakdown is specifically defined by certain coefficients of both electrons and holes, these coefficients play a crucial role in capturing and describing the intricate dynamics of impact ionization within the semiconductor material [208]:

$$\alpha_n = A_n \exp\left[-\left(\frac{B_n}{E}\right)^{\beta_n}\right] \tag{3.39}$$

$$\alpha_p = A_p \exp\left[-\left(\frac{B_p}{E}\right)^{\beta_p}\right] \tag{3.40}$$

Where E is the electric field it is the strength of the electric field in the direction of current flow at a specific position within the structure. The parameters A_n, A_p, B_n, B_p, β_n, and β_p integral to the impact statement, come with predefined default values.

➤ **Impact aniso e.side:** Impact ionization anisotropic model as a function of the electric field along the side, determined by ionization rates that account for anisotropic effects, the ionization rate is characterized by the following equations [214]:

$$\alpha(E_x E_y) = a \exp\left(c - \sqrt{1 - A^2 c^2 \left(\frac{E_x E_y}{b_x b_y}\right)^2}\right) \tag{3.41}$$

$$A = \ln\left(\frac{a_y}{a_x}\right) \tag{3.42}$$

$$c = \left(\frac{E_x^2}{b_x^2} + \frac{E_y^2}{b_y^2}\right) \tag{3.43}$$

$$a = a_x^{\frac{c^2 E_x^2}{b_x^2}} \cdot a_y^{\frac{c^2 E_y^2}{b_y^2}} \tag{3.44}$$

In these equations, E_x and E_y represent the magnitude of the electric field in the x and y directions, respectively. The parameter values a_x, a_y, b_x, and b_y are contingent upon the crystal orientation.

➤ **Temp=300:** A model that establishes the operational temperature of the system during simulation. In this thesis, RT was used (T=300 K) in the simulation.

➤ **Print:** Prints the status of all models, an array of coefficients, and constants.

There are also other models taken into account in various ways, such as:

✶ **Thermionic emission model:** To activate the thermal emission model, you can specify the "surf.rec" parameter within the "contact" statement [208].

✶ **Image-force lowering model:** To activate the image-force lowering model, you can enable it by using the "barrier" parameter in the "contact" statement [208].

✯ **Fermi level pinning model:** The Fermi level pinning model can automatically activate when considering M/S interfacial traps [208].

3.3.2.3   Numerical method selection

SILVACO-ATLAS provides various numerical methods to calculate the solutions to semiconductor device problems, the main types of these numerical methods are "GUMMEL", "NEWTON", and "BLOCK" [208]. The GUMMEL method operates by sequentially solving for individual unknowns while holding other variables constant repeating this process until a stable solution is reached. In contrast, the NEWTON method tackles the complete set of unknowns simultaneously. The BLOCK method blends elements of both approaches, employing the GUMMEL method for certain equations and the NEWTON method for others. The NEWTON method is generally preferred and automatically employed as the default unless otherwise specified, it has been chosen as the simulation method for this work. To specify the solution method, a Method statement is used [208]:

```
method NEWTON
```

SILVACO-ATLAS can solve either the continuity equations for electrons and holes, both, or neither, depending on your preference. This decision can be made through the utilization of the "CARRIERS" statement [208], for instance:

```
method CARRIERS=2 #(for electrons and holes)
```

All parameters related to the solution process are adjustable the most important of which are "maxtrap", and "itlim", these parameters determine the maximum number of tries, and "climit" specifies minimal values of concentrations to be resolved by the solver [208], for example:

```
method maxtrap=30 itlim=50 climit=1e-4
```

3.3.2.4   Solution specification

SILVACO-ATLAS can compute solutions for small signal DC, AC, and transient solutions. Typically, these solutions are derived when voltages are applied to both device electrodes. SILVACO-ATLAS determines the current flowing through each electrode, and internal parameters like carrier concentrations and electric fields across the device. Throughout simulations, the device begins with zero bias on all electrodes, and solutions are acquired by incrementally adjusting the biases on the electrodes from this initial equilibrium state. The preservation of results is accomplished through the utilization of "save" statement [208].

The characteristics computed by SILVACO-ATLAS will be saved in "log" files including currents and voltages for each electrode in simulations [208], for example the statement:

```
log outf = photodetector.log
```

To achieve convergence for the equations used it is necessary to make an initial estimate of the variables to be evaluated at each bias point [208], the statement explains it:

```
solve init
```

Since we are simulating a UV photodetector there must be light for the process to take place, the illumination turns on by assigning the beam intensity on a solve statement as follows [208]:

```
beam num=1 x.orig=0.5 y.orig=-0.5 angle=90 wavelength=0.255
solve b1=1e-3
```

In this statement, "num=1" denotes the beam number, "x.orig=0.5", and "y.orig= -0.5" signify the beam coordinates, the determination of the beam propagation angle is based on the parameter "angle", and the wavelength specified as "0.255" corresponds to the wavelength utilized in the spectrum.

Solution and structure files provide the device with a particular bias point, enabling us to visually represent any evaluated parameter within the device structure. The save statement captures all node point details and saves them in an output file [208], the following is an example of the "save" statement:

```
save outfile=photodetector.str
save outfile=photodetector.log
```

Finally, we can activate the voltage at the electrode of the device using the cathode as an illustrative example, as shown in the following statement [208]:

```
solve vcathode=0 vstep=0.1 vfinal=3 name=cathode
```

3.3.2.5   Results analysis

Once the solution is identified and stored in files you can extract the information as numerical values providing the opportunity for a graphical representation [208]. The "extract" statement facilitates the extraction of device parameters in numerical form operating on the previously solved curve or structure file, the subsequent statement serves as an illustrative example of an "extract" statement [208].

```
extract name="IVrevlight255" curve (v."cathode"*-1, i."anode"*-1)
```

The last step is to sketch the saved files, the process is done using the "tonyplot" statement, and the following is an example of drawing the structure file and curve file [208]:

```
tonyplot photodetector.str
tonyplot IVrevlight255.dat
```

In Figure 3.10 (a) and (b), the simulated structure and the variation of current density against the applied reverse bias are depicted under 255 nm illumination through the "tonyplot" statement.
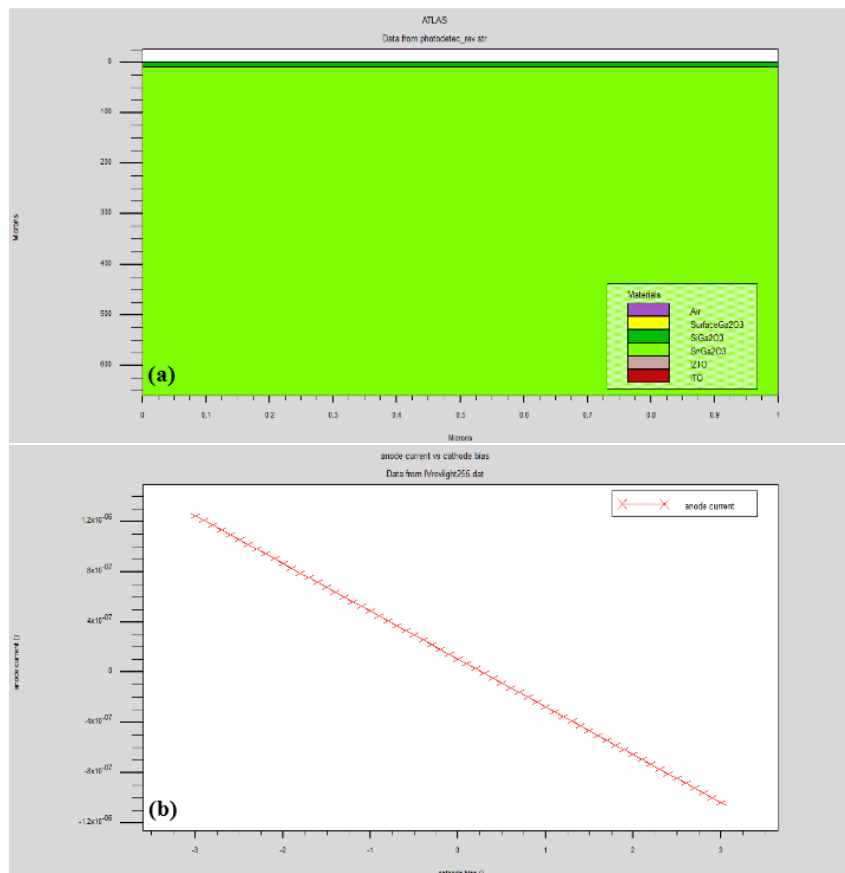
Figure 3.10: **(a)** The plotted simulated structure. **(b)** The extracted current density versus the applied reverse bias.

Chapter 4: Results and discussion
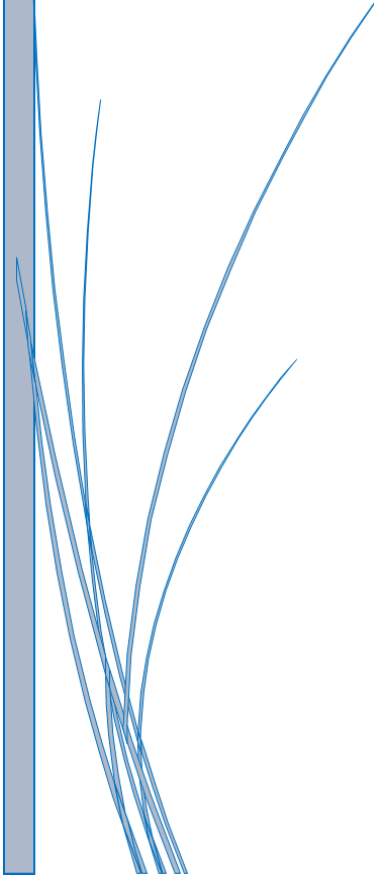
Chapter 4

Results and discussion

4.1 Introduction

This chapter conducts a simulation to investigate a fully transparent β-Ga$_2$O$_3$ Schottky barrier ultraviolet photodetector (SB UV-PhD). The device architecture is selected based on recent research by H. Kim et al [22]. Their work displayed a fully transparent β-Ga$_2$O$_3$ SB UV-PhD utilizing high-quality amorphous IZTO for the Schottky contact and ITO for the ohmic contact. The SB UV-PhD exhibited stable photo-response performance, low dark current, rapid photodetection, high responsivity, significant rectifying ratio, and self-powered operation [22].

The chapter was structured into two main parts. The first part involved simulating the J-V characteristic under reverse bias and assessing their responsivity across different wavelengths (255 nm, 385 nm, 500 nm, and dark conditions). This section also included a comprehensive analysis of the PPC phenomenon and its correlation with traps. The photodetector's performance was also optimized by introducing an $(Al_{0.39}Ga_{0.61})_2O_3$ passivation layer.

The second part of the chapter focused on three sequential optimizations. Initially, substituting the β-Ga$_2$O$_3$:Sn substrate with 4H-SiC was proposed, followed by incorporating a 4H-SiC intrinsic buffer layer to minimize surface defects between the β-Ga$_2$O$_3$:Si (drift layer) and 4H-SiC (substrate). These modifications were aimed at enhancing the photodetector's efficiency. Subsequently, the IZTO Schottky contact was suggested to be replaced by Graphene, an organic material known for its high electrical conductivity and optical transmittance across all wavelengths. Finally, the impact of elevated operating temperatures on the photodetector's performance was investigated.

The study employed the SILVACO-ATLAS numerical simulation tool to conduct comprehensive analyses. The Key focus was placed on calculating essential characteristics including the current density-voltage (J-V) characteristic, responsivity, and IQE. Additionally, the study extracted other pertinent metrics such as time-dependent photo response (T-D PhR),

and relationships between current density, responsivity, IQE, and light power density. These simulations were crucial in deepening understanding of the fundamental factors influencing the device's operational performance.

4.2 Device structure and modelling

The SB UV-PhD device was constructed on a single-crystal bulk Sn-doped β-Ga$_2$O$_3$ wafer (β-Ga$_2$O$_3$:Sn), which has a thickness of 650 μm and a doping concentration ($N_d - N_a$) of $1.0{\times}10^{18} cm^{-3}$. Following this, a Si-doped β-Ga$_2$O$_3$ layer (β-Ga$_2$O$_3$:Si) was grown via HVPE, measuring 10 μm in thickness with a doping concentration ($N_d - N_a$) of $3.0{\times}10^{16} cm^{-3}$. An ITO electrode was sputtered onto the bottom surface of the β-Ga$_2$O$_3$:Sn substrate to function as an Ohmic contact. The Schottky contact was then formed by depositing IZTO onto the β-Ga$_2$O$_3$:Si drift layer using a two-faced target co-sputtering technique at RT. Figure 4.1 illustrates the schematic representation of the SB UV-PhD structure. During experimentation, an LED light source emitted specific wavelengths (255 nm, 385 nm, 500 nm) with a power density of 1 mW/cm^2 [22].
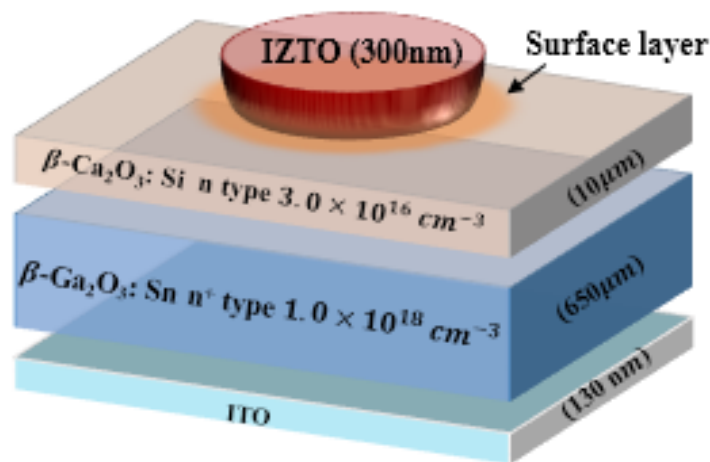
Figure 4.1: Schematic representation of SB UV-PhD structure [22].

The input materials parameters and input traps parameters in the simulation process of the studied SB UV-PhD are listed in Table 4.1, and Table 4.2, respectively.

Table 4.1: Physical input materials parameters in the simulation process.

Parameters	β-Ga$_2$O$_3$:Sn [35, 215]	β-Ga$_2$O$_3$:Si [35, 215]	Surface Layer [35, 215]	(Al$_{0.39}$Ga$_{0.61}$)$_2$O$_3$ Passivation Layer [216]	IZTO [22]	4H-SiC [217]	Graphene [218, 219]
E_g **(eV)**	4.8	4.8	4.8	5.48	3.6	3.26	/
χ **(eV)**	4.0	4.0	3.85	3.35	/	3.6	/
μ_p **(cm^2/V.s)**	10	10	10	10	/	115	/
μ_n **(cm^2/V.s)**	172	300	300	300	10.83	900	9000
ε	12.6	11	11	11	/	9.7	/
N_C **(cm^{-3})**	3.7×10^{18}	3.7×10^{18}	3.7×10^{18}	3.7×10^{18}	/	1.7×10^{19}	/
N_V **(cm^{-3})**	5.0×10^{18}	5.0×10^{18}	5.0×10^{18}	5.0×10^{18}	/	2.5×10^{19}	/
N_d **(cm^{-3})**	1.0×10^{18}	3.0×10^{16}	3.0×10^{16}	3.0×10^{16}	2.8×10^{20}	1.0×10^{18}	/
Thickness (μm)	650	10	0.01	0.05	0.3	650	3.0×10^{-4}
Workfunction (eV)	/	/	/	/	4.79	/	4.0–4.8
Resistivity ($\Omega \cdot cm$)	/	/	/	/	4.86×10^{-4}	/	2.0×10^{-4}

Table 4.2: Traps parameters used in the simulation process.

	$E_T(eV)$	$N_T(cm^{-3})$	$\sigma_n(cm^2)$	σ_n / σ_p	**Refs**
β-Ga$_2$O$_3$:Si drift layer	0.75	9×10^{15}	2×10^{-14}	100	[35, 215, 220, 221]
	1.05	9×10^{15}	2×10^{-14}	10	
β-Ga$_2$O$_3$:Sn bulk layer	0.55	4.9×10^{16}	2×10^{-14}	100	[35, 215, 220, 221]
	0.74	4.9×10^{17}	2×10^{-14}	100	
	1.04	5.0×10^{17}	2×10^{-14}	10	
4H-SiC bulk layer	0.80	5.0×10^{17}	1.5×10^{-15}	100	[222]
	1.01	5.0×10^{17}	8.4×10^{-16}	10	

4.3 Reverse bias modeling

Figure 4.2 illustrates simulated J–V characteristic under reverse bias for different wavelengths, compared against experimental measurements [22]. The simulation results closely match the experimental data across various wavelengths, including 255 *nm*, 385 *nm*, and 500 *nm*, as well as under dark conditions. This agreement underscores the influence of material properties detailed in Table 4.1 and Table 4.2, as well as the physical models discussed in section 3.3.2.2.

The photocurrent is notably influenced by both photogeneration and recombination processes. Therefore, precise determination of the optical indices *n* and *k* was crucial for accurately assessing absorption. In terms of recombination, a relatively high density of traps
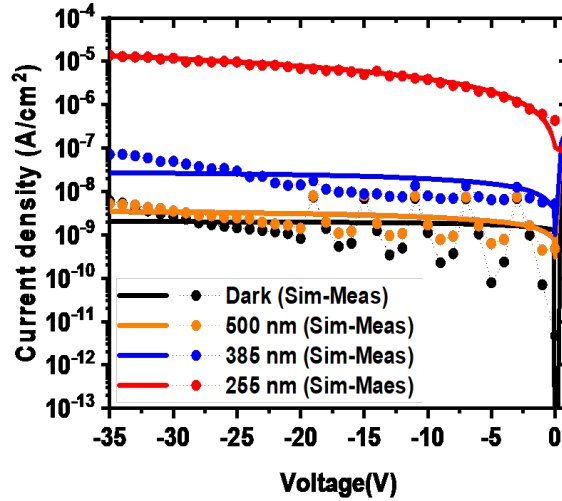
Figure 4.2: The simulated J–V characteristic at reverse bias for various wavelengths (solid lines) of the fully transparent β-Ga$_2$O$_3$ SB UV-PhD compared to measurements (symbols): data from reference [22].

has offered the most accurate alignment with experimental curves across all wavelengths (255 nm, 385 nm, and 500 nm). This can be justified by considering the high doping of the bulk region ($1.0 \times 10^{18} cm^{-3}$) and the dark current measurement, which falls between 10^{-9} to $10^{-8} A/cm^2$. This measurement is notably higher compared to the current range of 10^{-11} to $10^{-12} A/cm^2$ and is often associated with devices featuring very low defect densities [223], and a noteworthy PDCR exceeding 10^3 was achieved compared to other reported β-Ga$_2$O$_3$ SB UV-PhDs. This favorable ratio can be attributed to the complete transparency and thick bulk of the device, which effectively reduces optical losses through reflection or transmission.

Figure 4.3 illustrates the responsivity characteristics of β-Ga$_2$O$_3$ SB UV-PhD at various reverse voltages. A satisfactory fit with measurements was predominantly achieved at 255 nm, which is crucial as it lies within the solar-blind region for this wavelength. The device exhibited significant responsivity ranging from 10^{-4} to $10^{-3} A/W$. As the wavelength increases, the responsivity decreases, with 385 nm identified as the cut-off wavelength for the β-Ga$_2$O$_3$ SB UV-PhD. Moreover, higher responsivity can be achieved with increased reverse bias. However, due to its nature as a vertical Schottky diode and its self-powered configuration similar to a photovoltaic detector, the study is constrained to low biases.
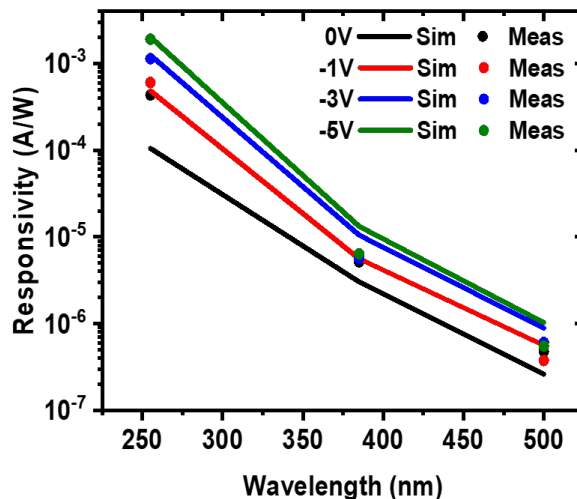
Figure 4.3: Responsivity versus wavelength at different reverse voltages (simulation - solid lines) (measurements - symbols): data from reference [22].

The photocurrent density versus light power density curve provides an assessment of the device's light detection capability. In Figure 4.4, the relationship between the photocurrent density and light power density is depicted for 255 nm and a reverse bias of -1V.

The β-Ga$_2$O$_3$ SB UV-PhD initiates light detection once the light power density exceeds $10^{-9}W/cm^2$. Subsequently, the current density shows a linear increase on the logarithmic scale until it saturates at (2-3)×$10^{-5}W/cm^2$, aligning closely with findings reported in [224].

The relationship between photocurrent I_{ph} and optical power P_{op} follows a power law expressed as $I_{ph} \propto P_{op}^{\gamma}$, in the initial linear region γ is approximately 0.85, whereas in the saturation region γ decreases to about 0.024. It is important to highlight that in the saturation region, the photocurrent is limited by various recombination processes, which will be discussed in detail later. The phenomenon of PPC, commonly observed in heterojunction devices including Schottky photodiodes persists even after the light source is turned off, this is usually associated with V_O defects that lead to the formation of shallow donor levels [22, 100, 223]. The most probable causes of the PPC phenomenon are photogenerated carriers from deep UV either trapped in these defect states or existing as free holes with limited mobility [225].

Figure 4.5 illustrates the transient response (T-D PhR) of β-Ga$_2$O$_3$ SB UV-PhD under 255 nm illumination with a 5s pulse width. The estimated decay time is 0.18s the photodetector demonstrates stability under both dark and illuminated conditions, showing minimal PPC effects. The transient decay is affected by the pulse width, which is influenced by the type and depth of traps, potentially leading to a delay in recovery time. Moreover, the switching characteristics remain robust even at very low operating voltages (-1V).
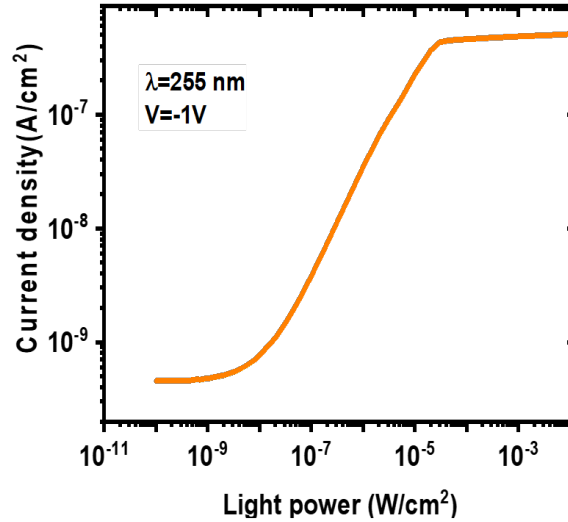
Figure 4.4: Photocurrent density versus light power density under 255 nm wavelength at -1 V.
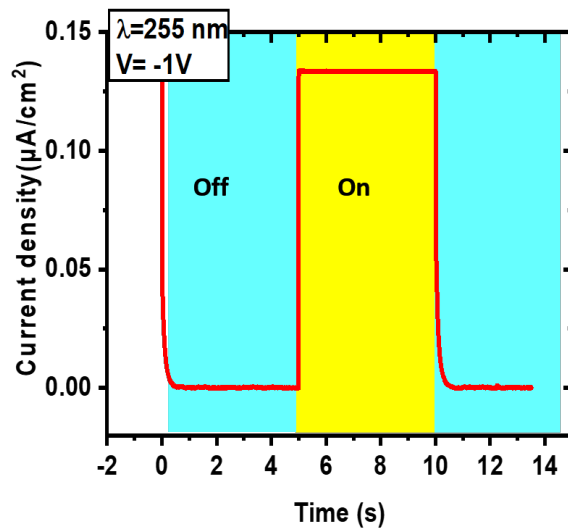
Figure 4.5: The T-D PhR under pulsed illumination of 255 nm at -1V.

4.4 Optimizations of β-Ga$_2$O$_3$ SB UV-PhD

4.4.1 Effect of reducing bulk traps density

4.4.1.1 J-V characteristic

This section elucidates the effect of reducing bulk traps density on the J-V characteristic of the SB UV-PhD. Figure 4.6 shows, the influence of traps density having energy levels of $E_T =$ 0.55 eV, $E_T = 0.74$ eV, and $E_T = 1.04$ eV on the photocurrent at a wavelength of 255 nm.

Based on the results obtained, it is clear that deeper traps play a significant role, with energy levels at 0.74 eV and 1.04 eV. This is logical because deeper traps enhance the efficiency of the recombination process.
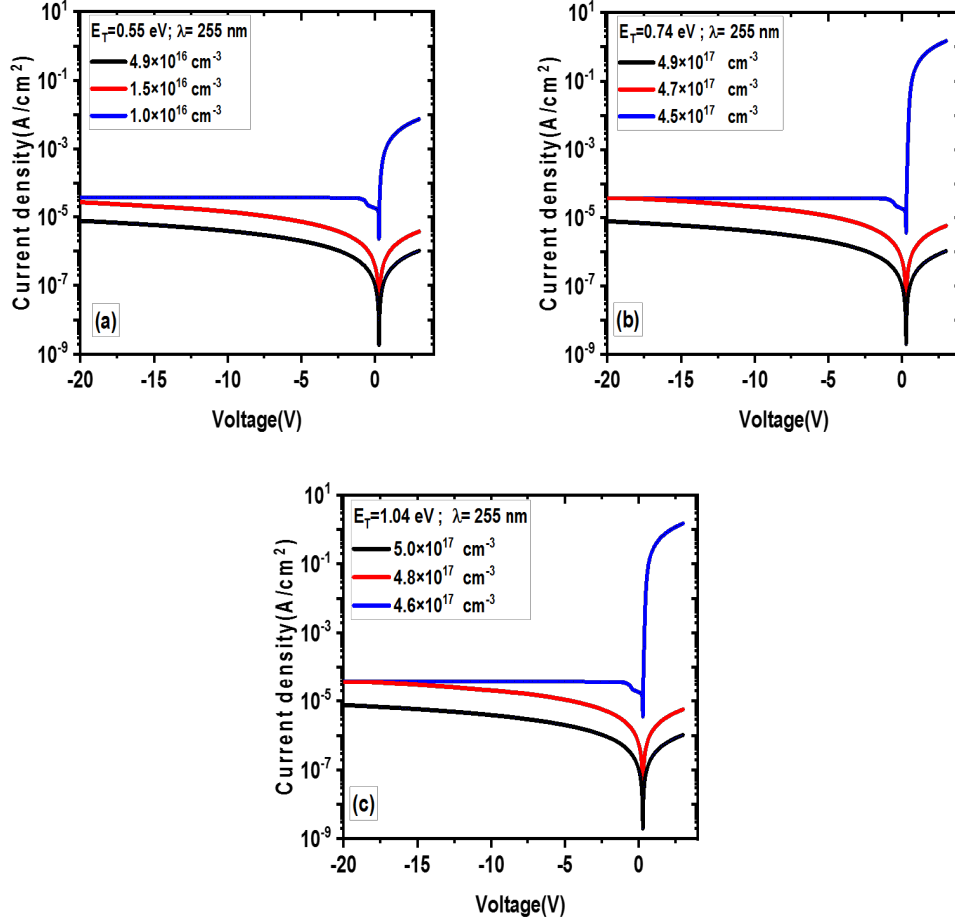
Figure 4.6: Effect of reducing bulk traps density (one by one), **(a)** $E_T = 0.55\ eV$, **(b)** $E_T = 0.74\ eV$, and **(c)** $E_T = 1.04\ eV$ on the J-V characteristic under 255 nm of β-Ga$_2$O$_3$ SB UV-PhD.

Each type of trap exhibits a threshold density beyond which further enhancement stops ($1.0\times10^{16} cm^{-3}$ for $E_T = 0.55\ eV$, $4.5\times10^{17} cm^{-3}$ for $E_T = 0.74\ eV$, and $4.6\times10^{17} cm^{-3}$ for $E_T = 1.04\ eV$).

The J–V characteristic loses its symmetric shape between reverse and forward bias, indicating the diode's rectifying behavior. At low traps density, there is a notable increase in photocurrent attributed to reduced recombination of photogenerated carriers [226]. In this case, the photodetector acts as a self-powered solar-blind photodetector.

4.4.1.2 The responsivity

The responsivity and rejection ratio from UV (255 nm) to visible light (500 nm) peak at 0.04 A/W and 8×10^4 at -1V, respectively, according to results plotted in Figure 4.7. A slight re-

duction in trap densities enhances the responsivity, while no further improvement occurs behind the cut-off wavelength of 385 *nm* for the three trap cases. Consequently, it is possible to presume that a minor reduction in the bulk traps density improves the device's light selectivity to be considered as a high-resolution solar blind.
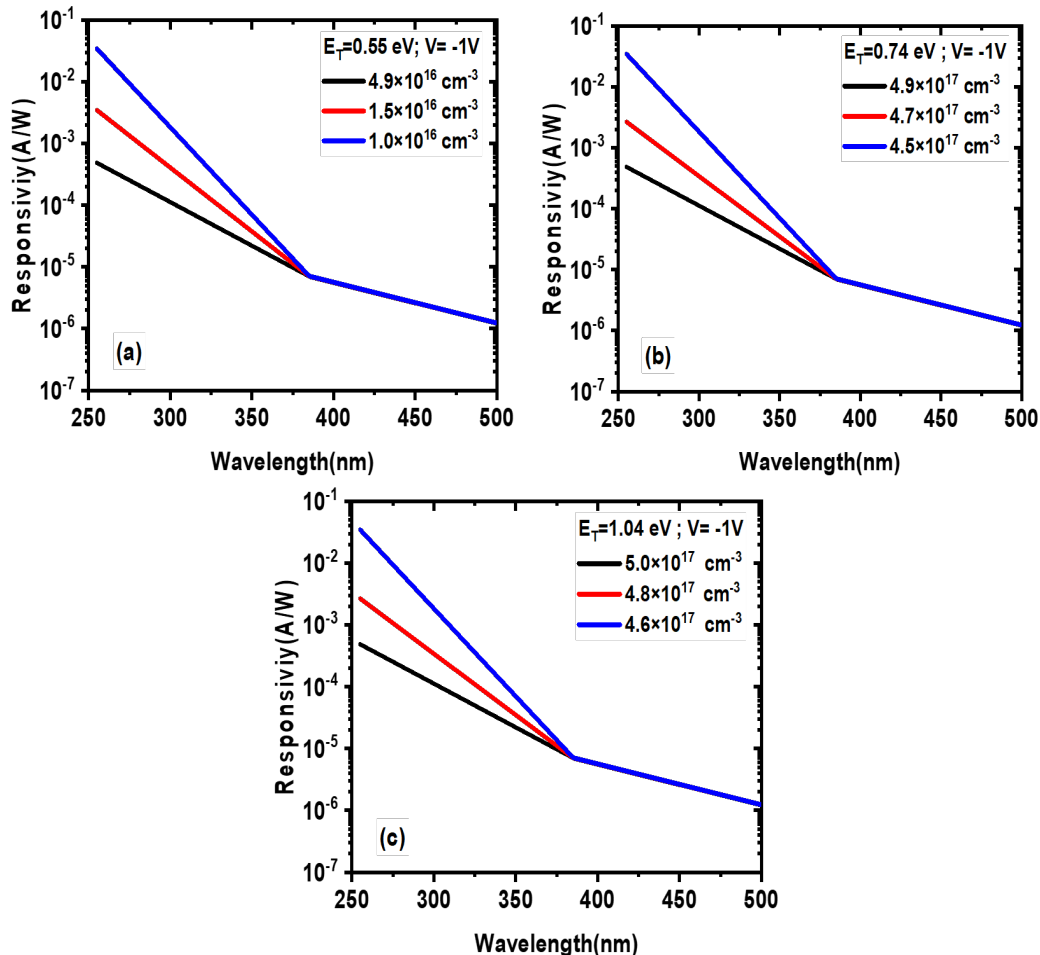
Figure 4.7: Effect of reducing bulk traps density (one by one), **(a)** $E_T = 0.55\ eV$, **(b)** $E_T = 0.74\ eV$, and **(c)** $E_T = 1.04\ eV$ on the responsivity at -1V of β-Ga$_2$O$_3$ SB UV-PhD.

4.4.1.3 Photocurrent density versus light power density

The impact of reducing traps density on photocurrent versus light power density is depicted in Figure 4.8. As the density of traps is reduced, the saturation zone decreases which is principally affected by recombination. When traps vanish entirely, at this point the linear dependence of current density versus light power density takes over the entire variation. This suggests that the saturation zone is primarily governed by SRH recombination.
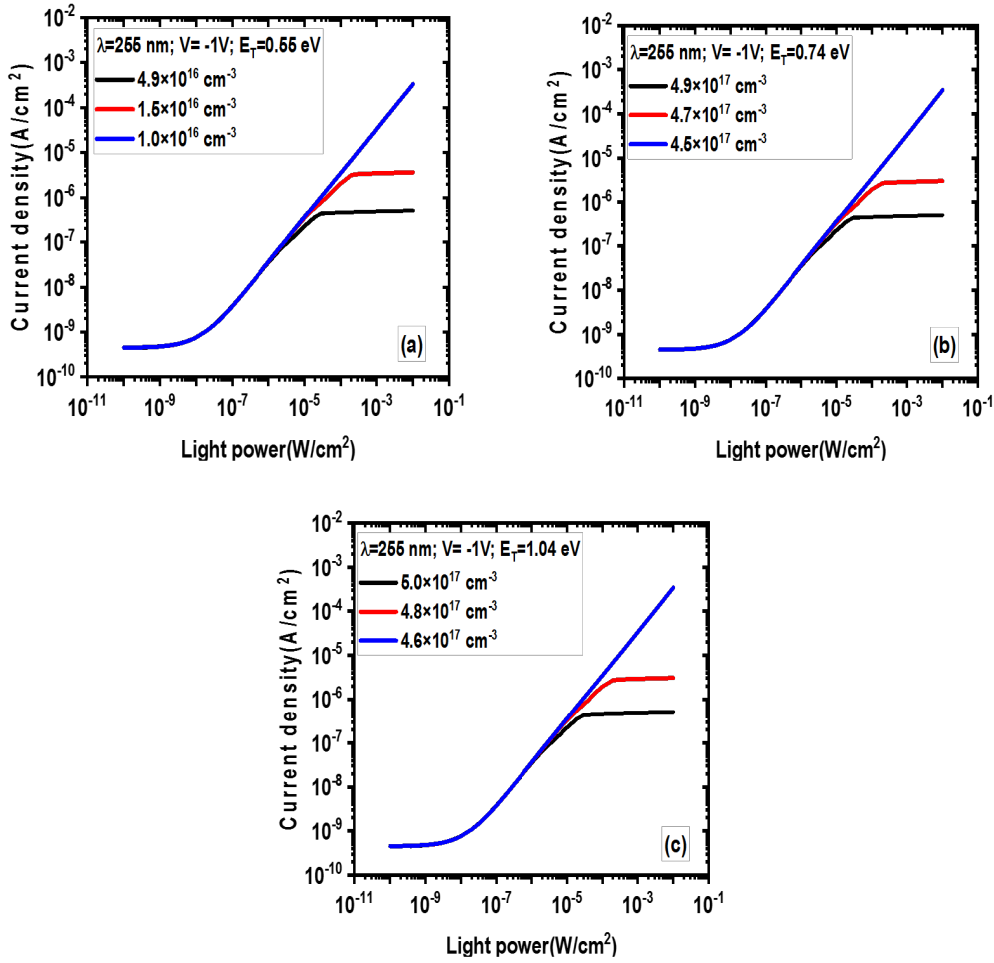
Figure 4.8: Effect of reducing bulk traps density (one by one), **(a)** $E_T = 0.55\ eV$, **(b)** $E_T = 0.74\ eV$, and **(c)** $E_T = 1.04\ eV$ on photocurrent density versus light power density under 255 nm at - 1 V in β-Ga$_2$O$_3$ SB UV-PhD.

4.4.1.4 Time dependency photo-response

The impact of reducing trap density on the speed and consistency of the device's response is now investigated by subjecting it to a short light pulse lasting 0.1 s, as shown in Figure 4.9. The PPC phenomenon undergoes notable suppression, leading to important response and decay speed improvements. The expected decay time for the lowest traps density, particularly for the deeper traps ($E_T = 0.74\ eV$ and $E_T = 1.04\ eV$), is approximately 0.05 s, while for $E_T = 0.55\ eV$, it is shorter than 0.015 s. In practical terms, traps density can be minimized through experimental processes such as annealing at various temperatures in an Ar atmosphere [151].
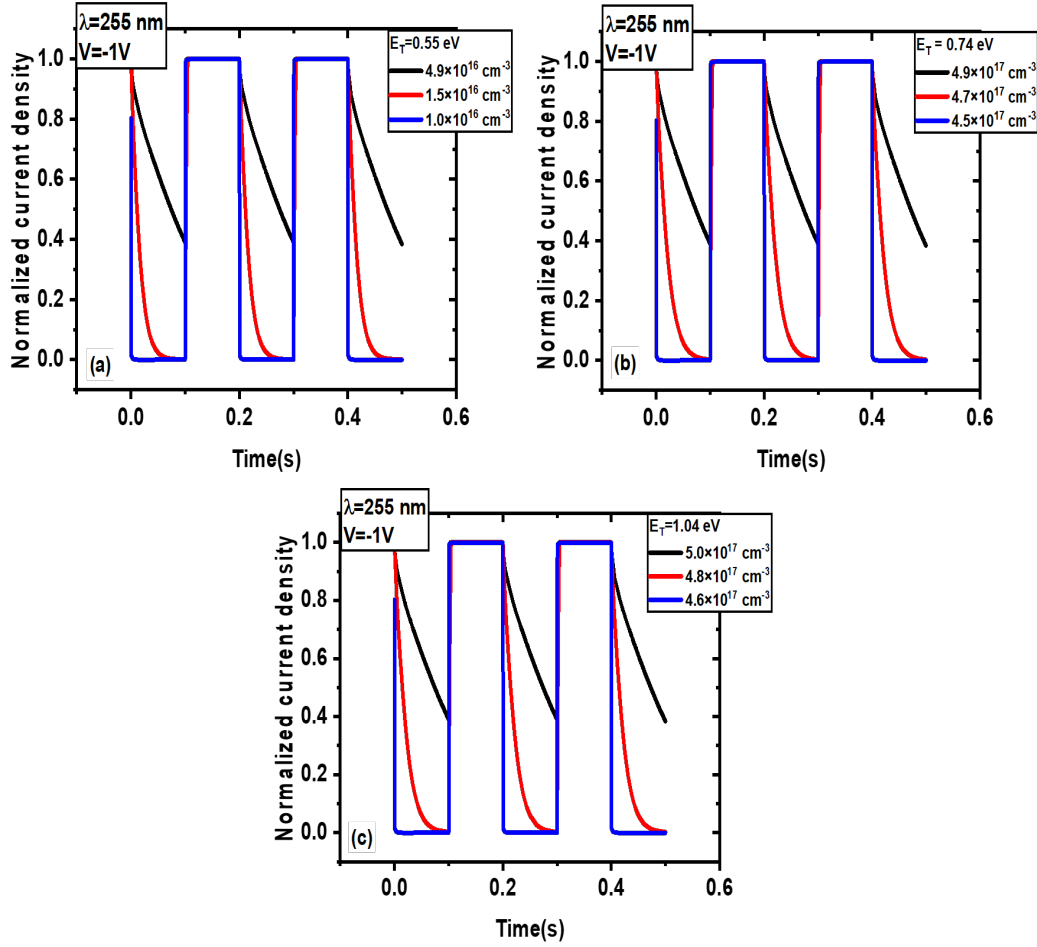
Figure 4.9: Effect of reducing bulk traps density (one by one), **(a)** $E_T = 0.55 \ eV$, **(b)** $E_T = 0.74 \ eV$, and **(c)** $E_T = 1.04 \ eV$ on T-D PhR under short-pulsed illumination of 255 nm at - 1 V in β-Ga$_2$O$_3$ SB UV-PhD.

4.4.2 Effect of inserting an (Al$_{0.39}$Ga$_{0.61}$)$_2$O$_3$ passivation layer

4.4.2.1 J–V characteristic

Modulating the Al fraction makes it possible to engineer E_g of (Al$_{0.39}$Ga$_{0.61}$)$_2$O$_3$. This capability allows for precise control of E_g within a broad range spanning from 4.8 to approximately 8.7 eV facilitating the development of wavelength-tunable opto-devices [216].

In light of this, a 50 nm thick (Al$_{0.39}$Ga$_{0.61}$)$_2$O$_3$ passivation layer is placed on top of the device between the IZTO photo-anode and the β-Ga$_2$O$_3$:Si drift layer. The (Al$_{0.39}$Ga$_{0.61}$)$_2$O$_3$ passivation layer features a WBG of 5.48 eV. To mitigate the impact of a pronounced E_g difference between the (Al$_{0.39}$Ga$_{0.61}$)$_2$O$_3$ passivation layer and the β-Ga$_2$O$_3$:Si drift layer, a lower Al fraction was deliberately selected this choice aims to minimize recombination within this layer. Furthermore, experimental observations revealed that an elevated Al content resulted in a transition from a monoclinic structure to a corundum structure in the crystal, and thus caused dislocations and interfacial states to occur [216, 227, 228]. The resulting J–V charac-

teristics are shown in Figure 4.10.
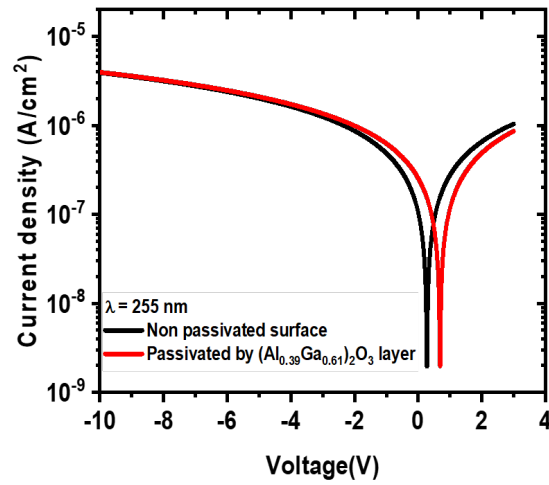
Figure 4.10: Effect of inserting an $(Al_{0.39}Ga_{0.61})_2O_3$ passivation layer on the J–V characteristic of β-Ga_2O_3 SB UV-PhD.

This passivation layer led to a noteworthy enhancement in photocurrent, accompanied by a shift towards forward voltage bias within the range of (-2,+2)V. This shift contributes to the augmentation of the self-powered feature of the device. The voltage region most significantly impacted ranges from (-2,+2)V, which can be attributed to the relatively thin thickness (50 nm) of the $(Al_{0.39}Ga_{0.61})_2O_3$ passivation layer.

4.4.2.2 The generation and recombination rates

The extraction of generation(G) and recombination (R) rates through the frontal region of the device, as depicted in Figure 4.11, reveals a marked decrease in the recombination rate at $(Al_{0.39}Ga_{0.61})_2O_3$ passivation layer.
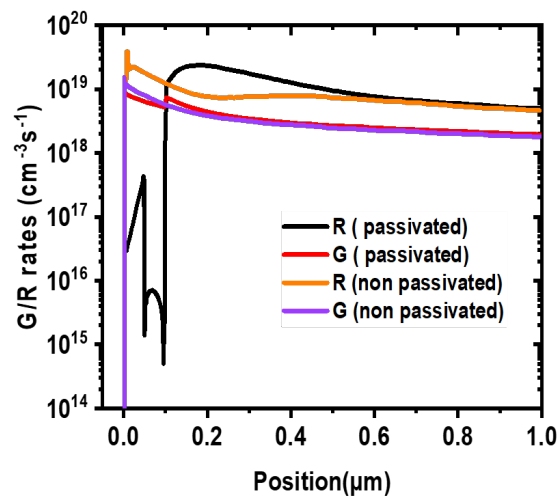
Figure 4.11: Effect of inserting an $(Al_{0.39}Ga_{0.61})_2O_3$ passivation layer on the generation and recombination rates in β-Ga_2O_3 SB UV-PhD.

The observed reduction in recombination rate at $(Al_{0.39}Ga_{0.61})_2O_3$ passivation layer can be attributed to its WBG. With identical defects (traps) as in β-Ga_2O_3, the WBG likely diminishes the impact of deep traps. Moreover, this passivation layer with its WBG improves light absorption in the β-Ga_2O_3:Si drift layer by minimizing surface reflection and as a result, an increase in the photocurrent occurs.

4.4.2.3   Internal quantum efficiency

The enhancements in photocurrent can also be elucidated by changes in the IQE. Figure 4.12 demonstrates an increase in IQE following the incorporation of the $(Al_{0.39}Ga_{0.61})_2O_3$ passivation layer at 0 V and -1 V, respectively.
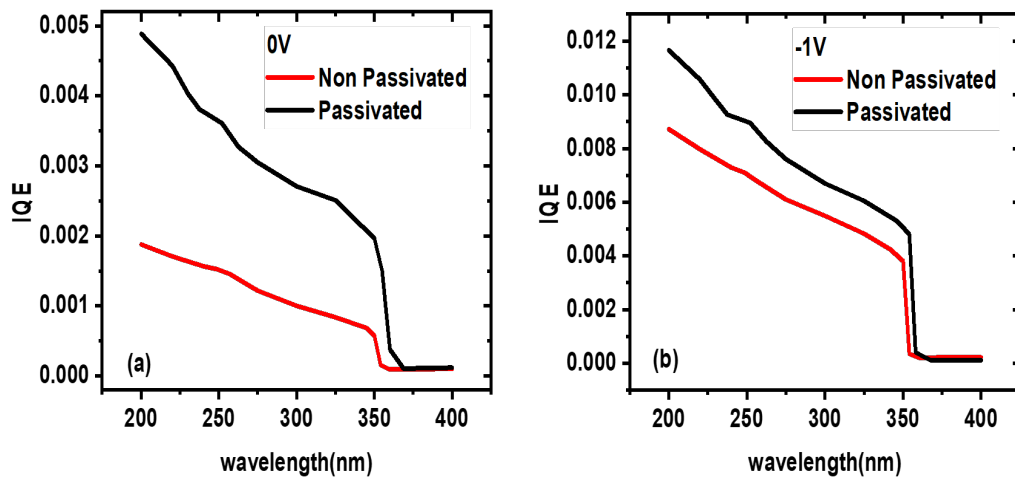
Figure 4.12: Effect of inserting an $(Al_{0.39}Ga_{0.61})_2O_3$ passivation layer on the IQE of β-Ga_2O_3 SB UV-PhD **(a)** at 0 V, **(b)** at -1 V.

4.4.2.4   Time-dependency photo-response

The enhancement in photocurrent has impacted the T-D PhR of the β-Ga_2O_3 SB UV-PhD as depicted in Figure 4.13, whereas the rise in photocurrent coincided with a shift toward forward voltage bias, leading to an additional PPC phenomenon at 0 V.

Therefore, in this study, adjusting the diode detection voltage to fall between 0 V and V_{off} is preferable. This adjustment is validated by the T-D PhR plot at 0.64 V, where a notable improvement in signal shape is evident.
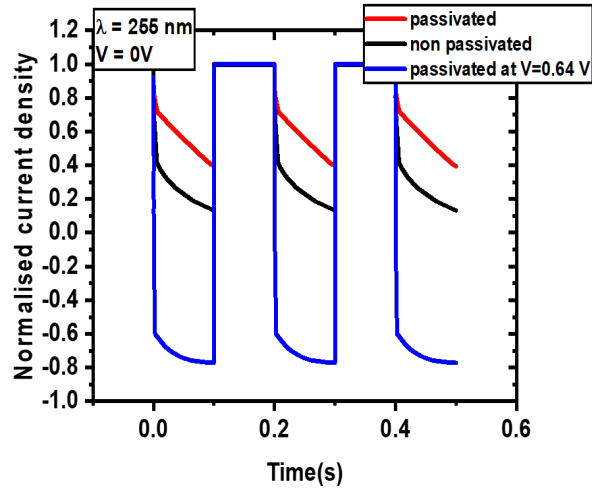
Figure 4.13: Effect of inserting an $(Al_{0.39}Ga_{0.61})_2O_3$ passivation layer on T-D PhR of β-Ga$_2$O$_3$ SB UV-PhD.

4.4.3   Effect of substituting β-Ga$_2$O$_3$:Sn substrate with 4H-SiC substrate

In this section, the optimization is based on using 4H-SiC as substrate [229]. β-Ga$_2$O$_3$ has demonstrated high-performance junctions when deposited on several substrates such as Ga$_2$O$_3$, Si, GaN, and 4H-SiC single-crystalline substrates [22, 230–232].

4H-SiC possesses impressive properties that contribute to its extensive use in various applications. The WBG of approximately 3.26 eV allows 4H-SiC to operate at high temperatures, making it suitable for demanding environments [217]. The material exhibits high thermal conductivity surpassing that of traditional semiconductors like Si enabling efficient heat dissipation in electronic devices [233]. In addition, 4H-SiC has a high breakdown electric field strength enhancing its performance in high-voltage applications [234], and good mechanical properties including its hardness and chemical stability [235].

The J-V characteristic was calculated based on the parameters of the 4H-SiC substrate listed in Table 4.1. The results are shown in Figure 4.14 for reverse and forward biases of (-3, 3) V, and compared to those obtained with β-Ga$_2$O$_3$:Sn substrate for different wavelengths (see section 4.3). The photocurrent is more significant when utilizing 4H-SiC substrate than the photocurrent with β-Ga$_2$O$_3$:Sn substrate at various wavelengths (255 nm, 385 nm, 500 nm). There is no notable disparity in current densities in reverse biases in the dark case. There is a noticeable contrast in the symmetry of the J-V curves between the β-Ga$_2$O$_3$:Sn substrate (particularly for 255 nm) and the 4H-SiC substrate. This is due to the fact that the intrinsic defects were taken into account for the β-Ga$_2$O$_3$:Sn substrate while not for the 4H-SiC substrate.
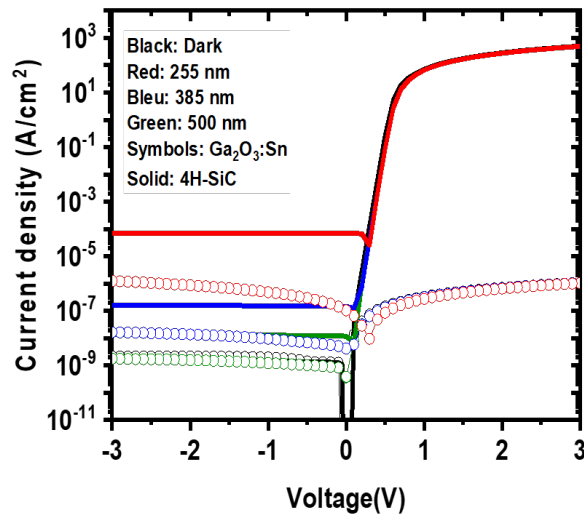
Figure 4.14: The simulated J-V characteristic at reverse and forward biases of the SB UV-PhD with 4H-SiC substrate (solid lines) compared to the β-Ga$_2$O$_3$:Sn substrate (symbols) at different wavelengths.

According to [222], the 4H-SiC substrate may also include certain intrinsic defects as outlined in Table 4.2. The symmetric J-V characteristic means that the current-voltage response for the photodetector is the same in both forward and reverse biases and it is often easier to design and work with because the response is uniform and the sensing is bidirectional [236, 237]. Consequently, we have introduced the intrinsic defects with suitable densities to achieve the desired symmetrical form and enhance the accuracy of the comparison with the earlier case using the β-Ga$_2$O$_3$:Sn substrate.
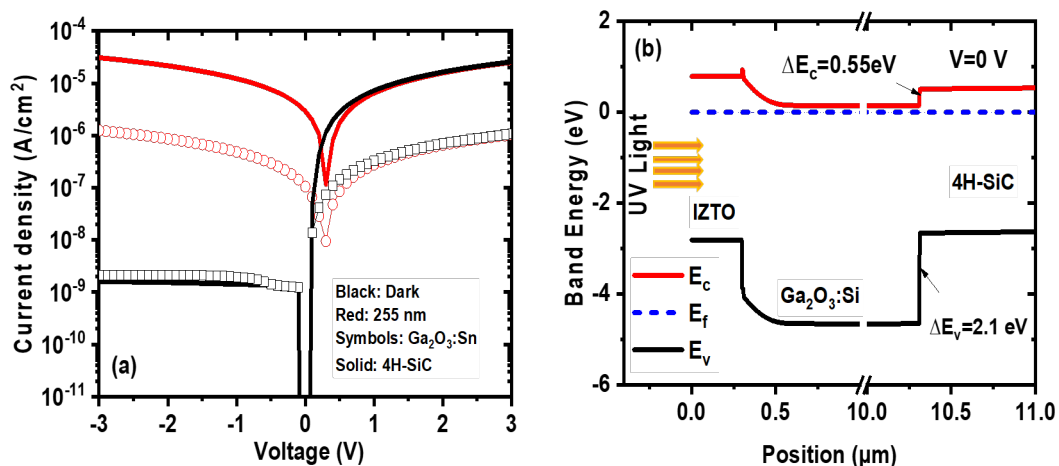
Figure 4.15: **(a)** Simulated symmetric J-V characteristic under 255 *nm* wavelength and at the dark for the SB UV-PhD with 4H-SiC substrate compared to the β-Ga$_2$O$_3$:Sn substrate. **(b)** The band energy diagram at V= 0V.

The results displayed in Figure 4.15 (a), demonstrate the symmetric shape of the J-V characteristic under a 255 *nm* wavelength for the SB UV-PhD with 4H-SiC substrate, which has

83

Results and discussion

provided the best response for both dark and illuminated cases. The improvement in the J-V characteristic observed with the 4H-SiC substrate can be attributed to the band energy diagram shown in Figure 4.15 (b), where the χ and E_g of β-Ga$_2$O$_3$:Si are reported to be 4.0 eV and 4.8 eV [35, 215], while for 4H-SiC they are 3.6 eV and 3.26 eV [217], respectively. Where ΔE_C is 0.55 eV while ΔE_V is 2.1 eV. This is similar to the ideal case reported in [232].

The n-type β-Ga$_2$O$_3$:Si has a WBG than n-type 4H-SiC and the gradual profile of the energy band encourages additional photo-generation of charge carriers under 255 nm of illumination, electrons transit from β-Ga$_2$O$_3$:Si to 4H-SiC when the heterojunction is created where an electrical accumulation layer is formed on one side of the 4H-SiC and a depletion layer is formed on the other side simultaneously. The study of the transport properties of the β-Ga$_2$O$_3$:Si/4H-SiC heterojunction mostly centers on electron behavior due to the n-type regions and the considerable difference in the offset discontinuity ΔE_V compared to ΔE_C. According to Y. Qu et al is estimated that there is a barrier $qV_b - \Delta E_C$ of 0.45 eV for conduction electrons in n-type 4H-SiC from β-Ga$_2$O$_3$:Si/4H-SiC heterojunction which facilitates the transfer of electrons [232].

Figure 4.16 (a) and (b) present the responsivity versus wavelength at 0 V and -1 V with β-Ga$_2$O$_3$:Sn (see section 4.3) and 4H-SiC substrates. It is observed that the photodetector with a 4H-SiC substrate shows improved responsivity of 0.003 A/W at 0 V and 0.012 A/W at -1 V along with a rejection ratio of approximately 10^3. However, the β-Ga$_2$O$_3$:Sn substrate has a rejection ratio of around 5×10^2. A comparison of the detectivity parameter between the 4H-SiC substrate and β-Ga$_2$O$_3$:Sn substrate at different wavelengths is also presented in Figure 4.16 (c). The detectivity decreases with increasing wavelength for both cases of substrates but its highest value reaches 5×10^{11} $Jones$ under 255 nm wavelength at -1 V for the 4H-SiC substrate.

Figure 4.17 (a) and (b), show the IQE versus wavelength at 0 V and -1 V for both cases of β-Ga$_2$O$_3$:Sn and 4H-SiC substrates. We notice an increase in all UV wavelengths while using a 4H-SiC substrate, especially at 255 nm, the values rise from 0.0015 to 0.042 at 0 V and from 0.007 to 0.17 at -1 V.

Figure 4.18 (a) displays, the comparison of T-D PhR at 255 nm and -1V of the SB UV-PhD with β-Ga$_2$O$_3$:Sn (see section 4.4.1.4) and 4H-SiC substrates, and Figure 4.18 (b) displays the T-D PhR under various wavelengths using a 4H-SiC substrate.

In Figure 4.18 (a), there is a significant difference in the current density between the two cases, as well as in the shape of the transient response. In the first case with β-Ga$_2$O$_3$:Sn substrate, it was remarked that the PPC phenomenon after the termination of the light source is important. The return to the baseline level is not immediate but with noticeable time decay constants almost $\tau_{d1} = 0.016s$, $\tau_{d2} = 0.02s$.
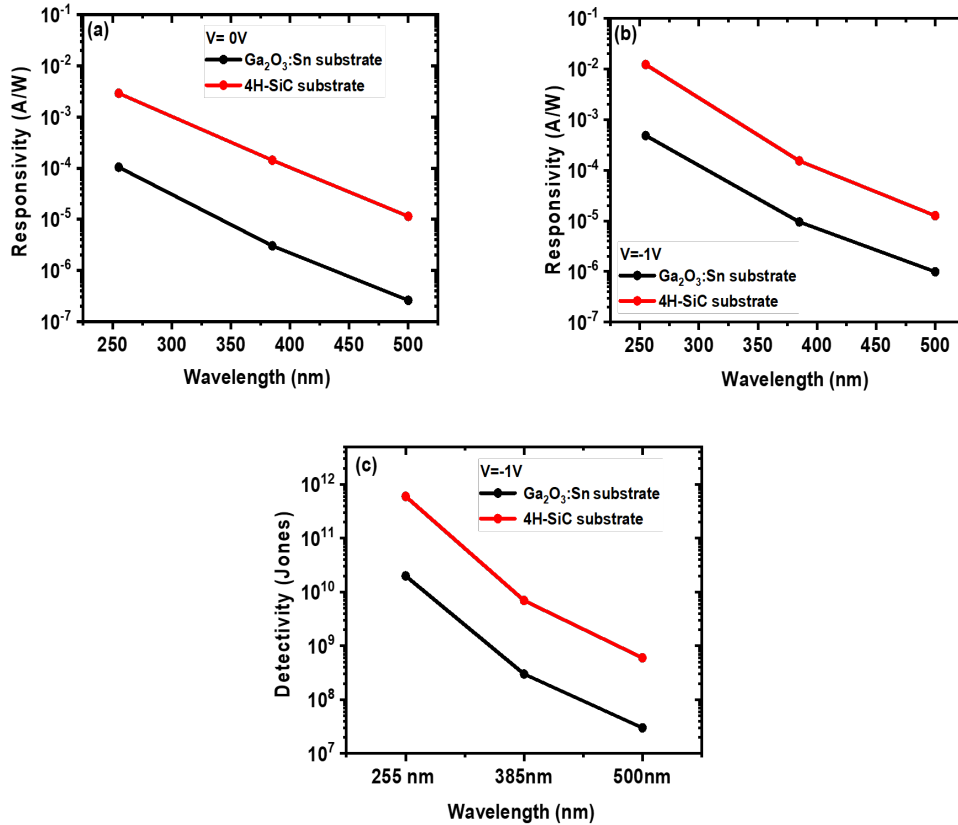
Figure 4.16: Comparison of responsivity versus wavelength between SB UV-PhD with 4H-SiC and β-Ga$_2$O$_3$:Sn substrates **(a)** at 0 V, **(b)** at -1 V.**(c)** Comparison of detectivity at different wavelengths between SB UV-PhD with 4H-SiC and β-Ga$_2$O$_3$:Sn substrates.
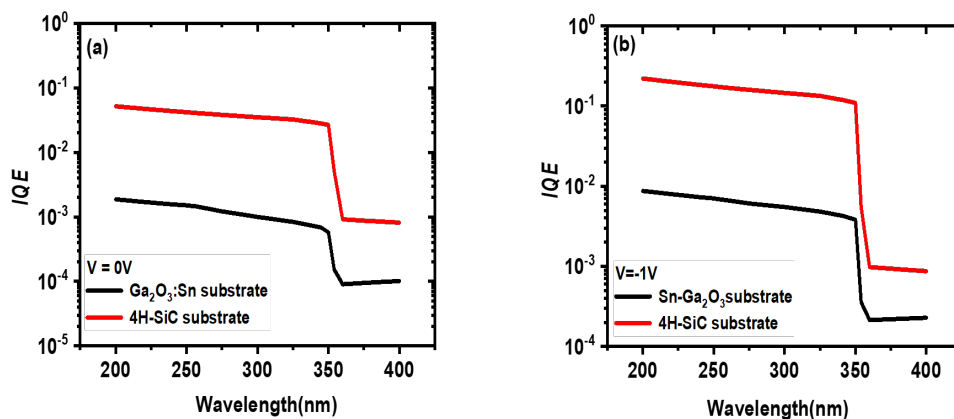
Figure 4.17: Comparison of IQE versus wavelength between SB UV-PhD with 4H-SiC and β-Ga$_2$O$_3$:Sn substrates **(a)** at 0 V, **(b)** at -1 V.

For the second case with 4H-SiC substrate, the photo-response is characterized by an immediate return to the baseline level. Consequently, in the SB UV-PhD with 4H-SiC substrate, the recombination and the collection are faster and so they return to the steady state. This

means that the efficiency of the overall response of the SB UV-PhD with 4H-SiC substrate is more suitable than with β-Ga$_2$O$_3$:Sn substrate for pulsed detection [113].
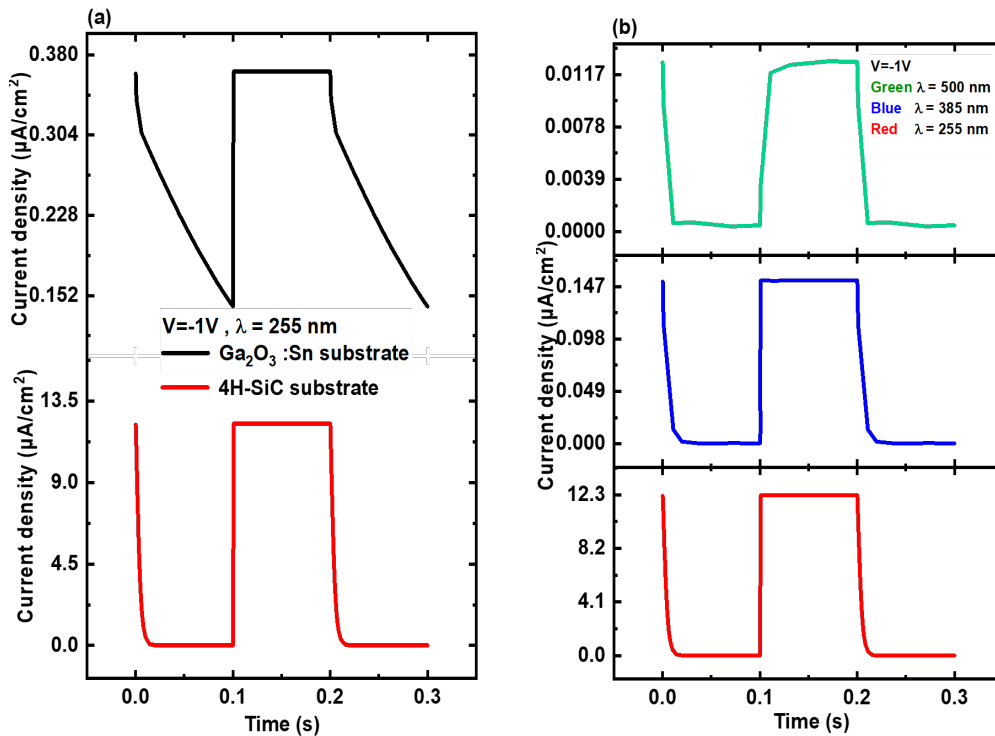
Figure 4.18: **(a)** Comparison of the T-D PhR under illumination 255 *nm* at -1 *V* between SB UV-PhD with 4H-SiC and β-Ga$_2$O$_3$:Sn substrates. **(b)** The T-D PhR under different wavelengths for SB UV-PhD with 4H-SiC substrate.

Figure 4.18 (b) displays, the T-D PhR of the SB UV-PhD on a 4H-SiC substrate under various light illumination wavelengths. The sensitivity to 255 *nm* light is significantly greater compared to 385 *nm* and 500 *nm*. The device shows consistent performance after numerous illumination cycles, demonstrating strong durability and reliable reproducibility, a similar finding was reported in [232].

Figure 4.19 (a), (b), and (c) show, the dependence of the photocurrent, responsivity, and IQE versus the light power density; at -1*V* and 255 *nm*. The light power density dependence of the photocurrent for SB UV-PhD with β-Ga$_2$O$_3$:Sn substrate was reported in section 4.3.

By using the 4H-SiC substrate, the onset detection threshold is comparable to that of the β-Ga$_2$O$_3$:Sn substrate ($10^{-9} W/cm^2$) but a higher current density is observed. The current densities increase roughly linearly with light power density on a logarithmic scale, saturation occurs outside of these ranges. For the β-Ga$_2$O$_3$:Sn substrate, the γ values are approximately 0.85 in the linear region and 0.024 in the saturation region. For the 4H-SiC substrate, they are around 0.72 in the linear region and 0.001 in the saturation region. Defect recombination

processes controlled the photocurrent in the saturation region, as was confirmed in detail in section 4.4.1.3.
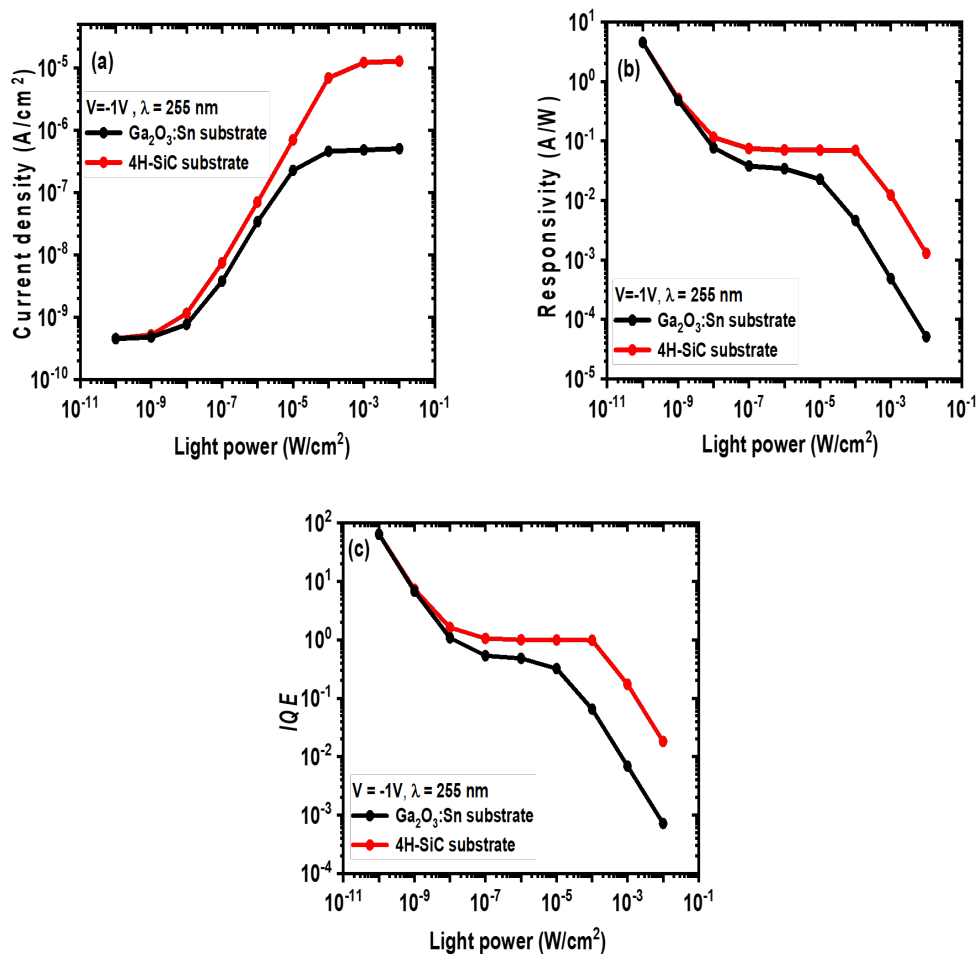
Figure 4.19: Comparison between SB UV-PhD with 4H-SiC and β-Ga$_2$O$_3$:Sn substrates of the dependence on the light power density for **(a)** photocurrent, **(b)** responsivity, and **(c)** IQE; at - $1V$ and 255 nm wavelength.

Responsivity and IQE show a similar change once they exceed the onset detection threshold. As the light power density increases, both the responsivity and IQE decrease, and this decrease indicates that saturation has occurred. Responsivity quantifies the efficiency of a photodetector in converting incoming light into electrical current. Saturation occurs when all charge carriers are already in motion, and more incident photons do not lead to a corresponding increase in current generation. This happens when the rate of photon absorption surpasses the carrier recombination rate. The photodetector may eventually lose its ability to respond linearly or proportionately to the increase in light power density. In the 4H-SiC substrate case, values of responsivity and IQE are better compared to the case of the β-Ga$_2$O$_3$:Sn substrate.

Figure 4.20 (a) and (b) show, the IQE and responsivity of the SB UV-PhD at different reverse biases on a 4H-SiC substrate. Values of IQE and responsivity increase with the increase of reverse bias. The study is limited to small biases since the device is a vertical Schottky diode intended to be self-powered. The increase in IQE and responsivity with increasing reverse bias is obvious and is generally attributed to the expansion of the depletion region, also the gain effect under a high electrical field [136].

Figure 4.20 (c) displays, the T-D PhR under 255 nm wavelength for SB UV-PhD using the 4H-SiC substrate at various reverse biases. We observe a rapid rise and rapid decay and as the reverse bias increases the rise and decay times become very short. This is accompanied by a rise in the photocurrent density which reaches $\approx 50\ \mu A/cm^2$ at -5 V.
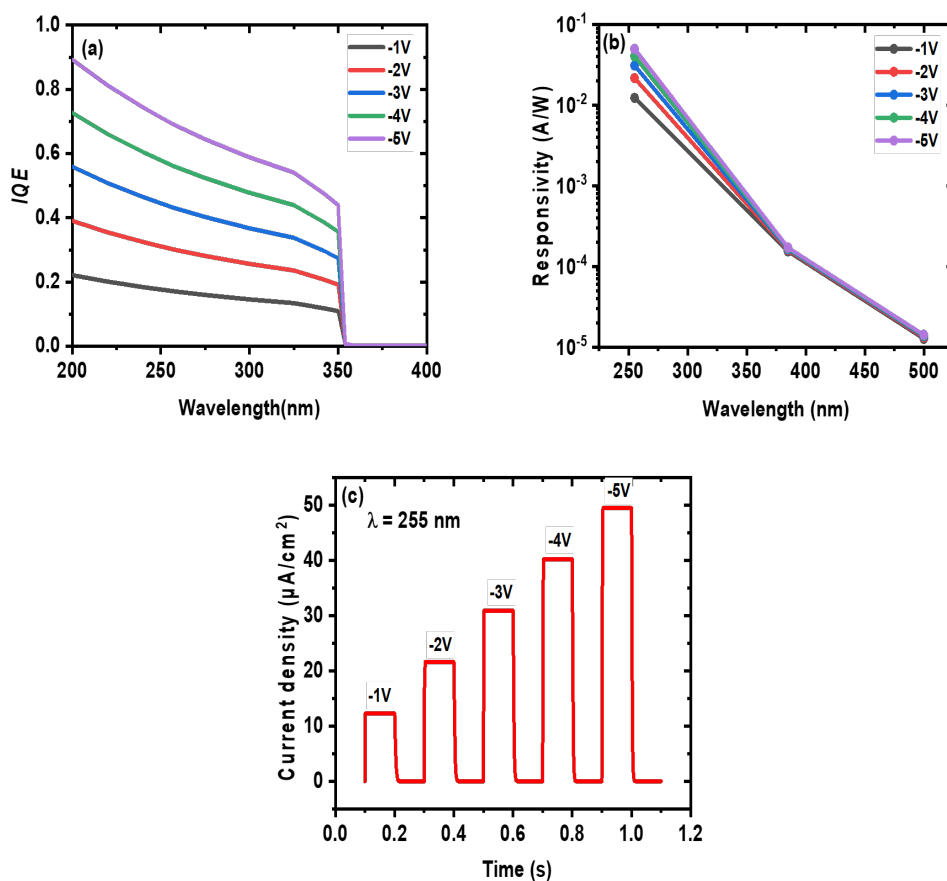
Figure 4.20: **(a)** IQE and **(b)** Responsivity versus wavelength at different reverse biases for the SB UV-PhD with 4H-SiC substrate. **(c)** The T-D PhR under 255 nm at different reverse biases for the SB UV-PhD with 4H-SiC substrate.

4.4.3.1 Effect of traps in 4H-SiC substrate

Previously, it was remarked that the J-V characteristic exhibits asymmetry when the trap density is below $5.0 \times 10^{17} cm^{-3}$. This section presents the effect of slightly increasing the traps density over $5.0 \times 10^{17} cm^{-3}$. Additionally, whether a slight variation in their positions can

influence the device's performance.

Figure 4.21 (a), (b), (c), and (d) illustrate the obtained results on J-V characteristic and T-D PhR. A slight increase in traps density leads to a significant decrease in photocurrent at 255 nm due to increased charge recombination, as seen in Figure 4.21 (a) and (b). The decay time is also affected by the minor rise in traps density. At a trap density of $5.5 \times 10^{17} cm^{-3}$, the decay time increases, attributed to the increased PPC phenomenon. Where it is about $0.056s$ for trap $E_T = 0.80 \ eV$ and $0.064s$ for trap $E_T = 1.01 \ eV$ at 255 nm and -1 V, as seen in Figure 4.21 (c) and (d).

Several methods have been suggested to decrease the traps density in the 4H-SiC film, such as annealing at different temperatures to improve the crystalline structure of the film. Enhanced crystallinity can reduce traps density, mitigate charge recombination, and ultimately improve the device's performance [238].
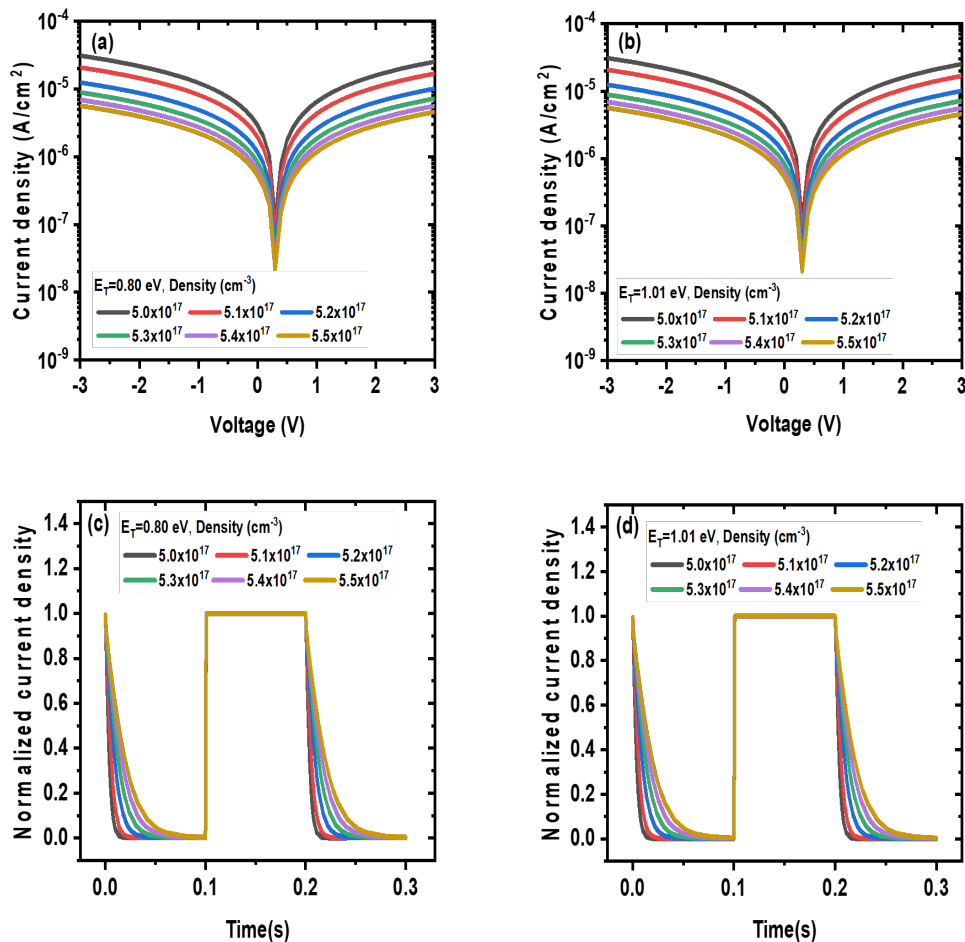
Figure 4.21: Effect of traps density on the J-V characteristic: **(a)** $E_T = 0.80 \ eV$, **(b)** $E_T = 1.01$ eV; and on T-D PhR: **(c)** $E_T = 0.80 \ eV$ and **(d)** $E_T = 1.01 \ eV$ for 4H-SiC substrate.

As shown in Figure 4.22 (a), and (b), shifting the E_T position from 0.80 to 0.90 eV results in a significant decrease in the photocurrent density but changing the E_T from 1.01 to 1.51

eV has no impact at 255 nm. The same observation applies to the T-D PhR, the decay time increases from 0.056 to 0.094 s for E_T ranging from 0.80 to 0.90 eV. It stays constant at 0.064 s for E_T ranging from 1.01 to 1.51 eV at 255 nm and -1 V, as seen in Figure 4.22 (c) and (d). The change in E_T depth from 1.01 to 1.51 eV does not influence due to its location deeper than the Fermi level of the n-type semiconductor material. The equilibrium Fermi level in the 4H-SiC region is around 0.31 eV. Consequently, a trap that has a deep level relative to the Fermi level will be inactive, also E_T= 1.01 eV has a lower σ_n than E_T= 0.80 eV.
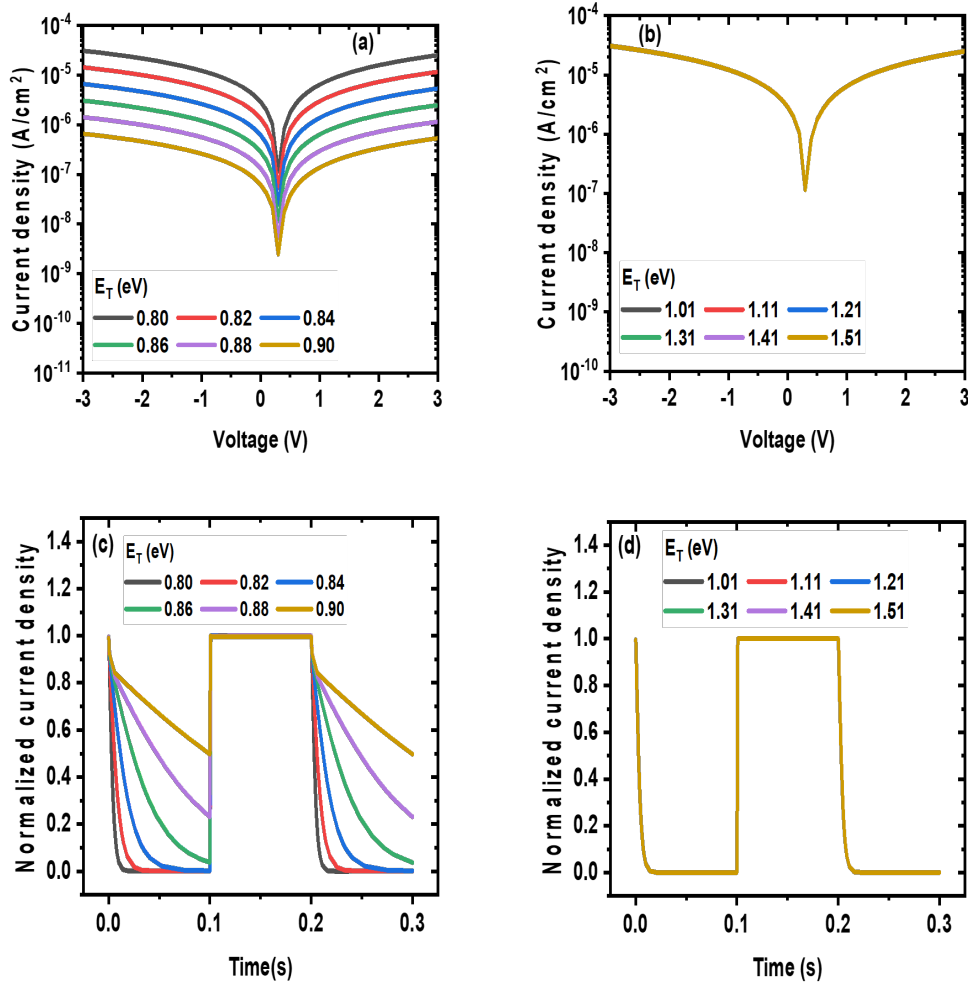
Figure 4.22: Effect of the slight variation of traps position on the J-V characteristic: **(a)** E_T = 0.80 eV, **(b)** E_T = 1.01 eV; and on T-D PhR: **(c)** E_T = 0.80 eV and **(d)** E_T = 1.01 eV for 4H-SiC substrate.

4.4.4 Effect of incorporating a buffer layer between β-Ga$_2$O$_3$:Si drift layer and 4H-SiC substrate

The performance of SB UV-PhD is significantly dependent on the band alignment and interface characteristics. Research indicates that adding a buffer layer to the substrate can greatly enhance the quality of β-Ga$_2$O$_3$ films [174–177]. The composition of the buffer layer changes

depending on its specific purpose. We suggest incorporating a customized 4H-SiC intrinsic thin buffer layer between the β-Ga$_2$O$_3$:Si drift layer and the 4H-SiC substrate. This buffer layer has distinct properties including χ, E_g, and thickness to enhance device performance further. The 4H-SiC substrate was maintained at a doping concentration and thickness of $1.0\times10^{18} cm^{-3}$ and $650\,\mu m$, respectively. The parameter set of the 4H-SiC intrinsic thin buffer layer is summarized in Table 4.3.

Table 4.3: The characteristics of the 4H-SiC intrinsic thin buffer layer [217].

Parameters	4H-SiC intrinsic thin buffer layer
E_g (eV)	3.26-4.0
χ (eV)	3.0-3.8
μ_n $(cm^2/V.s)$	900
μ_p $(cm^2/V.s)$	115
N_C (cm^{-3})	1.7×10^{19}
N_V (cm^{-3})	2.5×10^{19}
ε	9.7
Thickness (μm)	10^{-3}

Figure 4.23 illustrates, the impact of the buffer layer. The J-V characteristic Figure 4.23 (a) shows a significant fourfold increase in photocurrent when adding a buffer layer. However, improvement in dark conditions is observed exclusively at forward biases.

Figure 4.23 (b) displays, the band energy diagram of β-Ga$_2$O$_3$:Si/buffer layer/4H-SiC. Before adding the buffer layer there were offset discontinuities at the β-Ga$_2$O$_3$:Si/4H-SiC interface with $\Delta E_C = 0.55\ eV$ and $\Delta E_V = 2.1\ eV$. The inclusion of the buffer layer resulted in reduced offset discontinuities; ΔE_C decreased to $0.31\ eV$ at the buffer layer/4H-SiC interface and to $0.42\ eV$ at the β-Ga$_2$O$_3$:Si/buffer layer interface. At the buffer layer/4H-SiC interface, ΔE_V decreases to $1.15\ eV$ and at the β-Ga$_2$O$_3$:Si/buffer layer to $1.16\ eV$. These adjustments account for the noticeable enhancement in photocurrent for both reverse and forward biases, attributed to improved ability for free charge carriers' transfer.

Figure 4.24 (a) and (b) show, IQE, and responsivity at -1 V. Over the 255 to 350 nm range comparing cases with and without a buffer layer, the device shows a significant increase in IQE achieving 0.36 at 255 nm with a buffer layer in contrast to 0.17 without a buffer layer. The improved responsivity is 0.026 A/W, higher than the 0.012 A/W achieved without a buffer layer. The rejection ratio increased to 2×10^3 and the detectivity reached 1×10^{12} $Jones$ using a buffer layer under 255 nm at -1 V.

Figure 4.25 shows the T-D PhR at -1 V under 255 nm wavelength. The enhancement in the final case with a buffer layer is apparent. We observed a decrease in decay time and a notable enhancement in photocurrent density reaching 28 $\mu A/cm^2$ at $t = 0\ s$.
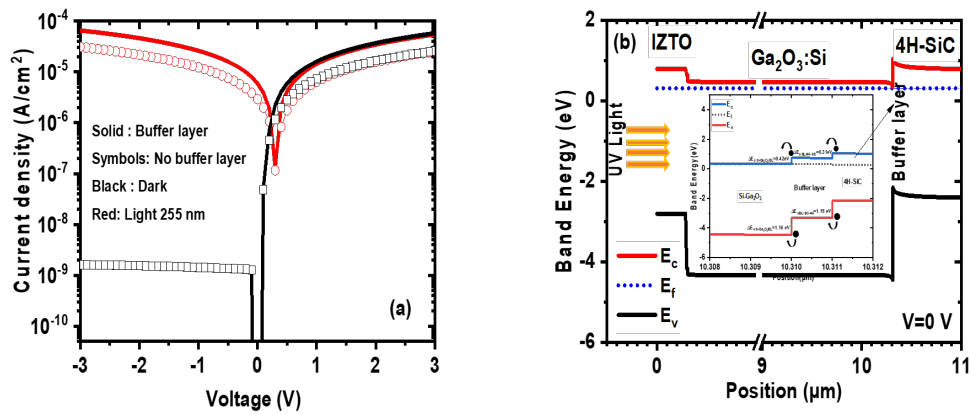
Figure 4.23: **(a)** Simulated J-V characteristic with and without buffer layer under 255 *nm* wavelength and at the dark for the SB UV-PhD. **(b)** The band energy diagram at V= 0*V*.
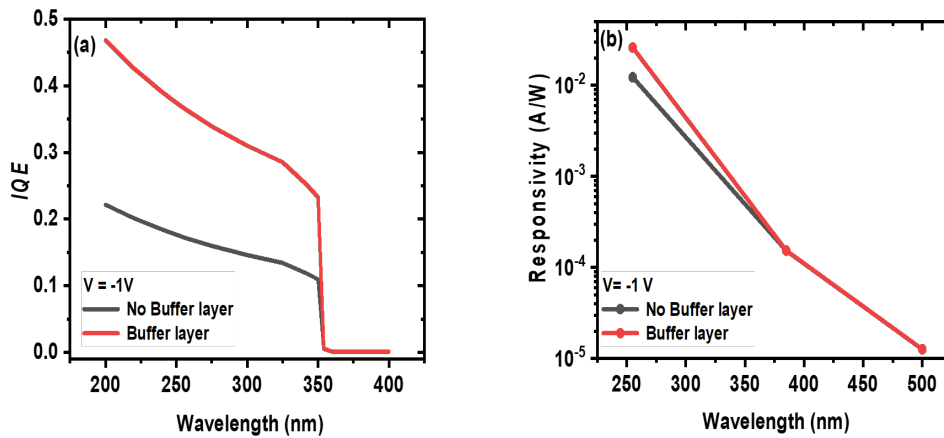
Figure 4.24: **(a)** IQE and **(b)** Responsivity versus wavelength at -1 *V* with and without buffer layer for the SB UV-PhD.

Figure 4.26 (a), (b), and (c) display the photocurrent, responsivity, and IQE variations versus light power density at - 1 *V* under 255 *nm* wavelength, with and without the buffer layer. Inside the light power density range of 10^{-10} to 10^{-4} W/cm^2, the buffer layer does not affect the electrical performance of the device. However, when the light power density surpasses $10^{-4}W/cm^2$, the beneficial impact of the buffer layer becomes evident. When light power density increases, the photodetector encounters a threshold where it can no longer respond proportionally to the increasing light power density, entering a saturation regime. The saturation phenomenon unfolds slower in the device featuring a buffer layer. This suggests that the carrier recombination rate is higher, contributing to the delayed onset of saturation as much has been explained in section 4.4.1.3.
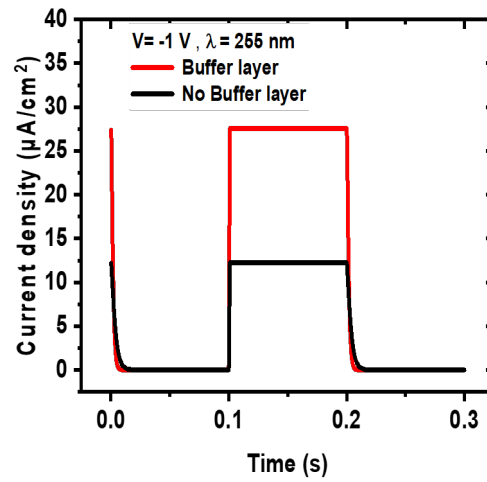
Figure 4.25: Comparison of the T-D PhR under illumination 255 *nm* at - 1 *V* between SB UV-PhD with and without buffer layer.
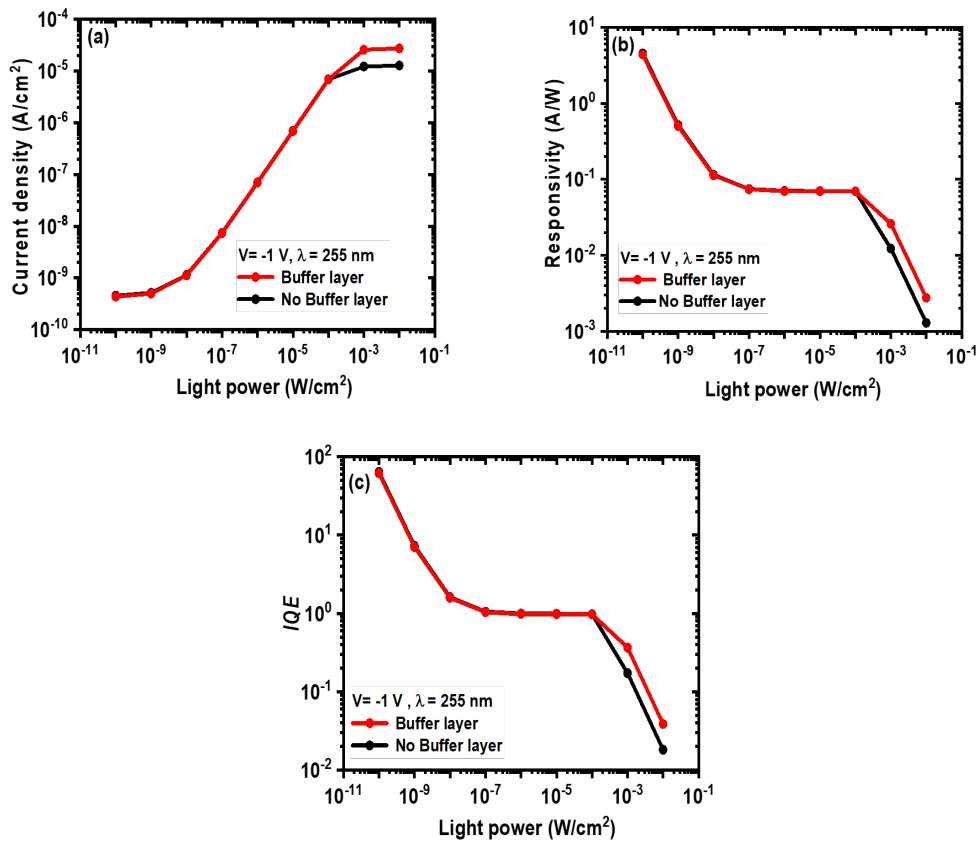
Figure 4.26: Comparison between SB UV-PhD with and without buffer layer of the dependence on the light power density of **(a)** photocurrent, **(b)** responsivity, and **(c)** IQE; at -1 *V* and 255 *nm* wavelength.

Results and discussion

4.4.4.1 Effect of electronic affinity of the buffer layer

Electronic affinity plays a crucial function in aligning E_g when examining the contact of various semiconductor materials to comprehend the behavior of charge carriers (electrons and holes) at the interface. Experimentally the electronic affinity is related to the chemical composition of the surface, surface polarization, and external factors such as Ar bombardment, plasma, etc [239–241].
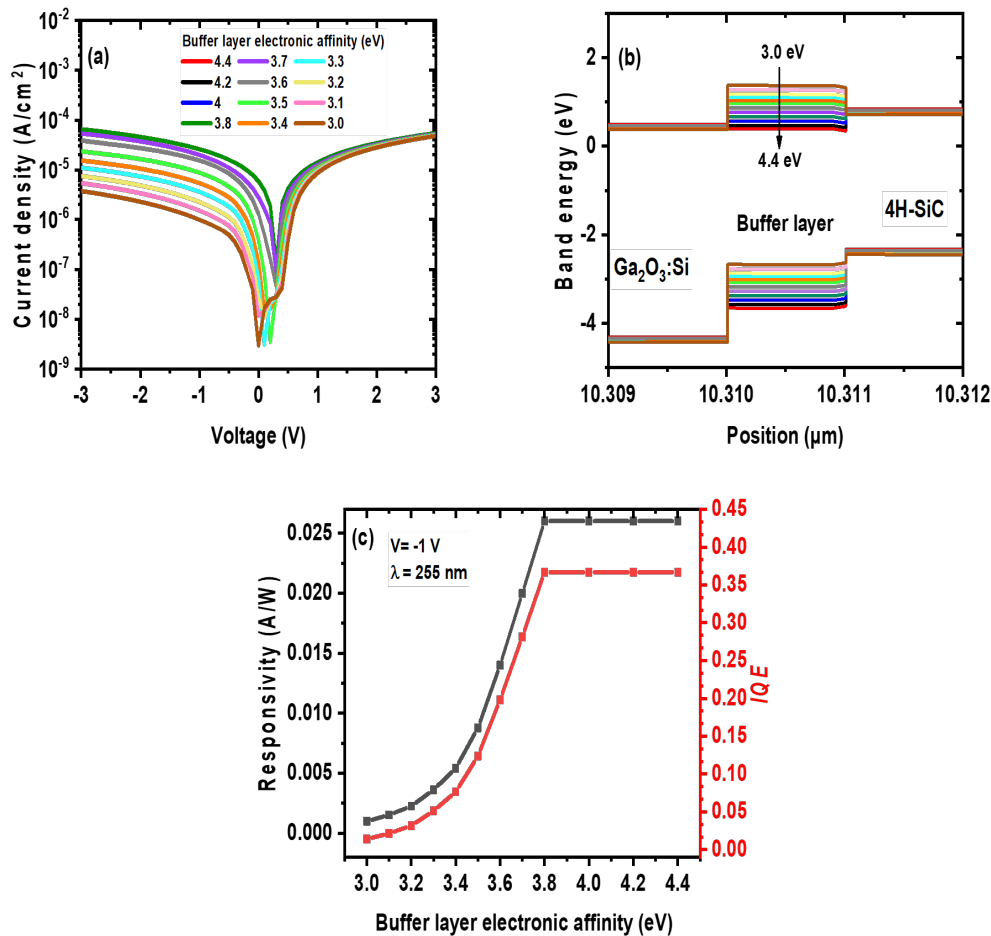
Figure 4.27: **(a)** The influence of the electronic affinity of the buffer layer on J-V characteristic under 255 *nm* wavelength for the SB UV-PhD. **(b)** Equilibrium band diagram for different buffer layer electronic affinity. **(c)** The buffer layer electronic affinity effect on responsivity and IQE; at -1 *V* and 255 *nm* wavelength.

Figure 4.27 (a) illustrates, how the electronic affinity of the 4H-SiC intrinsic thin buffer layer affects the J-V characteristic. The current density drops as the electronic affinity of the 4H-SiC intrinsic thin buffer layer decreases from 3.8 to 3.0 *eV* in reverse bias, at the same time a minor effect is noticed in forward bias. However, the impact of the electronic affinity on the J-V characteristic is insignificant when it exceeds 3.8 *eV*.

In addition, Figure 4.27 (b) illustrates that a reduction in the buffer layer's electronic affin-

ity leads to a gradual rise in the potential barrier within the buffer layer. This barrier blocks the movement of free electrons from the β-Ga_2O_3:Si drift layer to the 4H-SiC substrate.

Figure 4.27 (c) illustrates, that a decrease in the electronic affinity of the 4H-SiC intrinsic thin buffer layer leads to a simultaneous reduction in both responsivity and IQE. Decreasing the electronic affinity of the buffer layer results in forming a potential barrier within the buffer layer. This potential barrier hinders the electron flow, functioning as resistance and reducing the device's performance [144, 239], as illustrated in Figure 4.27 (b).

4.4.5 Effect of substituting IZTO with Graphene

Graphene has exceptional properties that qualify it as a suitable alternative to traditional transparent electrodes. Their outstanding electrical conductivity and exceptional carrier mobility (9000 $cm^2/V.s$ at RT), mechanical strength, and excellent optical transparency across a broad wavelength spectrum, from DUV to NIR [181–184]. In addition to its remarkably high charge mobility, electronic conductivity, and optical transmission [242, 243].

It has a low electrical resistivity of 0.2×$10^{-6} k\Omega.cm$ [218]. Compared with metallic materials, Graphene is a new novel heat-spreading material that possesses a superior thermal conductivity of up to 5300 W/mK at RT [244]. In addition to its high flexibility, it can be bent and twisted without breaking [245]. The unique structure of Graphene imparts exceptional strength and impermeability to gases and liquids, even helium, the tiniest atom [246].

For these reasons, the IZTO material will be replaced in the Schottky contact by Graphene. The fact that Graphene does not have an E_g and is transparent means that its introduction in the simulation of the device is quite different from that of IZTO, it will be introduced into the simulation as a top surface Schottky contact with high UV-visible transparency and good electrical conductivity. Additionally in this section, the intrinsic thin 4H-SiC buffer layer is preserved on the 4H-SiC substrate. Table 4.1 shows Schottky's contact parameters.

Figure 4.28 illustrates, the J-V characteristic under reverse and forward biases (-3, 3)V for both cases of Graphene and IZTO as Schottky contacts, in the dark and under 255 nm wavelength. When Graphene contact is used instead of IZTO contact, enhancements are observed in both dark and light conditions. In the dark case the forward current increases significantly, while the reverse current decreases causing a substantial rise in the PDCR to around 10^5.

The use of Graphene has greatly enhanced the sensitivity of light detection, as seen in Figure 4.29 (a) and (b). Both IQE and responsivity have notably increased achieving values of 0.57 and 0.074 A/W, respectively. Additionally, there is a substantial enhancement in the rejection ratio and detectivity reaching 6×10^3 and 5×10^{12} *Jones* at -1 V and 255 nm

wavelength, respectively. These findings underscore the positive impact of Graphene on the overall performance of the device.
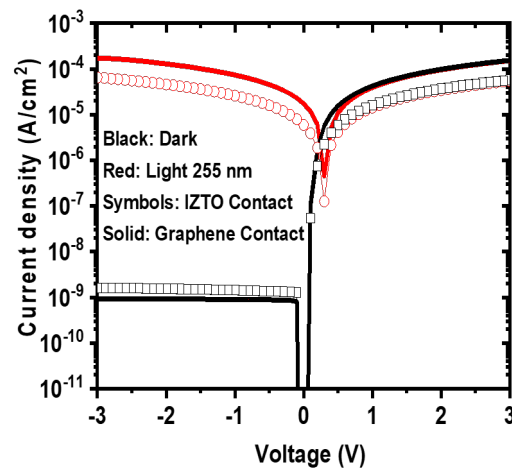
Figure 4.28: Simulated J-V characteristic of SB UV-PhD; comparison between the use of IZTO and Graphene as Schottky contacts in the dark and under 255 nm wavelength.
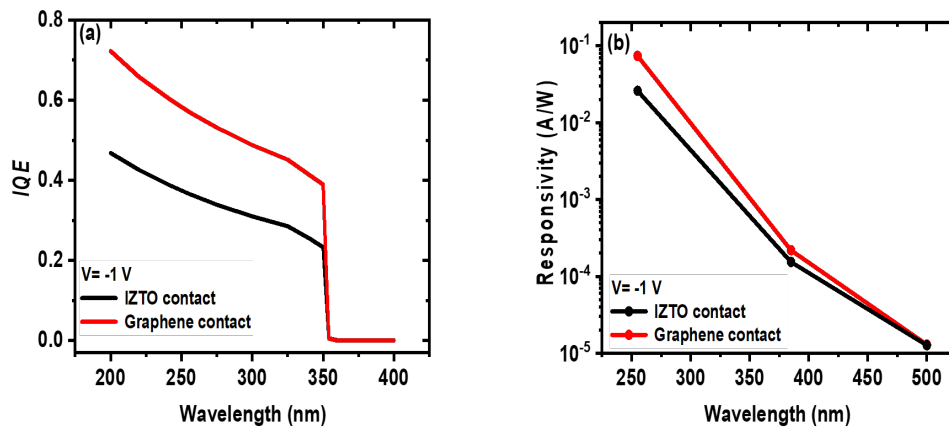
Figure 4.29: **(a)** IQE and **(b)** Responsivity versus wavelength at -1 V with Graphene and IZTO Schottky contacts.

Figure 4.30 shows the T-D PhR using Graphene and IZTO Schottky contacts at -1 V and 255 nm wavelength. The photocurrent density by using the Graphene Schottky contact reached remarkably 52 $\mu A/cm^2$ at t=0 s surpassing that of the IZTO Schottky contact. This increase did not impact the rise and decay times, which are nearly identical to those of the IZTO Schottky contact.

Figure 4.31 (a), (b), and (c), display photocurrent, responsivity, and IQE versus light power density, a comparison between IZTO and Graphene at -1 V and 255 nm wavelength. Both SB UV-PhD with IZTO and Graphene Schottky contacts exhibit the same onset detection

threshold of $10^{-9} W/cm^2$. Additionally, it is noted that all optical outputs (photocurrent, responsivity, and IQE) exhibit superior performance using Graphene Schottky contact.
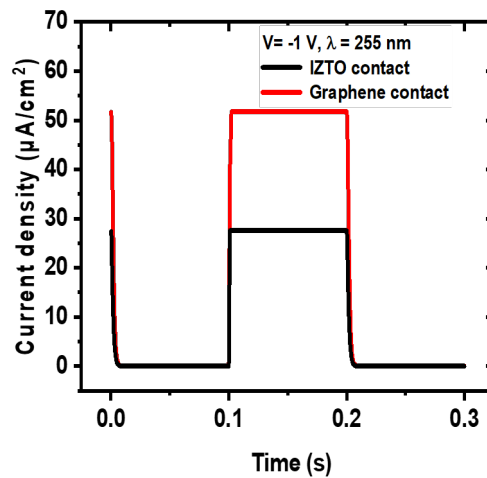
Figure 4.30: Comparison of the T-D PhR under illumination 255 nm at -1 V between SB UV-PhD with Graphene and IZTO Schottky contacts.
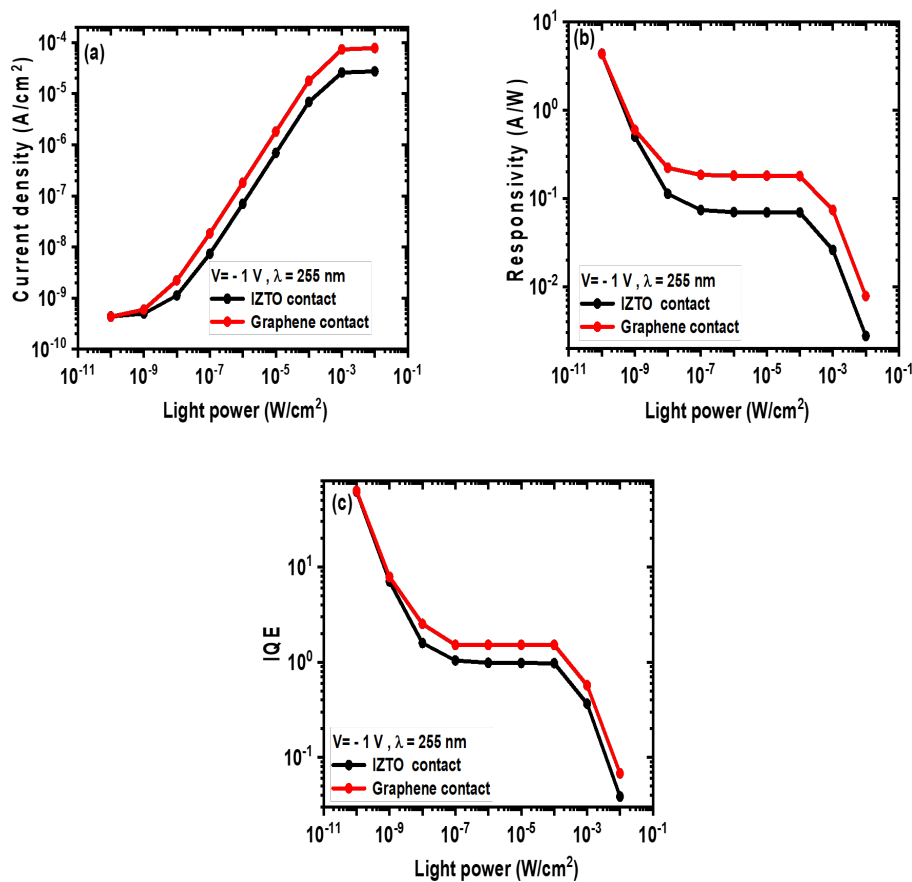
Figure 4.31: Comparison between SB UV-PhD with IZTO and Graphene Schottky contacts of the dependence on the light power density of **(a)** photocurrent, **(b)** responsivity, and **(c)** IQE; at -1 V and 255 nm wavelength.

4.4.5.1 Effect of Graphene workfunction

According to E.V. Rut'kov et al. the workfunction of Graphene increases from $4.30 \pm 0.05 \ eV$ for a monolayer and from $4.70 \pm 0.05 \ eV$ for thicknesses ≥ 10 layers. The workfunction of surface contact is particularly sensitive to free electron density and the interface with the subsequent bulk layer. A heavily doped Graphene will have a smaller work function compared to the undoped case [247]. This section focuses on forecasting how doping affects the device's performance by changing the workfunction of Graphene within the range of 4.8 to $4.0 \ eV$.
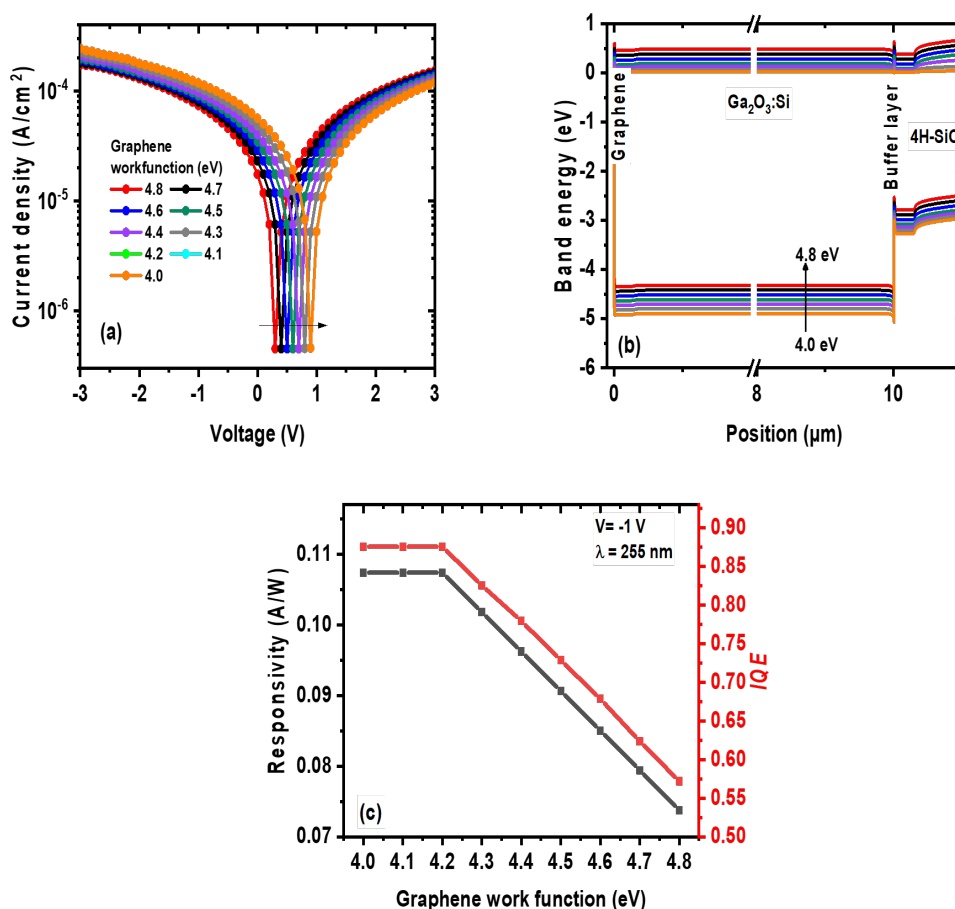
Figure 4.32: **(a)** The influence of the Graphene workfunction on J-V characteristic under 255 nm wavelength for the SB UV-PhD. **(b)** Equilibrium band diagram variation with the Graphene workfunction. **(c)** Graphene workfunction effect on responsivity and IQE; at -1 V and 255 nm wavelength.

Figure 4.32 (a) displays, the impact of the Graphene workfunction on the J-V characteristic under 255 nm wavelength, whereas Figure 4.32 (b) shows the band energy diagram at equilibrium. We observe an overlie in the J-V curves and band energy diagrams for workfunction values of 4.2, 4.1, and 4.0 eV. The noticeable change is the rise in photocurrent in both reverse and forward biases, together with a shift of the entire J-V characteristic to-

wards positive biases. This implies that the photodetector becomes a self-powered solar-blind photodetector [144]. The sensitivity to UV light has improved because of the increased generation of photocurrent. This can be explained by the decrease in ϕ_B which is the barrier formed between the Graphene and β-Ga$_2$O$_3$:Si drift layer, as seen in Figure 4.32 (b). This phenomenon follows the Schottky-Mott rule [180].

$$\phi_B = \phi_{Graph} - \chi_{\beta-\text{Ga}_2\text{O}_3:\text{Si}} \qquad (4.1)$$

ϕ_{Graph} is the Graphene workfunction and $\chi_{\beta-\text{Ga}_2\text{O}_3:\text{Si}}$ the affinity of β-Ga$_2$O$_3$:Si drift layer. Figure 4.32 (c) supports this result by illustrating the increase in responsivity and IQE.

4.4.6 Effect of high operating temperature

In this section, the objective is to assess whether the photodetector offers advantages by enhancing its resistance to the effects of high operating temperature. We will analyze the J-V characteristic at reverse and forward biases to assess the influence of high operating temperature on three different SB UV-PhD configurations.

The initial configuration employs a β-Ga$_2$O$_3$:Sn substrate, the second configuration contains a 4H-SiC substrate with a buffer layer, and the third configuration utilizes a Graphene Schottky contact with a temperature range of 25 to 225 °C. Common heat sources in experiments often involve the environment, particularly warm or high-temperature areas. Additionally, excess energy beyond the E_g of the semiconductor, such as solar spectrum energy or the temperature of a light source, can be used. Other external sources may include high-temperature storage and annealing at elevated temperatures. The J-V characteristic for various configurations is shown in Figure 4.33.

The photocurrent exhibits a positive correlation with high operating temperature, indicating that as operating temperature increases, the photocurrent also increases. Among the three configurations, the one with β-Ga$_2$O$_3$:Sn substrate is the most sensitive to high operating temperature, exhibiting a larger variation between two different temperatures compared to the other two configurations. In these two configurations, the rate of increase in the photocurrent slows down. Furthermore, the J-V characteristic exhibits an asymmetrical behavior with increasing operating temperature. As it increases, the UV absorption coefficient also increases. Therefore, the observed increase in absorption in the photodetector indicates an increased generation of photogenerated carriers, which can effectively transfer to the electrode contacts and generate a photocurrent [248].
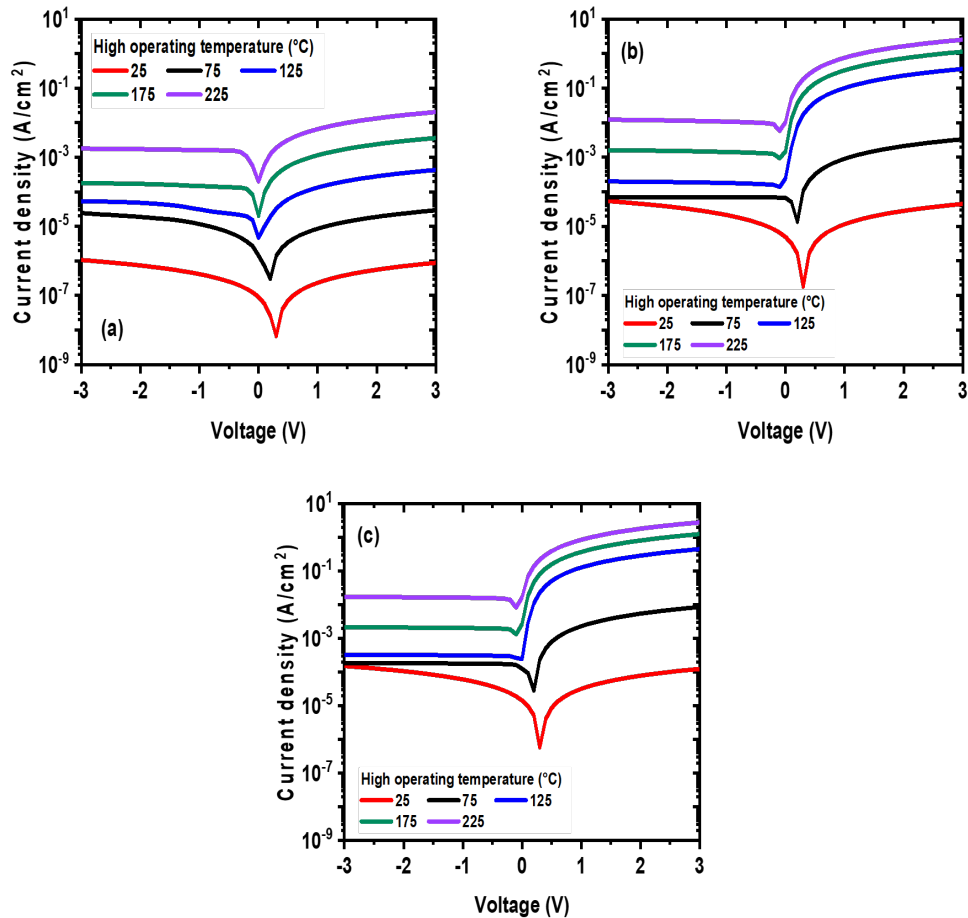
Figure 4.33: High operating temperature effect on J-V characteristic under 255 nm wavelength for the SB UV-PhD **(a)** with β-Ga$_2$O$_3$:Sn substrate, **(b)** with 4H-SiC substrate and the buffer layer, **(c)** with Graphene Schottky contact.

To achieve enduring reliability in high operating temperatures. Y. Xu et al exposed a 4H-SiC photodetector, equipped with metallic Schottky contacts, to a temperature of 200 °C in an ambient air environment for 100 $hours$. Following thermal storage, there was an increase in both the photocurrent and the responsivity. This has confirmed the reliable functioning of the 4H-SiC UV detectors at temperatures up to 200 °C but at temperatures beyond 300 °C, the general performance of the photodetector begins to deteriorate. However, the photodetector can maintain its functionality at a satisfactory level even after undergoing brief thermal treatment at temperatures reaching up to 550 °C [249].

According to our results, we deduce that Graphene/β-Ga$_2$O$_3$:Si /buffer layer/4H-SiC/ITO SB UV-PhD is expected to operate reliably at temperatures above 225 °C. This process is a significant improvement in the device's performance over any of the previous photodetectors [250–252].

4.5 Conclusion

In this chapter, the β-Ga$_2$O$_3$ SB UV-PhD was simulated and compared to experimental performance under reverse biases. The following improvements were then proposed. The first part of the optimizations involved reducing the traps density for the β-Ga$_2$O$_3$:Sn substrate and adding a passivation layer (Al$_{0.39}$Ga$_{0.61}$)$_2$O$_3$ between the IZTO photo-anode and the β-Ga$_2$O$_3$:Si drift layer. Where the focus was on the effect of reducing the traps density of $E_c - 0.55eV$, $E_c - 0.74eV$, and $E_c - 1.04eV$, we found that decreasing traps density led to an increase in photocurrent in both reverse and forward biases. The responsivity achieved a value of 0.04 A/W with low β-Ga$_2$O$_3$ traps density. The projected decay time for the lowest density of traps is approximately 0.05s for $E_c - 0.74eV$ and $E_c - 1.04eV$ and is shorter at around 0.015s for $E_c - 0.55eV$ where shallow traps produced the most significant impact on the PPC phenomenon. Moreover, when traps density is low, this photodetector can be considered a self-powered solar-blind photodetector. In addition, with the insertion of the passivation layer (Al$_{0.39}$Ga$_{0.61}$)$_2$O$_3$ the photocurrent is enhanced.

The second part of additional optimizations focused on enhancing the β-Ga$_2$O$_3$ SB UV-PhD through three successive steps. Firstly, utilize 4H-SiC as a substrate. Secondly, add a 4H-SiC intrinsic thin buffer layer between the β-Ga$_2$O$_3$:Si drift layer and 4H-SiC substrate. Thirdly, use Graphene as a Schottky contact. Substituting the substrate material from β-Ga$_2$O$_3$:Sn to 4H-SiC results in substantial enhancements in all output parameters: photocurrent of 1.23×10^{-5}A/cm^2, a responsivity of 0.012 A/W, an IQE of 0.17, and a detectivity of 5×10^{11}$Jones$; at -1V under 255 nm wavelength.

Lead placing an intrinsic buffer layer between the β-Ga$_2$O$_3$:Si drift layer and the 4H-SiC substrate enhancing the device quality, the best parameters obtained: photocurrent of 2.60×-10^{-5}A/cm^2, responsivity of 0.026 A/W, IQE of 0.36, and detectivity of 1×10^{12}$Jones$; at -1 V under 255 nm wavelength. By using Graphene as a Schottky contact, the optimal output parameters achieved for the photodetector were as follows: photocurrent of 7.38×10^{-5}A/cm^2, responsivity of 0.074 A/W, IQE of 0.57, and detectivity of 5×10^{12}$Jones$; at -1V under 255 nm wavelength. The effect of a slight increase in the traps density and its positions in the 4H-SiC substrate was also studied as a small increase in the traps density leads to a significant decrease in the photocurrent density. As for the slight shift in the traps positions, we note that there is a big difference between the effect of $E_c - 0.80eV$ and $E_c - 1.01eV$. Additionally, we examined the impact of the electronic affinity of the buffer layer where the photocurrent density decreases as it decreases, in reverse bias due to the high ϕ_B. An investigation has also been conducted on the effect of Graphene workfunction, showing an increase in photocurrent at the reverse and forward biases with shifting the entire J-V characteristic toward positive biases. Thus, the photodetector becomes a self-powered solar-blind photodetector and its sensitivity to UV radiation is enhanced.

Results and discussion

Finally, The SB UV-PhD was assessed to determine if it offers advantages by enhancing its ability to withstand high operating temperatures. It was noted that the photocurrent rises as the operating temperature increases. We may conclude that the Graphene/β-Ga$_2$O$_3$:Si/buffer layer/4H-SiC/ITO SB UV-PhD is anticipated to operate reliably at temperatures over 225 °C.
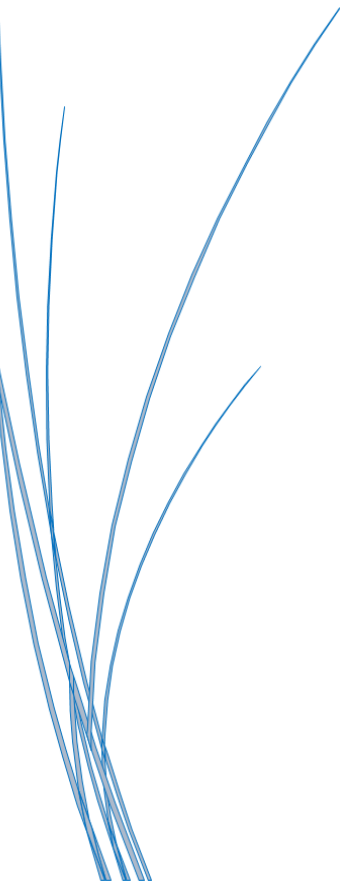
Conclusion

Conclusion

Semiconductors are technological materials that possess properties between good conductors and good insulators, making them crucial for modern electronics and technology. The importance of semiconductors lies in their ability to effectively control the flow of electric current, enabling the design of complex electronic circuits and devices such as processors and semiconductor components.

The characteristics of semiconductors depend on their ability to conduct electricity when exposed to external stimuli such as temperature, light, or electrical current itself. Examples of semiconductors include Si and Ge, which are widely used in the semiconductor industry.

Semiconductor technology has advanced significantly in recent decades, leading to remarkable progress in digital electronics and modern technology overall. Ongoing research in this field aims to develop new materials and techniques that enhance the performance of semiconductors and expand their applications across various technical and industrial fields.

Among the most important materials, we mention Ga_2O_3, with its WBG, high breakdown field, and thermal stability, which is particularly promising for high-power and high-voltage applications. Efforts are focused on improving material quality, refining fabrication processes, and optimizing its properties to enable advancements in power electronics, RF devices, UV photodetectors, and optoelectronics, thereby driving progress in sectors such as aerospace, automotive, and renewable energy.

This research aimed to identify the most important factors that control the performance of IZTO/β-Ga_2O_3 SB UV-PhD. Based on the experimental measurements, to optimize the device performance proficiently and to provide a clear understanding of device performance limits, we developed a comprehensive simulation that gives the correct description of the device operation.

By performing several sets of simulations over the main physical parameters. We have identified the importance of device performance optimization that is through reducing the traps density for β-Ga_2O_3:Sn substrate ($E_c - 0.55eV$, $E_c - 0.74eV$, and $E_c - 1.04eV$), this resulted in a responsivity as high as 0.04 A/W, with a low β-Ga_2O_3 trap density. Where shallow traps produced the most significant impact on the PPC phenomenon. Moreover, with a low

Conclusion

traps density, this photodetector can be considered a self-powered solar-blind photodetector.

The $(Al_{0.39}Ga_{0.61})_2O_3$ film can be utilized in the $(Al_{0.39}Ga_{0.61})_2O_3/Ga_2O_3$ monolithic structure. This configuration enables greater separation between ionized donor impurities, thereby enhancing electron mobility. For this reason, we inserted a passivation layer $(Al_{0.39}Ga_{0.61})_2O_3$ where photocurrent enhancement was observed. An increase in photocurrent is associated with a decrease in recombination and an increase in photogenerated carriers.

The high cost of bulk Ga_2O_3 and its poor thermal conductivity still hinder the commercialization of homoepitaxy. Therefore, it was necessary to search for alternatives, in this study, 4H-SiC was chosen because it shares a similar atomic arrangement with a small mismatch to Ga_2O_3. Significant improvements in all output parameters were achieved. The symmetrical J-V characteristic of the 4H-SiC substrate was attained by incorporating intrinsic defects. Studying the effect of traps density and their positions in the 4H-SiC substrate led to a notable decrease in the photocurrent density, attributed to increased charge recombination. Regarding the slight shift in trap positions, it's notable that there is a significant difference between the effects of $E_c - 0.80 eV$ and $E_c - 1.01 eV$, attributed to the precise location of the traps relative to the Fermi level, considering the n-type characteristics of the semiconductor material.

Recent research has shown that buffer layers are employed to reduce the mismatch between the substrate and the active layer, thereby improving the quality of film crystallization and enhancing device performance. Therefore, it was proposed to incorporate an intrinsic thin buffer layer from the same 4H-SiC substrate material. This buffer layer would be strategically placed between the β-Ga_2O_3:Si drift layer and the 4H-SiC substrate. The J-V characteristic shows a significant four-fold increase in photocurrent when adding a buffer layer. We found that the phenomenon of saturation is detected more slowly in the device equipped with a buffer layer. This indicates that the carrier recombination rate is higher, delaying the onset of saturation. A decrease in the electronic affinity of the buffer layer results in a gradual increase in ϕ_B. Consequently, the photocurrent density decreases in reverse bias.

The choice of Schottky contact material is crucial in determining the performance of UV photodetectors. In recent years, Graphene has garnered significant research attention due to its high UV-visible transparency and good electrical conductivity. For these reasons, we substituted the IZTO material in the Schottky connection with an organic material from Graphene, where improvements were observed in both dark and light conditions. The optimal output parameters are: photocurrent of $7.38 \times 10^{-5} A/cm^2$, responsivity of 0.074 A/W, IQE of 0.57, and detectivity of $5 \times 10^{12} Jones$; at -1V under 255 nm wavelength. The reduction in the work function of Graphene led to an increase in the photocurrent under both reverse and forward biases, shifting the entire J-V characteristic towards positive biases. This can be

Conclusion

attributed to the decrease in the barrier ϕ_B between Graphene and the β-Ga$_2$O$_3$:Si drift layer.

Recently, there has been considerable focus on researching high-temperature UV photodetectors. To assess whether the photodetector provides advantages by improving its resistance to the challenges of high operating temperatures, we varied the operating temperature from 25 to 225 °C. As the operating temperature increases, the UV absorption coefficient also increases, leading to a higher generation of photogenerated carriers and consequently an increase in photocurrent. This process is a significant improvement in the performance photodetector.

It's important to highlight that the performance of UV photodetectors can differ considerably based on the production method and operating conditions. Our advanced numerical simulation of Ga$_2$O$_3$ based UV photodetectors offers a dependable guide, delivering predictive insights crucial for the development of other UV photodetector devices, which are often characterized by low efficiency.

Nevertheless, there remains significant potential for future research to enhance the performance metrics of these innovative energy solutions. One promising avenue for exploration is the theoretical and experimental study of novel photodetector designs. One example of a promising strategy to explore is the surface passivation of the interfaces between the Schottky contact and the β-Ga$_2$O$_3$:Si drift layer using an organic layer. This approach could enhance light absorption and reduce reflectivity, potentially boosting the detector's sensitivity to UV light.

In summary, while our numerical models offer valuable insights into the potential performance of Ga$_2$O$_3$ based photodetectors, further research is essential to explore design and structural modifications. Such efforts are expected to significantly enhance the efficiency, cost-effectiveness, and overall properties of these devices.

Bibliography

[1] J. Lilensten and M. Kretzschmar, "The Solar Spectrum in the UV, EUV, and X Ranges: Observations, Modelling, and Effects on the Earth Upper Atmosphere in the Frame of Space Weather," *Solar and Heliospheric Origins of Space Weather Phenomena*, pp. 53–91, 2006.

[2] X. Chen, F. Ren, S. Gu, and J. Ye, "Review of gallium-oxide-based solar-blind ultraviolet photodetectors," *Photonics Research*, vol. 7, no. 4, pp. 381–415, 2019.

[3] K. Osamura, K. Nakajima, Y. Murakami, P. H. Shingu, and A. Ohtsuki, "Fundamental absorption edge in GaN, InN and their alloys," *Solid State Communications*, vol. 11, no. 5, pp. 617–621, 1972.

[4] J. Ye, S. Gu, S. Zhu, S. Liu, Y. Zheng, R. Zhang, Y. Shi, H. Yu, and Y. Ye, "Gallium doping dependence of single-crystal n-type ZnO grown by metal organic chemical vapor deposition," *Journal of Crystal Growth*, vol. 283, no. 3-4, pp. 279–285, 2005.

[5] C. Persson, C. Platzer-Björkman, J. Malmström, T. Törndahl, and M. Edoff, "Strong Valence-Band Offset Bowing of $ZnO_{1-x}S_x$ Enhances p-Type Nitrogen Doping of ZnO-like Alloys," *Physical Review Letters*, vol. 97, no. 14, p. 146403, 2006.

[6] F. Vigue, E. Tournie, and J.-P. Faurie, "Evaluation of the potential of ZnSe and Zn(Mg)BeSe compounds for ultraviolet photodetection," *IEEE Journal of Quantum Electronics*, vol. 37, no. 9, pp. 1146–1152, 2001.

[7] H. Morkoc, S. Strite, G. Gao, M. Lin, B. Sverdlov, and M. Burns, "Large-band-gap SiC, III-V nitride, and II-VI ZnSe-based semiconductor device technologies," *Journal of Applied Physics*, vol. 76, no. 3, pp. 1363–1398, 1994.

[8] W. Yim, E. Stofko, P. Zanzucchi, J. Pankove, M. Ettenberg, and S. Gilbert, "Epitaxially grown AlN and its optical band gap," *Journal of Applied Physics*, vol. 44, no. 1, pp. 292–296, 1973.

[9] S. Salvatori, M. Rossi, F. Galluzzi, and E. Pace, "Solar-blind UV-photodetector based on polycrystalline diamond films: basic design principle and comparison with exper-

imental results," *Materials Science and Engineering: B*, vol. 46, no. 1-3, pp. 105–111, 1997.

[10] W. Zheng, R. Lin, Z. Zhang, and F. Huang, "Vacuum-ultraviolet photodetection in few-layered h-BN," *ACS Applied Materials & Interfaces*, vol. 10, no. 32, pp. 27 116–27 123, 2018.

[11] T. Onuma, S. Saito, K. Sasaki, T. Masui, T. Yamaguchi, T. Honda, and M. Higashi-waki, "Valence band ordering in β-Ga$_2$O$_3$ studied by polarized transmittance and re-flectance spectroscopy," *Japanese Journal of Applied Physics*, vol. 54, no. 11, p. 112601, 2015.

[12] D. Li, K. Jiang, X. Sun, and C. Guo, "AlGaN photonics: recent advances in materials and ultraviolet devices," *Advances in Optics and Photonics*, vol. 10, no. 1, pp. 43–110, 2018.

[13] M. Kim, J.-H. Seo, U. Singisetti, and Z. Ma, "Recent advances in free-standing single crystalline wide band-gap semiconductors and their applications: GaN, SiC, ZnO, β-Ga$_2$O$_3$, and diamond," *Journal of Materials Chemistry C*, vol. 5, no. 33, pp. 8338–8354, 2017.

[14] Z. G. Shao, M. I. Chen, Dun Jun, H. Lu, R. Zhang, D. P. Cao, W. J. Luo, Y. D. Zheng, L. Li, and Z. H. Li, "High-gain AlGaN solar-blind avalanche photodiodes," *IEEE Electron Device Letters*, vol. 35, no. 3, pp. 372–374, 2014.

[15] J. Yu, C. Shan, J. Liu, X. Zhang, B. Li, and D. Shen, "MgZnO avalanche photodetectors realized in Schottky structures," *physica status solidi (RRL)–Rapid Research Letters*, vol. 7, no. 6, pp. 425–428, 2013.

[16] M. Imura, K. Nakano, N. Fujimoto, N. Okada, K. Balakrishnan, M. Iwaya, S. Kamiyama, H. Amano, I. Akasaki, T. Noro, T. Takagi, and A. Bandoh, "High-temperature metal-organic vapor phase epitaxial growth of AlN on sapphire by multi transition growth mode method varying V/III ratio," *Japanese Journal of Applied Physics*, vol. 45, no. 11R, p. 8639, 2006.

[17] W. Yang, S. Hullavarad, B. Nagaraj, I. Takeuchi, R. Sharma, T. Venkatesan, R. Vispute, and H. Shen, "Compositionally-tuned epitaxial cubic Mg$_x$Zn$_{1-x}$O on Si (100) for deep ultraviolet photodetectors," *Applied Physics Letters*, vol. 82, no. 20, pp. 3424–3426, 2003.

[18] A. Balducci, M. Marinelli, E. Milani, M. Morgada, A. Tucciarone, G. Verona-Rinati, M. Angelone, and M. Pillon, "Extreme ultraviolet single-crystal diamond detectors by chemical vapor deposition," *Applied Physics Letters*, vol. 86, no. 19, 2005.

[19] J. Y. Tsao, S. Chowdhury, M. A. Hollis, D. Jena, N. M. Johnson, K. A. Jones, R. J. Kaplar, S. Rajan, C. G. Van de Walle, E. Bellotti, C. L. Chua, R. Collazo, M. E. Coltrin, J. A. Cooper, K. R. Evans, S. Graham, T. A. Grotjohn, E. R. Heller, M. Higashiwaki, M. S. Islam, P. W. Juodawlkis, M. A. Khan, A. D. Koehler, J. H. Leach, U. K. Mishra, R. J. Nemanich, R. C. N. Pilawa-Podgurski, J. B. Shealy, Z. Sitar, M. J. Tadjer, A. F. Witulski, M. Wraback, and J. A. Simmons, "Ultrawide-bandgap semiconductors: research opportunities and challenges," *Advanced Electronic Materials*, vol. 4, no. 1, p. 1600501, 2018.

[20] A. Kuramata, K. Koshi, S. Watanabe, Y. Yamaoka, T. Masui, and S. Yamakoshi, "High-quality β-Ga_2O_3 single crystals grown by edge-defined film-fed growth," *Japanese Journal of Applied Physics*, vol. 55, no. 12, p. 1202A2, 2016.

[21] K. Sasaki, A. Kuramata, T. Masui, E. G. Villora, K. Shimamura, and S. Yamakoshi, "Device-quality β-Ga_2O_3 epitaxial films fabricated by ozone molecular beam epitaxy," *Applied Physics Express*, vol. 5, no. 3, p. 035502, 2012.

[22] H. Kim, H.-J. Seok, J. H. Park, K.-B. Chung, S. Kyoung, H.-K. Kim, and Y. S. Rim, "Fully transparent InZnSnO/β-Ga_2O_3/InSnO solar-blind photodetectors with high Schottky barrier height and low-defect interfaces," *Journal of Alloys and Compounds*, vol. 890, p. 161931, 2022.

[23] C. A. Hoel, T. O. Mason, J.-F. Gaillard, and K. R. Poeppelmeier, "Transparent conducting oxides in the ZnO-In_2O_3-SnO_2 system," *Chemistry of Materials*, vol. 22, no. 12, pp. 3569–3579, 2010.

[24] L. de Boisbaudran, "On the chemical and spectroscopic characters of a new metal (gallium)," *The London, Edinburgh, and Dublin Philosophical Magazine and Journal of Science*, vol. 50, no. 332, pp. 414–416, 1875.

[25] V. Hill, R. Roy, and E. Osborn, "The system alumina-gallia-water," *Journal of the American Ceramic Society*, vol. 35, no. 6, pp. 135–142, 1952.

[26] R. Roy, V. Hill, and E. Osborn, "Polymorphism of β-Ga_2O_3 and the system Ga_2O_3-H_2O," *Journal of the American Chemical Society*, vol. 74, no. 3, pp. 719–722, 1952.

[27] H. Tippins, "Optical absorption and photoconductivity in the band edge of β-Ga_2O_3," *Physical Review*, vol. 140, no. 1A, p. A316, 1965.

[28] A. Chase, "Growth of β-Ga_2O_3 by the verneuil technique," *Journal of the American Ceramic Society*, vol. 47, no. 9, pp. 470–470, 1964.

[29] H. Aida, K. Nishiguchi, H. Takeda, N. Aota, K. Sunakawa, and Y. Yaguchi, "Growth of β-Ga_2O_3 single crystals by the edge-defined, film-fed growth method," *Japanese Journal of Applied Physics*, vol. 47, no. 11R, p. 8506, 2008.

Bibliography

[30] E. G. Víllora, K. Shimamura, Y. Yoshikawa, K. Aoki, and N. Ichinose, "Large-size β-Ga$_2$O$_3$ single crystals and wafers," *Journal of Crystal Growth*, vol. 270, no. 3-4, pp. 420–426, 2004.

[31] Z. Galazka, R. Uecker, K. Irmscher, M. Albrecht, D. Klimm, M. Pietsch, M. Brützam, R. Bertram, S. Ganschow, and R. Fornari, "Czochralski growth and characterization of β-Ga$_2$O$_3$ single crystals," *Crystal Research and Technology*, vol. 45, no. 12, pp. 1229–1236, 2010.

[32] M. Higashiwaki, K. Sasaki, A. Kuramata, T. Masui, and S. Yamakoshi, "Development of gallium oxide power devices," *physica status solidi (a)*, vol. 211, no. 1, pp. 21–26, 2014.

[33] M. Higashiwaki, K. Konishi, K. Sasaki, K. Goto, K. Nomura, Q. T. Thieu, R. Togashi, H. Murakami, Y. Kumagai, B. Monemar, A. Koukitu, A. Kuramata, and S. Yamakoshi, "Temperature-dependent capacitance–voltage and current–voltage characteristics of Pt/Ga$_2$O$_3$ (001) Schottky barrier diodes fabricated on n—-Ga$_2$O$_3$ drift layers grown by halide vapor phase epitaxy," *Applied Physics Letters*, vol. 108, no. 13, 2016.

[34] B. Zhao, F. Wang, H. Chen, L. Zheng, L. Su, D. Zhao, and X. Fang, "An ultrahigh responsivity (9.7 mA W^{-1}) self-powered solar-blind photodetector based on individual ZnO–Ga$_2$O$_3$ heterostructures," *Advanced Functional Materials*, vol. 27, no. 17, p. 1700264, 2017.

[35] Z. Galazka, "β-Ga$_2$O$_3$ for wide-bandgap electronics and optoelectronics," *Semiconductor Science and Technology*, vol. 33, no. 11, p. 113001, 2018.

[36] S. Pearton, J. Yang, P. H. Cary, F. Ren, J. Kim, M. J. Tadjer, and M. A. Mastro, "A review of Ga$_2$O$_3$ materials, processing, and devices," *Applied Physics Reviews*, vol. 5, no. 1, 2018.

[37] S. Pearton, F. Ren, and M. Mastro, *Gallium Oxide: Technology, Devices and Applications.* Elsevier, 2018.

[38] Z. Muhammad, Z. Anwar, B. Saleem, and J. Shahid, "Emerging cybersecurity and privacy threats to electric vehicles and their impact on human and environmental sustainability," *Energies*, vol. 16, no. 3, p. 1113, 2023.

[39] N. S. Jamwal and A. Kiani, "Gallium oxide nanostructures: A review of synthesis, properties and applications," *Nanomaterials*, vol. 12, no. 12, p. 2061, 2022.

[40] M. Marezio and J. Remeika, "Bond lengths in the α-Ga$_2$O$_3$ structure and the high-pressure phase of Ga$_{2-x}$Fe$_x$O$_3$," *Journal of Chemical Physics*, vol. 46, no. 5, pp. 1862–1865, 1967.

[41] H. Y. Playford, A. C. Hannon, E. R. Barney, and R. I. Walton, "Structures of uncharacterised polymorphs of gallium oxide from total neutron diffraction," *Chemistry–A European Journal*, vol. 19, no. 8, pp. 2803–2813, 2013.

[42] K. Pohl, "Hydrothermale bildung von γ-Ga$_2$O$_3$," *Naturwissenschaften*, vol. 55, pp. 82–82, 1968.

[43] S. Yoshioka, H. Hayashi, A. Kuwabara, F. Oba, K. Matsunaga, and I. Tanaka, "Structures and energetics of Ga$_2$O$_3$ polymorphs," *Journal of Physics: Condensed Matter*, vol. 19, no. 34, p. 346211, 2007.

[44] I. Cora, F. Mezzadri, F. Boschi, M. Bosi, M. Čaplovičová, G. Calestani, I. Dódony, B. Pécz, and R. Fornari, "The real structure of ε-Ga$_2$O$_3$ and its relation to κ-phase," *CrystEngComm*, vol. 19, no. 11, pp. 1509–1516, 2017.

[45] K. Yamaguchi, "First principles study on electronic structure of β-Ga$_2$O$_3$," *Solid State Communications*, vol. 131, no. 12, pp. 739–744, 2004.

[46] H. Peelaers and C. G. Van de Walle, "Brillouin zone and band structure of β-Ga$_2$O$_3$," *Physica Status Solidi (B)*, vol. 252, no. 4, pp. 828–832, 2015.

[47] L. Zhang, J. Yan, Y. Zhang, T. Li, and X. Ding, "First-principles study on electronic structure and optical properties of n-doped p-type β-Ga$_2$O$_3$," *Science China Physics, Mechanics and Astronomy*, vol. 55, pp. 19–24, 2012.

[48] H. He, R. Orlando, M. A. Blanco, R. Pandey, E. Amzallag, I. Baraille, and M. Rérat, "First-principles study of the structural, electronic, and optical properties of Ga$_2$O$_3$ in its monoclinic and hexagonal phases," *Physical Review B—Condensed Matter and Materials Physics*, vol. 74, no. 19, p. 195123, 2006.

[49] N. Ueda, H. Hosono, R. Waseda, and H. Kawazoe, "Synthesis and control of conductivity of ultraviolet transmitting β-Ga$_2$O$_3$ single crystals," *Applied Physics Letters*, vol. 70, no. 26, pp. 3561–3563, 1997.

[50] S. Stepanov, V. Nikolaev, V. Bougrov, and A. Romanov, "Gallium oxide: Properties and applications—a review," *Revue des Avancées en Science et Technologie*, vol. 44, pp. 63–86, 2016.

[51] Z. Galazka, K. Irmscher, R. Uecker, R. Bertram, M. Pietsch, A. Kwasniewski, M. Naumann, T. Schulz, R. Schewski, D. Klimm, and M. Bickermann, "On the bulk β-Ga$_2$O$_3$ single crystals grown by the czochralski method," *Journal of Crystal Growth*, vol. 404, pp. 184–191, 2014.

[52] J. B. Varley, J. R. Weber, A. Janotti, and C. G. Van de Walle, "Oxygen vacancies and donor impurities in β-Ga$_2$O$_3$," *Applied Physics Letters*, vol. 97, no. 14, 2010.

Bibliography

[53] N. Suzuki, S. Ohira, M. Tanaka, T. Sugawara, K. Nakajima, and T. Shishido, "Fabrication and characterization of transparent conductive Sn-doped β-Ga$_2$O$_3$ single crystal," *physica status solidi c*, vol. 4, no. 7, pp. 2310–2313, 2007.

[54] E. G. Víllora, K. Shimamura, Y. Yoshikawa, T. Ujiie, and K. Aoki, "Electrical conductivity and carrier concentration control in β-Ga$_2$O$_3$ by Si doping," *Applied Physics Letters*, vol. 92, no. 20, 2008.

[55] J. Liu, S. Gao, W. Li, J. Dai, Z. Suo, and Z. Suo, "First-Principles Calculations of Electronic Structure and Optical Properties of Si-Doped and Vacancy β-Ga$_2$O$_3$," *Crystal Research and Technology*, vol. 57, no. 1, p. 2100126, 2022.

[56] X. Feng, Z. Li, W. Mi, Y. Luo, and J. Ma, "Mg-doped β-Ga$_2$O$_3$ films with tunable optical band gap prepared on MgO (110) substrates by metal-organic chemical vapor deposition," *Materials Science in Semiconductor Processing*, vol. 34, pp. 52–57, 2015.

[57] L. Liu, M. Li, D. Yu, J. Zhang, H. Zhang, C. Qian, and Z. Yang, "Fabrication and characteristics of N-doped β-Ga$_2$O$_3$ nanowires," *Applied Physics A*, vol. 98, pp. 831–835, 2010.

[58] Z. Wu, Z. Jiang, C. Ma, W. Ruan, Y. Chen, H. Zhang, G. Zhang, Z. Fang, J. Kang, and T.-Y. Zhang, "Energy-driven multi-step structural phase transition mechanism to achieve high-quality p-type nitrogen-doped β-Ga$_2$O$_3$ films," *Materials Today Physics*, vol. 17, p. 100356, 2021.

[59] J. B. Varley, A. Janotti, C. Franchini, and C. G. Van de Walle, "Role of self-trapping in luminescence and p-type conductivity of wide-band-gap oxides," *Physical Review B—Condensed Matter and Materials Physics*, vol. 85, no. 8, p. 081109, 2012.

[60] J. B. Cho, G. Jung, K. Kim, J. Kim, S.-K. Hong, J.-H. Song, and J. I. Jang, "Highly asymmetric optical properties of β-Ga$_2$O$_3$ as probed by linear and nonlinear optical excitation spectroscopy," *The Journal of Physical Chemistry C*, vol. 125, no. 2, pp. 1432–1440, 2020.

[61] A. Paskaleva, D. Spassov, and P. Terziyska, "Electric, dielectric and optical properties of Ga$_2$O$_3$ grown by metal organic chemical vapour deposition," in *Journal of Physics: Conference Series*, vol. 794, no. 1.   IOP Publishing, 2017, p. 012017.

[62] M. Al-Kuhaili, S. Durrani, and E. Khawaja, "Optical properties of gallium oxide films deposited by electron-beam evaporation," *Applied physics letters*, vol. 83, no. 22, pp. 4533–4535, 2003.

[63] N. Ueda, H. Hosono, R. Waseda, and H. Kawazoe, "Anisotropy of electrical and optical properties in β-Ga$_2$O$_3$ single crystals," *Applied physics letters*, vol. 71, no. 7, pp. 933–935, 1997.

[64] Z. Guo, A. Verma, X. Wu, F. Sun, A. Hickman, T. Masui, A. Kuramata, M. Higashiwaki, D. Jena, and T. Luo, "Anisotropic thermal conductivity in single crystal β-gallium oxide," *Applied Physics Letters*, vol. 106, no. 11, 2015.

[65] A. Fiedler, R. Schewski, Z. Galazka, and K. Irmscher, "Static dielectric constant of β-Ga$_2$O$_3$ perpendicular to the principal planes (100),(010), and (001)," *ECS Journal of Solid State Science and Technology*, vol. 8, no. 7, p. Q3083, 2019.

[66] M. D. McCluskey, "Point defects in Ga$_2$O$_3$," *Journal of Applied Physics*, vol. 127, no. 10, 2020.

[67] B. E. Kananen, L. E. Halliburton, K. Stevens, G. Foundos, and N. Giles, "Gallium vacancies in β-Ga$_2$O$_3$ crystals," *Applied Physics Letters*, vol. 110, no. 20, 2017.

[68] K. Irmscher, Z. Galazka, M. Pietsch, R. Uecker, and R. Fornari, "Electrical properties of β-Ga$_2$O$_3$ single crystals grown by the Czochralski method," *Journal of Applied Physics*, vol. 110, no. 6, 2011.

[69] C. A. Lenyk, T. Gustafson, L. E. Halliburton, and N. C. Giles, "Deep donors and acceptors in β-Ga$_2$O$_3$ crystals: Determination of the Fe$^{2+/3+}$ level by a noncontact method," *Journal of Applied Physics*, vol. 126, no. 24, 2019.

[70] K. Takakura, S. Funasaki, I. Tsunoda, H. Ohyama, D. Takeuchi, T. Nakashima, M. Shibuya, K. Murakami, E. Simoen, and C. Claeys, "Investigation of the Si doping effect in β-Ga$_2$O$_3$ films by co-sputtering of gallium oxide and Si," *Physica B: Condensed Matter*, vol. 407, no. 15, pp. 2900–2902, 2012.

[71] R. Sun, Y. K. Ooi, A. Bhattacharyya, M. Saleh, S. Krishnamoorthy, K. G. Lynn, and M. A. Scarpulla, "Defect states and their electric field-enhanced electron thermal emission in heavily Zr-doped β-Ga$_2$O$_3$ crystals," *Applied Physics Letters*, vol. 117, no. 21, 2020.

[72] B. E. Kananen, L. E. Halliburton, E. M. Scherrer, K. Stevens, G. Foundos, K. Chang, and N. C. Giles, "Electron paramagnetic resonance study of neutral Mg acceptors in β-Ga$_2$O$_3$ crystals," *Applied Physics Letters*, vol. 111, no. 7, 2017.

[73] M. H. Wong, C.-H. Lin, A. Kuramata, S. Yamakoshi, H. Murakami, Y. Kumagai, and M. Higashiwaki, "Acceptor doping of β-Ga$_2$O$_3$ by Mg and N ion implantations," *Applied Physics Letters*, vol. 113, no. 10, 2018.

Bibliography

[74] K. Hoshikawa, E. Ohba, T. Kobayashi, J. Yanagisawa, C. Miyagawa, and Y. Nakamura, "Growth of β-Ga$_2$O$_3$ single crystals using vertical bridgman method in ambient air," *Journal of Crystal Growth*, vol. 447, pp. 36–41, 2016.

[75] Z. Chi, J. J. Asher, M. R. Jennings, E. Chikoidze, and A. Pérez-Tomás, "Ga$_2$O$_3$ and related ultra-wide bandgap power semiconductor oxides: new energy electronics solutions for CO$_2$ emission mitigation," *Materials*, vol. 15, no. 3, p. 1164, 2022.

[76] A. K. Saikumar, S. D. Nehate, and K. B. Sundaram, "RF sputtered films of Ga$_2$O$_3$," *ECS journal of solid state science and technology*, vol. 8, no. 7, p. Q3064, 2019.

[77] F. Zhang, K. Saito, T. Tanaka, M. Nishio, and Q. Guo, "Structural and optical properties of Ga$_2$O$_3$ films on sapphire substrates by pulsed laser deposition," *Journal of Crystal Growth*, vol. 387, pp. 96–100, 2014.

[78] D. Pashley, R. Stradling, and P. Klipstein, "Growth and Characterisation of Semiconductors," *Adam Hilger*, pp. 1–16, 1990.

[79] Y. Yao, S. Okur, L. A. Lyle, G. S. Tompa, T. Salagaj, N. Sbrockey, R. F. Davis, and L. M. Porter, "Growth and characterization of α-, β-, and ε-phases of Ga$_2$O$_3$ using MOCVD and HVPE techniques," *Materials Research Letters*, vol. 6, no. 5, pp. 268–275, 2018.

[80] E. G. Víllora, K. Shimamura, K. Kitamura, and K. Aoki, "Rf-plasma-assisted molecular-beam epitaxy of β-Ga$_2$O$_3$," *Applied physics letters*, vol. 88, no. 3, 2006.

[81] J. L. Hudgins, G. S. Simin, E. Santi, and M. A. Khan, "An assessment of wide bandgap semiconductors for power devices," *IEEE Transactions on power electronics*, vol. 18, no. 3, pp. 907–914, 2003.

[82] D. Guo, Q. Guo, Z. Chen, Z. Wu, P. Li, and W. Tang, "Review of Ga$_2$O$_3$-based optoelectronic devices," *Materials Today Physics*, vol. 11, p. 100157, 2019.

[83] A. Trinchi, W. Wlodarski, and Y. X. Li, "Hydrogen sensitive Ga$_2$O$_3$ Schottky diode sensor based on SiC," *Sensors and Actuators B: Chemical*, vol. 100, no. 1-2, pp. 94–98, 2004.

[84] Y. S. Lee, D. Chua, R. E. Brandt, S. C. Siah, J. V. Li, J. P. Mailoa, S. W. Lee, R. G. Gordon, and T. Buonassisi, "Atomic layer deposited gallium oxide buffer layer enables 1.2 V open-circuit voltage in cuprous oxide solar cells," *Adv. Mater*, vol. 26, no. 27, pp. 4704–4710, 2014.

[85] B. Zheng, W. Hua, Y. Yue, and Z. Gao, "Dehydrogenation of propane to propene over different polymorphs of gallium oxide," *Journal of Catalysis*, vol. 232, no. 1, pp. 143–151, 2005.

[86] C. V. Prasad, M. Labed, M. T. A. S. Shaikh, J. Y. Min, T. H. V. Nguyen, W. Song, K. J. Kim, and Y. S. Rim, "Ga_2O_3-based X-ray detector and scintillators: A review," *Materials Today Physics*, vol. 35, p. 101095, 2023.

[87] M. N. Hasan, E. Swinnich, and J.-H. Seo, "Recent progress in gallium oxide and diamond based high power and high-frequency electronics," *International Journal of High Speed Electronics and Systems*, vol. 28, no. 01n02, p. 1940004, 2019.

[88] H. Deng, K. J. Leedle, Y. Miao, D. S. Black, K. E. Urbanek, J. McNeur, M. Kozák, A. Ceballos, P. Hommelhoff, O. Solgaard, R. L. Byer, and J. S. Harris, "Gallium oxide for high-power optical applications," *Advanced Optical Materials*, vol. 8, no. 7, p. 1901522, 2020.

[89] F. Lawrenz, P. Lange, N. Severin, J. P. Rabe, C. A. Helm, and S. Block, "Morphology, mechanical stability, and protective properties of ultrathin gallium oxide coatings," *Langmuir*, vol. 31, no. 21, pp. 5836–5842, 2015.

[90] C. Roy, H. Gies, and S. Toomey, "The solar UV radiation environment: measurement techniques and results," *Journal of Photochemistry and Photobiology B: Biology)*, vol. 31, no. 1-2, pp. 21–27, 1995.

[91] M. Razeghi, "Short-wavelength solar-blind detectors-status, prospects, and markets," *Proceedings of the IEEE*, vol. 90, no. 6, pp. 1006–1014, 2002.

[92] W. Zheng, Z. Zhang, R. Lin, K. Xu, J. He, and F. Huang, "High-Crystalline 2D Layered PbI_2 with Ultrasmooth Surface: Liquid-Phase Synthesis and Application of High-Speed Photon Detection," *Advanced Electronic Materials*, vol. 2, no. 11, 2016.

[93] Q. Hu, W. Zheng, R. Lin, Y. Xu, and F. Huang, "Oxides/graphene heterostructure for deep-ultraviolet photovoltaic photodetector," *Carbon*, vol. 147, pp. 427–433, 2019.

[94] J. Xu, W. Zheng, and F. Huang, "Gallium oxide solar-blind ultraviolet photodetectors: a review," *Journal of Materials Chemistry C*, vol. 7, no. 29, pp. 8753–8770, 2019.

[95] A. Rogalski, Z. Bielecki, J. Mikołajczyk, and J. Wojtas, "Ultraviolet photodetectors: From photocathodes to low-dimensional solids," *Sensors*, vol. 23, no. 9, p. 4452, 2023.

[96] M. Razeghi and A. Rogalski, "Semiconductor ultraviolet detectors," *Journal of Applied Physics*, vol. 79, no. 10, pp. 7433–7473, 1996.

[97] C. Xie and F. Yan, "Flexible photodetectors based on novel functional materials," *Small*, vol. 13, no. 43, p. 1701822, 2017.

[98] G. Peng, Y. Zhou, Y. He, X. Yu, X. A. Zhang, G. Y. Li, and H. Haick, "UV-induced SiC nanowire sensors," *Journal of Physics D: Applied Physics*, vol. 48, no. 5, p. 055102, 2015.

[99] Y. Zou, Y. Zhang, Y. Hu, and H. Gu, "Ultraviolet detectors based on wide bandgap semiconductor nanowire: A review," *Sensors*, vol. 18, no. 7, p. 2072, 2018.

[100] D. Kaur and M. Kumar, "A strategic review on gallium oxide based deep-ultraviolet photodetectors: recent progress and future prospects," *Advanced optical materials*, vol. 9, no. 9, p. 2002160, 2021.

[101] B. Zhao, F. Wang, H. Chen, Y. Wang, M. Jiang, X. Fang, and D. Zhao, "Solar-blind avalanche photodetector based on single ZnO– β-Ga$_2$O$_3$ core–shell microwire," *Nano letters*, vol. 15, no. 6, pp. 3988–3993, 2015.

[102] A. O. Goushcha and B. Tabbert, "On response time of semiconductor photodiodes," *Optical Engineering*, vol. 56, no. 9, pp. 097 101–097 101, 2017.

[103] R. J. Keyes, *Optical and infrared detectors.* Springer Science & Business Media, 2013, vol. 19.

[104] C. Xie, X.-T. Lu, X.-W. Tong, Z.-X. Zhang, F.-X. Liang, L. Liang, L.-B. Luo, and Y.-C. Wu, "Recent progress in solar-blind deep-ultraviolet photodetectors based on inorganic ultrawide bandgap semiconductors," *Advanced Functional Materials*, vol. 29, no. 9, p. 1806006, 2019.

[105] P. Glasow, G. Ziegler, W. Suttrop, G. Pensl, and R. Helbig, "SiC-UV-photodetectors," in *Optoelectronic technologies for remote sensing from space*, vol. 868. SPIE, 1988, pp. 40–47.

[106] M. Liao, Y. Koide, and J. Alvarez, "Thermally stable visible-blind diamond photodiode using tungsten carbide schottky contact," *Applied Physics Letters*, vol. 87, no. 2, 2005.

[107] R. Dahal, J. Li, Z. Fan, M. Nakarmi, T. A. Tahtamouni, J. Lin, and H. Jiang, "AlN MSM and Schottky photodetectors," *physica status solidi c*, vol. 5, no. 6, pp. 2148–2151, 2008.

[108] A. de Luna Bugallo, M. Tchernycheva, G. Jacopin, L. Rigutti, F. H. Julien, S.-T. Chou, Y.-T. Lin, P.-H. Tseng, and L.-W. Tu, "Visible-blind photodetector based on p–i–n junction GaN nanowire ensembles," *Nanotechnology*, vol. 21, no. 31, p. 315201, 2010.

[109] E. Cicek, R. McClintock, C. Cho, B. Rahnema, and M. Razeghi, "Al$_x$Ga$_{1-x}$N-based back-illuminated solar-blind photodetectors with external quantum efficiency of 89%," *Applied Physics Letters*, vol. 103, no. 19, 2013.

[110] W. Zheng, Z. C. Feng, J.-F. Lee, D.-S. Wuu, and R. S. Zheng, "Lattice deformation of wurtzite Mg$_x$Zn$_{1-x}$O alloys: An extended x-ray absorption fine structure study," *Journal of Alloys and Compounds*, vol. 582, pp. 157–160, 2014.

Bibliography

[111] M. Yu, C. Lv, J. Yu, Y. Shen, L. Yuan, J. Hu, S. Zhang, H. Cheng, Y. Zhang, and R. Jia, "High-performance photodetector based on sol–gel epitaxially grown α/β-Ga$_2$O$_3$ thin films," *Materials Today Communications*, vol. 25, p. 101532, 2020.

[112] H. Wang, J. Ma, L. Cong, H. Zhou, P. Li, L. Fei, B. Li, H. Xu, and Y. Liu, "Piezoelectric effect enhanced flexible UV photodetector based on Ga$_2$O$_3$/ZnO heterojunction," *Materials Today Physics*, vol. 20, p. 100464, 2021.

[113] J. Yu, L. Dong, B. Peng, L. Yuan, Y. Huang, L. Zhang, Y. Zhang, and R. Jia, "Self-powered photodetectors based on β-Ga$_2$O$_3$/4H-SiC heterojunction with ultrahigh current on/off ratio and fast response," *Journal of Alloys and Compounds*, vol. 821, p. 153532, 2020.

[114] P. Feng, J. Zhang, Q. Li, and T. Wang, "Individual β-Ga$_2$O$_3$ nanowires as solar-blind photodetectors," *Applied Physics Letters*, vol. 88, no. 15, 2006.

[115] X. Liu, P. Guo, T. Sheng, L. Qian, W. Zhang, and Y. Li, "β-Ga$_2$O$_3$ thin films on sapphire pre-seeded by homo-self-templated buffer layer for solar-blind UV photodetector," *Optical Materials*, vol. 51, pp. 203–207, 2016.

[116] Q. Feng, L. Huang, G. Han, F. Li, X. Li, L. Fang, X. Xing, J. Zhang, W. Mu, Z. Jia, D. Guo, W. Tang, X. Tao, and Y. Hao, "Comparison Study of β-Ga$_2$O$_3$ Photodetectors on Bulk Substrate and Sapphire," *IEEE Transactions on Electron Devices*, vol. 63, no. 9, pp. 3578–3583, 2016.

[117] D. Guo, Y. Su, H. Shi, P. Li, N. Zhao, J. Ye, S. Wang, A. Liu, Z. Chen, C. Li, and W. Tang, "Self-powered ultraviolet photodetector with superhigh photoresponsivity (3.05 A/W) based on the GaN/Sn:Ga$_2$O$_3$ pn junction," *ACS Nano*, vol. 12, no. 12, pp. 12 827–12 835, 2018.

[118] S. Nakagomi, T. Momo, S. Takahashi, and Y. Kokubun, "Deep ultraviolet photodiodes based on β-Ga$_2$O$_3$/SiC heterojunction," *Applied Physics Letters*, vol. 103, no. 7, 2013.

[119] X. Guo, N. Hao, D. Guo, Z. Wu, Y. An, X. Chu, L. Li, P. Li, M. Lei, and W. Tang, "β-Ga$_2$O$_3$/p-Si heterojunction solar-blind ultraviolet photodetector with enhanced photoelectric responsivity," *Journal of Alloys and Compounds*, vol. 660, pp. 136–140, 2016.

[120] Z. Wu, L. Jiao, X. Wang, D. Guo, W. Li, L. Li, F. Huang, and W. Tang, "A self-powered deep-ultraviolet photodetector based on an epitaxial Ga$_2$O$_3$/Ga:ZnO heterojunction," *Journal of Materials Chemistry C*, vol. 5, no. 34, pp. 8688–8693, 2017.

[121] M. Ai, D. Guo, Y. Qu, W. Cui, Z. Wu, P. Li, L. Li, and W. Tang, "Fast-response solar-blind ultraviolet photodetector with a graphene/β-Ga$_2$O$_3$/graphene hybrid structure," *Journal of Alloys and Compounds*, vol. 692, pp. 634–638, 2017.

[122] Y.-C. Chen, Y.-J. Lu, C.-N. Lin, Y.-Z. Tian, C.-J. Gao, L. Dong, and C.-X. Shan, "Self-powered diamond/β-Ga$_2$O$_3$ photodetectors for solar-blind imaging," *Journal of Materials Chemistry C*, vol. 6, no. 21, pp. 5727–5732, 2018.

[123] R. Zhuo, D. Wu, Y. Wang, E. Wu, C. Jia, Z. Shi, T. Xu, Y. Tian, and X. Li, "A self-powered solar-blind photodetector based on a MoS$_2$/β-Ga$_2$O$_3$ heterojunction," *Journal of Materials Chemistry C*, vol. 6, no. 41, pp. 10 982–10 986, 2018.

[124] P. Li, H. Shi, K. Chen, D. Guo, W. Cui, Y. Zhi, S. Wang, Z. Wu, Z. Chen, and W. Tang, "Construction of GaN/Ga$_2$O$_3$ p–n junction for an extremely high responsivity self-powered UV photodetector," *Journal of Materials Chemistry C*, vol. 5, no. 40, pp. 10 562–10 570, 2017.

[125] Y. An, Y. Zhi, Z. Wu, W. Cui, X. Zhao, D. Guo, P. Li, and W. Tang, "Deep ultraviolet photodetectors based on p-Si/i-SiC/n-Ga$_2$O$_3$ heterojunction by inserting thin SiC barrier layer," *Applied Physics A*, vol. 122, pp. 1–5, 2016.

[126] T. Oshima, T. Okuno, N. Arai, N. Suzuki, H. Hino, and S. Fujita, "Flame detection by a β-Ga$_2$O$_3$ -based sensor," *Japanese Journal of Applied Physics*, vol. 48, no. 1R, p. 011605, 2009.

[127] X. Chen, K. Liu, Z. Zhang, C. Wang, B. Li, H. Zhao, D. Zhao, and D. Shen, "Self-powered solar-blind photodetector with fast response based on Au/β-Ga$_2$O$_3$ nanowires array film Schottky junction," *ACS applied materials & interfaces*, vol. 8, no. 6, pp. 4185–4191, 2016.

[128] X. Liu, C. Yue, C. Xia, and W. Zhang, "Characterization of vertical Au/β-Ga$_2$O$_3$ single-crystal Schottky photodiodes with MBE-grown high-resistivity epitaxial layer," *Chinese Physics B*, vol. 25, no. 1, p. 017201, 2015.

[129] A. M. Armstrong, M. H. Crawford, A. Jayawardena, A. Ahyi, and S. Dhar, "Role of self-trapped holes in the photoconductive gain of β-gallium oxide schottky diodes," *Journal of Applied Physics*, vol. 119, no. 10, 2016.

[130] B. Peng, L. Yuan, H. Zhang, H. Cheng, S. Zhang, Y. Zhang, Y. Zhang, and R. Jia, "Fast-response self-powered solar-blind photodetector based on Pt/β-Ga$_2$O$_3$ Schottky barrier diodes," *Optik*, vol. 245, p. 167715, 2021.

[131] T. Oshima, T. Okuno, N. Arai, N. Suzuki, S. Ohira, and S. Fujita, "Vertical solar-blind deep-ultraviolet Schottky photodetectors based on β-Ga$_2$O$_3$ substrates," *Applied physics express*, vol. 1, no. 1, p. 011202, 2008.

[132] S. Oh, C.-K. Kim, and J. Kim, "High responsivity β-Ga$_2$O$_3$ metal–semiconductor–metal solar-blind photodetectors with ultraviolet transparent graphene electrodes," *Acs Photonics*, vol. 5, no. 3, pp. 1123–1128, 2017.

[133] T. Oshima, T. Okuno, and S. Fujita, "Ga$_2$O$_3$ thin film growth on c-plane sapphire substrates by molecular beam epitaxy for deep-ultraviolet photodetectors," *Japanese Journal of Applied Physics*, vol. 46, no. 11R, p. 7217, 2007.

[134] X. Chen, Y. Xu, D. Zhou, S. Yang, F.-f. Ren, H. Lu, K. Tang, S. Gu, R. Zhang, Y. Zheng, and J. Ye, "Solar-blind photodetector with high avalanche gains and bias-tunable detecting functionality based on metastable phase α-Ga$_2$O$_3$/ZnO isotype heterostructures," *ACS applied materials & interfaces*, vol. 9, no. 42, pp. 36 997–37 005, 2017.

[135] H. Zhou, L. Cong, J. Ma, B. Li, M. Chen, H. Xu, and Y. Liu, "High gain broadband photoconductor based on amorphous Ga$_2$O$_3$ and suppression of persistent photoconductivity," *Journal of Materials Chemistry C*, vol. 7, no. 42, pp. 13 149–13 155, 2019.

[136] M. Chen, J. Ma, P. Li, H. Xu, and Y. Liu, "Zero-biased deep ultraviolet photodetectors based on graphene/cleaved (100) Ga$_2$O$_3$ heterojunction," *Optics Express*, vol. 27, no. 6, pp. 8717–8726, 2019.

[137] X. Qi, J. Yue, X. Ji, Z. Liu, S. Li, Z. Yan, M. Zhang, L. Yang, P. Li, D. Guo, Y. Guo, and W. Tang, "A deep-ultraviolet photodetector of a β-Ga$_2$O$_3$/CuBiI$_4$ heterojunction highlighting ultra-high sensitivity and responsivity," *Thin Solid Films*, vol. 757, p. 139397, 2022.

[138] W. Wang, Q. Yuan, D. Han, J. Sun, N. Liu, S. Hu, C. Liu, W. Zhang, and J. Ye, "High-temperature deep ultraviolet photodetector based on a crystalline Ga$_2$O$_3$-diamond heterostructure," *IEEE Electron Device Letters*, vol. 43, no. 12, pp. 2121–2124, 2022.

[139] S. Feng, Z. Liu, L. Feng, J. Wang, H. Xu, L. Deng, O. Zhou, X. Jiang, B. Liu, and X. Zhang, "High-performance self-powered ultraviolet photodetector based on Ga$_2$O$_3$/GaN heterostructure for optical imaging," *Journal of Alloys and Compounds*, vol. 945, p. 169274, 2023.

[140] S. Nakagomi, "Ultraviolet Photodetector Based on a Beta-Gallium Oxide/Nickel Oxide/Beta-Gallium Oxide Heterojunction Structure," *Sensors*, vol. 23, no. 19, p. 8332, 2023.

[141] L.-Y. Jian, H.-Y. Lee, and C.-T. Lee, "Ga$_2$O$_3$-based pin solar blind deep ultraviolet photodetectors," *Journal of Materials Science: Materials in Electronics*, vol. 30, pp. 8445–8448, 2019.

[142] H. Kan, W. Zheng, C. Fu, R. Lin, J. Luo, and F. Huang, "Ultrawide band gap oxide nan-odots (E g> 4.8 eV) for a high-performance deep ultraviolet photovoltaic detector," *ACS applied materials & interfaces*, vol. 12, no. 5, pp. 6030–6036, 2020.

[143] Y. Xu, X. Chen, Y. Zhang, F. Ren, S. Gu, and J. Ye, "Fast speed Ga_2O_3 solar-blind Schottky photodiodes with large sensitive area," *IEEE Electron Device Letters*, vol. 41, no. 7, pp. 997–1000, 2020.

[144] M. Labed, H. Kim, J. H. Park, M. Labed, A. Meftah, N. Sengouga, and Y. S. Rim, "Physical operations of a self-powered IZTO/β-Ga_2O_3 Schottky barrier diode photodetector," *Nanomaterials*, vol. 12, no. 7, p. 1061, 2022.

[145] L. Ye, S. Zhou, Y. Xiong, J. Tang, X. Wang, X. Li, D. Pang, H. Li, H. Zhang, L. Ye, Y. Cui, and W. Li, "Self-powered Pt/a-Ga_2O_3/ITO vertical Schottky junction solar-blind pho-todetector with excellent detection performance," *Optics Express*, vol. 31, no. 17, pp. 28 200–28 211, 2023.

[146] M. Labed, B.-I. Park, J. Kim, J. H. Park, J. Y. Min, H. J. Hwang, J. Kim, and Y. S. Rim, "Ul-trahigh Photoresponsivity of W/Graphene/β-Ga_2O_3 Schottky Barrier Deep Ultraviolet Photodiodes," *ACS nano*, vol. 18, no. 8, pp. 6558–6569, 2024.

[147] X. Liu, Q. Liu, B. Zhao, Y. Ren, B. Tao, and W. Zhang, "Comparison of β-Ga_2O_3 thin films grown on r-plane and c-plane sapphire substrates," *Vacuum*, vol. 178, p. 109435, 2020.

[148] W. Zhang, W. Wang, J. Zhang, T. Zhang, L. Chen, L. Wang, Y. Zhang, Y. Cao, L. Ji, and J. Ye, "Directional carrier transport in micrometer-thick gallium oxide films for high-performance deep-ultraviolet photodetection," *ACS Applied Materials & Interfaces*, vol. 15, no. 8, pp. 10 868–10 876, 2023.

[149] Y. Wang, H. Li, J. Cao, J. Shen, Q. Zhang, Y. Yang, Z. Dong, T. Zhou, Y. Zhang, W. Tang, and Z. Wu, "Ultrahigh gain solar blind avalanche photodetector using an amorphous Ga_2O_3-based heterojunction," *ACS nano*, vol. 15, no. 10, pp. 16 654–16 663, 2021.

[150] N. Li, Q. Zhang, Y. Yang, Y. Tang, T. Zhang, J. Shen, Y. Wang, F. Zhang, Y. Zhang, and Z. Wu, "Solar-blind avalanche photodetector based on epitaxial Ga_2O_3/$La_{0.8}Ca_{0.2}MnO_3$ pn heterojunction with ultrahigh gain," *Chinese Optics Letters*, vol. 21, no. 5, p. 051604, 2023.

[151] B. R. Tak, M.-M. Yang, M. Alexe, and R. Singh, "Deep-level traps responsible for per-sistent photocurrent in pulsed-laser-deposited β-Ga_2O_3 thin films," *Crystals*, vol. 11, no. 9, p. 1046, 2021.

[152] R. A. Miller, H. So, T. A. Heuser, and D. G. Senesky, "High-temperature ultraviolet pho-todetectors: a review," *arXiv preprint arXiv:1809.07396*, 2018.

[153] B. Poti, A. Passaseo, M. Lomascolo, R. Cingolani, and M. De Vittorio, "Persistent photocurrent spectroscopy of GaN metal–semiconductor–metal photodetectors on long time scale," *Applied physics letters*, vol. 85, no. 25, pp. 6083–6085, 2004.

[154] M. De Vittorio, B. poti, M. Todaro, M. Frassanito, A. Pomarico, A. Passaseo, M. Lomascolo, and R. Cingolani, "High temperature characterization of GaN-based photodetectors," *Sensors and Actuators A: Physical*, vol. 113, no. 3, pp. 329–333, 2004.

[155] J.-Y. Yue, X.-Q. Ji, S. Li, X.-H. Qi, P.-G. Li, Z.-P. Wu, and W.-H. Tang, "Dramatic reduction in dark current of β-Ga$_2$O$_3$ ultraviolet photodetectors via β-(Al$_{0.25}$Ga$_{0.75}$)$_2$O$_3$ surface passivation," *Chinese Physics B*, vol. 32, no. 1, p. 016701, 2023.

[156] A. Anhar Uddin Bhuiyan, Z. Feng, J. M. Johnson, Z. Chen, H.-L. Huang, J. Hwang, and H. Zhao, "MOCVD epitaxy of β-(Al$_x$Ga$_{1-x}$)$_2$O$_3$ thin films on (010) Ga$_2$O$_3$ substrates and N-type doping," *Applied Physics Letters*, vol. 115, no. 12, 2019.

[157] J. B. Varley, A. Perron, V. Lordi, D. Wickramaratne, and J. L. Lyons, "Prospects for n-type doping of (Al$_x$Ga$_{1-x}$)$_2$O$_3$ alloys," *Applied Physics Letters*, vol. 116, no. 17, 2020.

[158] F. Zhang, C. Hu, M. Arita, K. Saito, T. Tanaka, and Q. Guo, "Impacts of oxygen radical ambient on structural and optical properties of (AlGa)$_2$O$_3$ films deposited by pulsed laser deposition," *AIP Advances*, vol. 10, no. 6, 2020.

[159] R. Miller, F. Alema, and A. Osinsky, "Epitaxial β-Ga$_2$O$_3$ and β-(Al$_x$Ga$_{1-x}$)$_2$O$_3$/β-Ga$_2$O$_3$ Heterostructures Growth for Power Electronics," *IEEE Transactions on Semiconductor Manufacturing*, vol. 31, no. 4, pp. 467–474, 2018.

[160] T. Uchida, R. Jinno, S. Takemoto, K. Kaneko, and S. Fujita, "Evaluation of band alignment of α-Ga$_2$O$_3$/α-(Al$_x$Ga$_{1-x}$)$_2$O$_3$ heterostructures by X-ray photoelectron spectroscopy," *Japanese Journal of Applied Physics*, vol. 57, no. 4, p. 040314, 2018.

[161] X. Ma, R. Xu, Y. Mei, L. Ying, B. Zhang, and H. Long, "Crystalline anisotropy of β-Ga$_2$O$_3$ thin films on a c-plane GaN template and a sapphire substrate," *Semiconductor Science and Technology*, vol. 37, no. 3, p. 035003, 2022.

[162] C.-C. Yen, A. K. Singh, P.-W. Wu, H.-Y. Chou, and D.-S. Wuu, "Interface engineering in epitaxial growth of sputtered β-Ga$_2$O$_3$ films on Si substrates via TiN (111) buffer layer for Schottky barrier diodes," *Materials Today Advances*, vol. 17, p. 100348, 2023.

[163] H. Nishinaka, D. Tahara, and M. Yoshimoto, "Heteroepitaxial growth of ε-Ga$_2$O$_3$ thin films on cubic (111) MgO and (111) yttria-stablized zirconia substrates by mist chemical vapor deposition," *Japanese Journal of Applied Physics*, vol. 55, no. 12, p. 1202BC, 2016.

[164] Y. Chen, H. Liang, X. Xia, R. Shen, Y. Liu, Y. Luo, and G. Du, "Effect of growth pressure on the characteristics of β-Ga$_2$O$_3$ films grown on GaAs (100) substrates by MOCVD method," *Applied Surface Science*, vol. 325, pp. 258–261, 2015.

[165] B. Xu, J. Hu, J. Meng, X. He, X. Wang, and H. Pu, "Study of the Bonding Characteristics at β-Ga$_2$O$_3$ (201)/4H-SiC (0001) Interfaces from First Principles and Experiment," *Crystals*, vol. 13, no. 2, p. 160, 2023.

[166] W. Mi, J. Ma, C. Luan, and H. Xiao, "Structural and optical properties of β-Ga$_2$O$_3$ films deposited on MgAl$_2$O$_4$ (100) substrates by metal–organic chemical vapor deposition," *Journal of luminescence*, vol. 146, pp. 1–5, 2014.

[167] H. Sun, C. Torres Castanedo, K. Liu, K.-H. Li, W. Guo, R. Lin, X. Liu, J. Li, and X. Li, "Valence and conduction band offsets of β-Ga$_2$O$_3$/AlN heterojunction," *Applied Physics Letters*, vol. 111, no. 16, 2017.

[168] S.-M. Sun, W.-J. Liu, D. A. Golosov, C.-J. Gu, and S.-J. Ding, "Investigation of energy band at atomic layer deposited AZO/β-Ga$_2$O$_3$ ($\bar{2}$01) heterojunctions," *Nanoscale Research Letters*, vol. 14, pp. 1–6, 2019.

[169] M. Kneiß, A. Hassa, D. Splith, C. Sturm, H. Von Wenckstern, T. Schultz, N. Koch, M. Lorenz, and M. Grundmann, "Tin-assisted heteroepitaxial PLD-growth of κ-Ga$_2$O$_3$ thin films with high crystalline quality," *APL Materials*, vol. 7, no. 2, 2019.

[170] Y. Cheng, C. Zhang, Y. Xu, Z. Li, D. Chen, W. Zhu, Q. Feng, S. Xu, J. Zhang, and Y. Hao, "Heteroepitaxial growth of β-Ga$_2$O$_3$ thin films on c-plane sapphire substrates with β-(Al$_x$Ga$_{1-x}$)$_2$O$_3$ intermediate buffer layer by mist-CVD method," *Materials Today Communications*, vol. 29, p. 102766, 2021.

[171] J. Zyss, *Molecular nonlinear optics: materials, physics, and devices.* Academic press, 2013.

[172] K. Choi and H. Kang, "Structural and optical evolution of Ga$_2$O$_3$/glass thin films deposited by radio frequency magnetron sputtering," *Materials Letters*, vol. 123, pp. 160–164, 2014.

[173] X. Feng, Z. Li, W. Mi, and J. Ma, "Effect of annealing on the properties of Ga$_2$O$_3$: Mg films prepared on α-Al$_2$O$_3$ (0001) by MOCVD," *Vacuum*, vol. 124, pp. 101–107, 2016.

[174] S.-Y. Ting, P.-J. Chen, H.-C. Wang, C.-H. Liao, W.-M. Chang, Y.-P. Hsieh, and C. Yang, "Crystallinity improvement of ZnO thin film on different buffer layers grown by MBE," *Journal of Nanomaterials*, vol. 2012, no. 1, p. 929278, 2012.

Bibliography

[175] M. Liu, D. Bi, B. Man, D. Kong, and X. Xu, "Effects of CdZnTe buffer layer thickness on properties of HgCdTe thin film grown by pulsed laser deposition," *Applied surface science*, vol. 264, pp. 522–526, 2013.

[176] J. Huang, B. Li, Y. Ma, K. Tang, H. Huang, Y. Hu, T. Zou, and L. Wang, "Effect of Homo-buffer Layers on the Properties of Sputtering Deposited Ga_2O_3 Films," in *IOP Conference Series: Materials Science and Engineering*, vol. 362, no. 1. IOP Publishing, 2018, p. 012003.

[177] C. Gao, Y. Wang, S. Fu, D. Xia, Y. Han, J. Ma, H. Xu, B. Li, A. Shen, and Y. Liu, "High-Performance Solar-Blind Ultraviolet Photodetectors Based on β-Ga_2O_3 Thin Films Grown on p-Si (111) Substrates with Improved Material Quality via an AlN Buffer Layer Introduced by Metal–Organic Chemical Vapor Deposition," *ACS Applied Materials & Interfaces*, vol. 15, no. 32, pp. 38 612–38 622, 2023.

[178] Y.-K. Su, Y.-Z. Chiou, F.-S. Juang, S.-J. Chang, and J.-K. Sheu, "GaN and InGaN metal-semiconductor-metal photodetectors with different Schottky contact metals," *Japanese Journal of Applied Physics*, vol. 40, no. 4S, p. 2996, 2001.

[179] T. M. H. Nguyen, M. H. Tran, and C. W. Bark, "Deep-ultraviolet transparent electrode design for high-performance and self-powered perovskite photodetector," *Nanomaterials*, vol. 13, no. 22, p. 2979, 2023.

[180] M.-L. Tu, Y.-K. Su, S.-J. Chang, and R. W. Chuang, "GaN UV photodetector by using transparency antimony-doped tin oxide electrode," *Journal of crystal growth*, vol. 298, pp. 744–747, 2007.

[181] Y. Song, W. Fang, R. Brenes, and J. Kong, "Challenges and opportunities for graphene as transparent conductors in optoelectronics," *Nano Today*, vol. 10, no. 6, pp. 681–700, 2015.

[182] X. Wang and X. Gan, "Graphene integrated photodetectors and opto-electronic devices—a review," *Chinese Physics B*, vol. 26, no. 3, p. 034203, 2017.

[183] E. Kus, D. Özkendir, V. Fırat, C. Çelebi *et al.*, "Epitaxial graphene contact electrode for silicon carbide based ultraviolet photodetector," *Journal of Physics D: Applied Physics*, vol. 48, no. 9, p. 095104, 2015.

[184] S. Dhar, T. Majumder, and S. P. Mondal, "Graphene quantum dot-sensitized ZnO nanorod/polymer Schottky junction UV detector with superior external quantum efficiency, detectivity, and responsivity," *ACS Applied Materials & Interfaces*, vol. 8, no. 46, pp. 31 822–31 831, 2016.

Bibliography

[185] N. Watanabe, T. Kimoto, and J. Suda, "4H-SiC pn photodiodes with temperature-independent photoresponse up to 300°C ," *Applied Physics Express*, vol. 5, no. 9, p. 094101, 2012.

[186] S. Salvatori, M. Rossi, F. Scotti, G. Conte, F. Galluzzi, and V. Ralchenko, "High-temperature performances of diamond-based UV-photodetectors," *Diamond and Related Materials*, vol. 9, no. 3-6, pp. 982–986, 2000.

[187] L. Sang, M. Liao, Y. Koide, and M. Sumiya, "High-temperature ultraviolet detection based on InGaN Schottky photodiodes," *Applied Physics Letters*, vol. 99, no. 3, 2011.

[188] C. Yang, H. Liang, Z. Zhang, X. Xia, H. Zhang, R. Shen, Y. Luo, and G. Du, "Effect of temperature on photoresponse properties of solar-blind Schottky barrier diode photodetector based on single crystal Ga_2O_3," *Chinese Physics B*, vol. 28, no. 4, p. 048502, 2019.

[189] B. Tak, M. Garg, S. Dewan, C. G. Torres-Castanedo, K.-H. Li, V. Gupta, X. Li, and R. Singh, "High-temperature photocurrent mechanism of β-Ga_2O_3 based metal-semiconductor-metal solar-blind photodetectors," *Journal of Applied Physics*, vol. 125, no. 14, 2019.

[190] R. Zou, Z. Zhang, Q. Liu, J. Hu, L. Sang, M. Liao, and W. Zhang, "High detectivity solar-blind high-temperature deep-ultraviolet photodetector based on multi-layered (100) facet-oriented β-Ga_2O_3 nanobelts," *Small*, vol. 10, no. 9, pp. 1848–1856, 2014.

[191] Y. Li, D. Zhang, R. Lin, Z. Zhang, W. Zheng, and F. Huang, "Graphene interdigital electrodes for improving sensitivity in a Ga_2O_3: Zn deep-ultraviolet photoconductive detector," *ACS applied materials & interfaces*, vol. 11, no. 1, pp. 1013–1020, 2018.

[192] L. Sang, M. Liao, and M. Sumiya, "A comprehensive review of semiconductor ultraviolet photodetectors: from thin film to one-dimensional nanostructures," *Sensors*, vol. 13, no. 8, pp. 10 482–10 518, 2013.

[193] H.-t. Zhou, L.-j. Cong, J.-g. Ma, M.-z. Chen, D.-y. Song, H.-b. Wang, P. Li, B.-s. Li, H.-y. Xu, and Y.-c. Liu, "High-performance high-temperature solar-blind photodetector based on polycrystalline Ga_2O_3 film," *Journal of Alloys and Compounds*, vol. 847, p. 156536, 2020.

[194] Y. Chen, Y. Lu, M. Liao, Y. Tian, Q. Liu, C. Gao, X. Yang, and C. Shan, "3D solar-blind Ga_2O_3 photodetector array realized via origami method," *Advanced Functional Materials*, vol. 29, no. 50, p. 1906040, 2019.

[195] N. DasGupta and A. DasGupta, *Semiconductor devices: modelling and technology*. PHI Learning Pvt. Ltd., 2004.

Bibliography

[196] W. Spicer, P. Chye, C. Garner, I. Lindau, and P. Pianetta, "The surface electronic structure of 3–5 compounds and the mechanism of Fermi level pinning by oxygen (passivation) and metals (Schottky barriers)," *Surface Science*, vol. 86, pp. 763–788, 1979.

[197] S. M. Sze, Y. Li, and K. K. Ng, *Physics of semiconductor devices.* John wiley & sons, 2021.

[198] T. Goudon, V. Miljanović, and C. Schmeiser, "On the Shockley–Read–Hall model: generation-recombination in semiconductors," *SIAM Journal on Applied Mathematics*, vol. 67, no. 4, pp. 1183–1201, 2007.

[199] S. Selberherr, *Analysis and simulation of semiconductor devices.* Springer Science & Business Media, 2012.

[200] J. Dziewior and W. Schmid, "Auger coefficients for highly doped and highly excited silicon," *Applied Physics Letters*, vol. 31, no. 5, pp. 346–348, 1977.

[201] A. Latreche, "Combined thermionic emission and tunneling mechanisms for the analysis of the leakage current for Ga_2O_3 Schottky barrier diodes," *SN Applied Sciences*, vol. 1, no. 2, p. 188, 2019.

[202] M. J. Tadjer, V. D. Wheeler, D. I. Shahin, C. R. Eddy, and F. J. Kub, "Thermionic emission analysis of TiN and Pt Schottky contacts to β-Ga_2O_3," *ECS Journal of Solid State Science and Technology*, vol. 6, no. 4, p. P165, 2017.

[203] H. Kim, S. Kyoung, T. Kang, J.-Y. Kwon, K. H. Kim, and Y. S. Rim, "Effective surface diffusion of nickel on single crystal β-Ga_2O_3 for Schottky barrier modulation and high thermal stability," *Journal of Materials Chemistry C*, vol. 7, no. 35, pp. 10 953–10 960, 2019.

[204] B. Roul, M. Kumar, M. K. Rajpalke, T. N. Bhat, and S. Krupanidhi, "Binary group III-nitride based heterostructures: band offsets and transport properties," *Journal of Physics D: Applied Physics*, vol. 48, no. 42, p. 423001, 2015.

[205] R. Lingaparthi, K. Sasaki, Q. T. Thieu, A. Takatsuka, F. Otsuka, S. Yamakoshi, and A. Kuramata, "Surface related tunneling leakage in β-Ga_2O_3 (001) vertical Schottky barrier diodes," *Applied Physics Express*, vol. 12, no. 7, p. 074008, 2019.

[206] K.-H. Kao, A. S. Verhulst, W. G. Vandenberghe, B. Soree, G. Groeseneken, and K. De Meyer, "Direct and indirect band-to-band tunneling in germanium-based TFETs," *IEEE Transactions on Electron Devices*, vol. 59, no. 2, pp. 292–301, 2011.

Bibliography

[207] F. E. Mamouni, S. K. Dixit, R. D. Schrimpf, P. C. Adell, I. S. Esqueda, M. L. McLain, H. J. Barnaby, S. Cristoloveanu, and W. Xiong, "Gate-length and drain-bias dependence of band-to-band tunneling-induced drain leakage in irradiated fully depleted SOI devices," *IEEE Transactions on Nuclear Science*, vol. 55, no. 6, pp. 3259–3264, 2008.

[208] I. Silvaco, "Atlas user's manual," *Santa Clara, CA, Ver*, vol. 5, 2011.

[209] D. B. Klaassen, "A unified mobility model for device simulation—I. Model equations and concentration dependence," *Solid-State Electronics*, vol. 35, no. 7, pp. 953–959, 1992.

[210] S. Rafique, L. Han, S. Mou, and H. Zhao, "Temperature and doping concentration dependence of the energy band gap in β-Ga$_2$O$_3$ thin films grown on sapphire," *Optical Materials Express*, vol. 7, no. 10, pp. 3561–3570, 2017.

[211] S. Jain and D. Roulston, "A simple expression for band gap narrowing (BGN) in heavily doped Si, Ge, GaAs and Ge$_x$Si$_{1-x}$ strained layers," *Solid-State Electronics*, vol. 34, no. 5, pp. 453–465, 1991.

[212] J. Roldán, F. Gámiz, J. López-Villanueva, J. Carceller, and P. Cartujo, "The dependence of the electron mobility on the longitudinal electric field in MOSFETs," *Semiconductor science and technology*, vol. 12, no. 3, p. 321, 1997.

[213] W. Joyce and R. Dixon, "Analytic approximations for the Fermi energy of an ideal Fermi gas," *Applied Physics Letters*, vol. 31, no. 5, pp. 354–356, 1977.

[214] T. Hatakeyama, J. Nishio, C. Ota, and T. Shinohe, "Physical modeling and scaling properties of 4H-SiC power devices," in *2005 International Conference On Simulation of Semiconductor Processes and Devices*. IEEE, 2005, pp. 171–174.

[215] M. Labed, N. Sengouga, M. Labed, A. Meftah, S. Kyoung, H. Kim, and Y. S. Rim, "Modeling a Ni/β-Ga$_2$O$_3$ Schottky barrier diode deposited by confined magnetic-field-based sputtering," *Journal of Physics D: Applied Physics*, vol. 54, no. 11, p. 115102, 2021.

[216] Z. Hu, Q. Feng, J. Zhang, F. Li, X. Li, Z. Feng, C. Zhang, and Y. Hao, "Optical properties of (Al$_x$Ga$_{1-x}$)$_2$O$_3$ on sapphire," *Superlattices and microstructures*, vol. 114, pp. 82–88, 2018.

[217] B. Shankar, S. K. Gupta, W. R. Taube, and J. Akhtar, "Dependence of field plate parameters on dielectric constant in a 4H-SiC Schottky diode," in *2014 IEEE 2nd International Conference on Emerging Electronics (ICEE)*. IEEE, 2014, pp. 1–3.

[218] H. Liu, A. Deshmukh, N. Salowitz, J. Zhao, and K. Sobolev, "Resistivity signature of graphene-based fiber-reinforced composite subjected to mechanical loading," *Frontiers in Materials*, vol. 9, p. 818176, 2022.

Bibliography

[219] M. Dadashbeik, D. Fathi, and M. Eskandari, "Design and simulation of perovskite solar cells based on graphene and TiO_2/graphene nanocomposite as electron transport layer," *Solar Energy*, vol. 207, pp. 917–924, 2020.

[220] A. Polyakov, I.-H. Lee, N. Smirnov, E. Yakimov, I. Shchemerov, A. Chernykh, A. Kochkova, A. Vasilev, P. Carey, F. Ren *et al.*, "Defects at the surface of β-Ga_2O_3 produced by Ar plasma exposure," *APL Materials*, vol. 7, no. 6, 2019.

[221] M. Labed, N. Sengouga, and Y. S. Rim, "Control of Ni/β-Ga_2O_3 vertical Schottky diode output parameters at forward bias by insertion of a graphene layer," *Nanomaterials*, vol. 12, no. 5, p. 827, 2022.

[222] M. Kato, S. Tanaka, M. Ichimura, E. Arai, S. Nakamura, T. Kimoto, and R. Pässler, "Optical cross sections of deep levels in 4H-SiC," *Journal of applied physics*, vol. 100, no. 5, 2006.

[223] Y. Sui, H. Liang, W. Huo, Y. Wang, and Z. Mei, "A flexible and transparent β-Ga_2O_3 solar-blind ultraviolet photodetector on mica," *Journal of Physics D: Applied Physics*, vol. 53, no. 50, p. 504001, 2020.

[224] B. R. Tak, V. Gupta, A. K. Kapoor, Y.-H. Chu, and R. Singh, "Wearable gallium oxide solar-blind photodetectors on muscovite mica having ultrahigh photoresponsivity and detectivity with added high-temperature functionalities," *ACS Applied Electronic Materials*, vol. 1, no. 11, pp. 2463–2470, 2019.

[225] Y. Qin, S. Long, H. Dong, Q. He, G. Jian, Y. Zhang, X. Hou, P. Tan, Z. Zhang, H. Lv, Q. Liu, and M. Liu, "Review of deep ultraviolet photodetector based on gallium oxide," *Chinese Physics B*, vol. 28, no. 1, p. 018501, 2019.

[226] J.-W. Oh, C. Lee, and N. Kim, "The effect of trap density on the space charge formation in polymeric photorefractive composites," *The Journal of chemical physics*, vol. 130, no. 13, 2009.

[227] H. Peelaers, J. B. Varley, J. S. Speck, and C. G. Van de Walle, "Structural and electronic properties of Ga_2O_3-Al_2O_3 alloys," *Applied Physics Letters*, vol. 112, no. 24, 2018.

[228] R. Cherroun, A. Meftah, M. Labed, N. Sengouga, A. Meftah, H. Kim, and Y. S. Rim, "Study of a solar-blind photodetector based on an IZTO/β-Ga_2O_3/ITO Schottky diode," *Journal of Electronic Materials*, vol. 52, no. 2, pp. 1448–1460, 2023.

[229] R. Cherroun, A. Meftah, N. Sengouga, M. Labed, H. Kim, Y. S. Rim, A. Djemaa, and A. Meftah, "Improvement of β-Ga_2O_3-based Schottky barrier UV photodetector by 4H-SiC substrate, intrinsic buffer layer, and graphene surface contact," *Journal of Materials Science: Materials in Electronics*, vol. 35, no. 16, pp. 1–19, 2024.

Bibliography

[230] C.-C. Yen, T.-M. Huang, P.-W. Chen, K.-P. Chang, W.-Y. Wu, and D.-S. Wuu, "Role of interfacial oxide in the preferred orientation of Ga_2O_3 on Si for deep ultraviolet photodetectors," *ACS omega*, vol. 6, no. 43, pp. 29 149–29 156, 2021.

[231] S. Nakagomi, T.-a. Sato, Y. Takahashi, and Y. Kokubun, "Deep ultraviolet photodiodes based on the β-Ga_2O_3/GaN heterojunction," *Sensors and Actuators A: Physical*, vol. 232, pp. 208–213, 2015.

[232] Y. Qu, Z. Wu, M. Ai, D. Guo, Y. An, H. Yang, L. Li, and W. Tang, "Enhanced Ga_2O_3/SiC ultraviolet photodetector with graphene top electrodes," *Journal of Alloys and Compounds*, vol. 680, pp. 247–251, 2016.

[233] R. Wei, S. Song, K. Yang, Y. Cui, Y. Peng, X. Chen, X. Hu, and X. Xu, "Thermal conductivity of 4H-SiC single crystals," *Journal of Applied Physics*, vol. 113, no. 5, 2013.

[234] T. Kimoto, "High-voltage SiC power devices for improved energy efficiency," *Proceedings of the Japan Academy, Series B*, vol. 98, no. 4, pp. 161–189, 2022.

[235] K. Lin, D. Li, S. Song, Z. Ye, W. Jiang, and Q. H. Qin, "Enhanced mechanical properties of 4H-SiC by epitaxial carbon films obtained from bilayer graphene," *Nanotechnology*, vol. 31, no. 19, p. 195702, 2020.

[236] D. Nath, P. Dey, A. M. Joseph, J. K. Rakshit, and J. N. Roy, "Photocurrent generation under forward bias with interfacial tunneling of carrier at pentacene/F_{16}CuPc heterojunction photodetector," *Journal of Alloys and Compounds*, vol. 815, p. 152401, 2020.

[237] V. Dhyani and S. Das, "High-speed scalable silicon-MoS_2 PN heterojunction photodetectors," *Scientific reports*, vol. 7, no. 1, pp. 1–9, 2017.

[238] B. Zippelius, J. Suda, and T. Kimoto, "High temperature annealing of n-type 4H-SiC: Impact on intrinsic defects and carrier lifetime," *Journal of Applied Physics*, vol. 111, no. 3, 2012.

[239] J. Beattie, J. Goss, M. Rayson, and P. Briddon, "Structure and electron affinity of the 4H–SiC (0001) surfaces: a methodological approach for polar systems," *Journal of Physics: Condensed Matter*, vol. 33, no. 16, p. 165003, 2021.

[240] W.-C. Yang, B. J. Rodriguez, A. Gruverman, and R. Nemanich, "Polarization-dependent electron affinity of $LiNbO_3$ surfaces," *Applied Physics Letters*, vol. 85, no. 12, pp. 2316–2318, 2004.

[241] G. Pfusterschmied, F. Triendl, M. Schneider, and U. Schmid, "Impact of Ar^+ bombardment of 4H–SiC substrates on Schottky diode barrier heights," *Materials Science in Semiconductor Processing*, vol. 123, p. 105504, 2021.

[242] J.-H. Chen, C. Jang, S. Xiao, M. Ishigami, and M. S. Fuhrer, "Intrinsic and extrinsic performance limits of graphene devices on SiO_2," *Nature nanotechnology*, vol. 3, no. 4, pp. 206–209, 2008.

[243] S. Morozov, K. Novoselov, M. Katsnelson, F. Schedin, D. C. Elias, J. A. Jaszczak, and A. Geim, "Giant intrinsic carrier mobilities in graphene and its bilayer," *Physical review letters*, vol. 100, no. 1, p. 016602, 2008.

[244] T. M. Tritt, *Thermal conductivity: theory, properties, and applications.* Springer Science & Business Media, 2005.

[245] S. J. Kim, K. Choi, B. Lee, Y. Kim, and B. H. Hong, "Materials for flexible, stretchable electronics: graphene and 2D materials," *Annual Review of Materials Research*, vol. 45, no. 1, pp. 63–84, 2015.

[246] V. Berry, "Impermeability of graphene and its applications," *Carbon*, vol. 62, pp. 1–10, 2013.

[247] E. Rut'kov, E. Afanas' eva, and N. Gall, "Graphene and graphite work function depending on layer number on Re," *Diamond and Related Materials*, vol. 101, p. 107576, 2020.

[248] B. Chen, Y. Yang, X. Xie, N. Wang, Z. Ma, K. Song, and X. Zhang, "Analysis of temperature-dependent characteristics of a 4H-SiC metal-semiconductor-metal ultraviolet photodetector," *Chinese Science Bulletin*, vol. 57, pp. 4427–4433, 2012.

[249] Y. Xu, D. Zhou, H. Lu, D. Chen, F. Ren, R. Zhang, and Y. Zheng, "High-temperature and reliability performance of 4H-SiC Schottky-barrier photodiodes for UV detection," *Journal of Vacuum Science & Technology B*, vol. 33, no. 4, 2015.

[250] A. Aldalbahi and P. Feng, "Development of 2-D boron nitride nanosheets UV photoconductive detectors," *IEEE Transactions on Electron Devices*, vol. 62, no. 6, pp. 1885–1890, 2015.

[251] A. F. Zhou, A. Aldalbahi, and P. Feng, "Vertical metal-semiconductor-metal deep UV photodetectors based on hexagonal boron nitride nanosheets prepared by laser plasma deposition," *Optical Materials Express*, vol. 6, no. 10, pp. 3286–3292, 2016.

[252] A. Aldalbahi, E. Li, M. Rivera, R. Velazquez, T. Altalhi, X. Peng, and P. X. Feng, "A new approach for fabrications of SiC based photodetectors," *Scientific Reports*, vol. 6, no. 1, p. 23457, 2016.

Publications and conferences

➤ Rima Cherroun, Afak Meftah, Madani Labed, Nouredine Sengouga, Amjad Meftah, Hojoong Kim, You Seung Rim. "Study of a Solar Blind Photodetector Based on an IZTO/β-Ga$_2$O$_3$/ITO Schottky Diode." *Journal of Electronic Materials*, 2022.
https://doi.org/10.1007/s11664-022-10081-3.

➤ Rima Cherroun, Afak Meftah, Nouredine Sengouga, Madani Labed, Hojoong Kim, You Seung Rim, Attafi Djemaa, Amjad Meftah. "Improvement of β-Ga$_2$O$_3$ based Schottky barrier UV photodetector by 4H SiC substrate, intrinsic buffer layer, and graphene surface contact." *Journal of Materials Science: Materials in Electronics*, 2024.
https://doi.org/10.1007/s10854-024-12786-z.

● Certificate of participation at the first international conference on materials science and application February 8-9 2023 Khenchela Algeria.

● Certificate of participation in the 3rd National Conference on Applied Physics and Chemistry, March 12-13, 2023, Laghouat, Algeria.

● Certificate of participation in the 4th International Cappadocia Scientific Research Congress, April 16-17, 2023, Cappadocia-Nevsehir, Turkey, organized by IKSAD Institute.

● Certificate of participation in the 7th international student's science congress on 12-13 May 2023 at Izmir University.

ORIGINAL RESEARCH ARTICLE

Study of a Solar-Blind Photodetector Based on an IZTO/β-Ga$_2$O$_3$/ITO Schottky Diode

Rima Cherroun[1] · Afak Meftah[1] · Madani Labed[1] · Nouredine Sengouga[1] · Amjad Meftah[1] · Hojoong Kim[2] · You Seung Rim[2]

Abstract

An InZnSnO$_2$ (IZTO)/β-Ga$_2$O$_3$ solar blind Schottky barrier diode photodetector (PhD) exposed to 255 nm, 385 nm and 500 nm light wavelengths was simulated and compared with measurement. The measured dark photocurrent at reverse bias and responsivity were successfully reproduced by numerical simulation by considering several factors such as conduction mechanisms and material parameters. Further optimizations based on reducing trap densities and insertion of a 50-nm $(Al_{0.39}Ga_{0.61})_2O_3$ passivation layer between IZTO and β-Ga$_2$O$_3$ are carried out. The effect of reducing bulk traps densities on the photocurrent, responsivity and time-dependent photoresponse (persistent conductivity) were studied. With decreasing traps densities, the photocurrent increased. Responsivity reached 0.04 A/W for low β-Ga$_2$O$_3$ trap densities. The decay time estimated for the lowest E_T (0.74, 1.04 eV) densities is ~ 0.05 s and is shorter at ~ 0.015 s for E_T (0.55 eV). This indicates that the shallowest traps had the dominant influence ($E_T = 0.55$ eV) on the persistent photoconductivity phenomenon. Furthermore, with decreasing trap densities, this PhD can be considered as a self-powered solar-blind photodiode (SBPhD). The insertion of a $(Al_{0.39}Ga_{0.61})_2O_3$ passivation layer increases the photocurrent which is related to a recombination decrease and the photogenerated carrier increase, and hence the increase of the internal quantum efficiency.

Keywords IZTO/β-Ga$_2$O$_3$ · solar-blind photodetector · persistent photoconductivity · $(Al_{0.39}Ga_{0.61})_2O_3$ passivation · simulation · traps

Introduction

Deep ultraviolet photodetectors (DUV PDs) based on wide-band gap semiconductors such as GaN, SiC, diamond, BN, Al$_x$Ga$_{1-x}$N, LaAlO$_3$, In$_2$Ge$_2$O$_7$, ZnMgO and many others[1-10] have been developed, showing natural solar blindness and very low dark current owing to their wide band gap, low permittivity, high electron saturation velocity and radiation resistance.[6] A number of works have studied

the appropriateness of the abovementioned materials that have proved a selectivity and absorption ability in the DUV region (190–350 nm).[7,11] Among the studied materials for photodetector devices, Al$_x$Ga$_{1-x}$N[12] and Mg$_x$Zn$_{1-x}$O[13] ternary semiconductor alloys were investigated.[14] However, the high-quality epitaxial growth of Al$_x$Ga$_{1-x}$N needs a critical growth temperature above 1350°C.[16,15] Mg$_x$Zn$_{1-x}$O with a Mg composition of over 33% undergoes phase segregation from wurtzite to rocksalt structure[9] which induces defects and reduces the detecting efficiency. Diamond material is not preferred since it is largely expensive, its band gap engineering is difficult[16,17] and there is a lack of large-area single-crystal diamond bulk material.[18] One-dimensional (1D) nanostructured UV detectors have attracted attention due to the good sensitivity to light resulting from their large surface-to-volume ratio, but as a result of the dominance of the surface photocurrent and the high-temperature of UV detectors based on the nanostructured semiconductors they may face difficult situations, and hence, bulk-dominated photocurrents are preferred.[19]

✉ Nouredine Sengouga
n.sengouga@univ-biskra.dz

✉ You Seung Rim
youseung@sejong.ac.kr

[1] Laboratory of Semiconducting and Metallic Materials (LMSM), University of Biskra, Biskra 07000, Algeria

[2] Department of Intelligent Mechatronics Engineering and Convergence Engineering for Intelligent Drone, Sejong University, 209 Neungdong-ro, Gwangjin-gu, Seoul 05006, Republic of Korea

Improvement of β-Ga$_2$O$_3$-based Schottky barrier UV photodetector by 4H-SiC substrate, intrinsic buffer layer, and graphene surface contact

Rima Cherroun[1], Afak Meftah[1,*], Nouredine Sengouga[1], Madani Labed[2], Hojoong Kim[2], You Seung Rim[2,3], Afaf Djemaa[1], and Amjad Meftah[1]

[1] *Laboratory of Semiconducting and Metallic Materials (LMSM), University of Biskra, 07000 Biskra, Algeria*
[2] *Department of Intelligent Mechatronics Engineering and Convergence Engineering for Intelligent Drone, Sejong University, 209 Neungdong-ro, Gwangjin-gu, Seoul 05006, Republic of Korea*
[3] *Institute of Semiconductor and System IC, Sejong University, Seoul 05006, Republic of Korea*

ABSTRACT

This work presents a study of a β-Ga$_2$O$_3$-based Schottky barrier UV photodetector (SB UV-PD) with careful concern for material properties, device structure, and optimization techniques. The initial is IZTO/β-Ga$_2$O$_3$/ITO was calibrated with experimental measurement. The optimization process lies in these three points: using Silicon Carbide (4H-SiC) as substrate, employing a 4H-SiC intrinsic buffer layer, between Ga$_2$O$_3$-Si and the 4H-SiC substrate, and using of graphene instead of IZTO as top Schottky contact. The analysis is based on the current density–voltage (J–V) characteristics, responsivity, internal quantum efficiency (IQE), and time-dependent photo-response (T – $DPhR$). The optimization process was carried out by fine-tuning various parameters like traps in the 4H-SiC, the 4H-SiC buffer layer electronic affinity, and the top contact graphene work function. The best obtained parameters of photocurrent density, responsivity, IQE, and detectivity are 7.38×10^{-5} A/cm^2, 0.074 A/W, 0.57, 5×10^{12} Jones at -1 V under 255 nm, respectively.

1 Introduction

Gallium oxide (Ga$_2$O$_3$) is known for its notable characteristics, including an ultra-wide band gap ranging from 4.6 to 4.9 eV, an electrical breakdown field intensity of 8 MV/cm, and a high saturation velocity of 1×10^7 cm/s [1]. The material possesses economic efficiency, high resistance to radiation, and chemical and thermal stability, enabling its functionality in harsh conditions [2, 3]. It is considered a significant solar-blind UV photodetector and is classified as a novel addition to the third generation of semiconductors [3]. Its applications span various domains such as high-temperature event monitoring, counter-terrorism, security, ad hoc network communications, and numerous other fields [4]. The high band gap of Ga$_2$O$_3$ enables improved detection of UV light by reducing its absorption limit edge to below 280 nm, accompanied

⌖ Springer

First International Conference on Materials Science and Applications — ICMSA 2023

Certificate of Participation

This Certification of participation is presented to

Rima cherroun

Co-authors: Afak Meftah

Was presented as a **Online poster presentation** at the First International Conference on Materials Science and Applications ICMSA'23 (Hybrid), held in February 08th to 09th, 2023 at Khenchela University (Algeria)

Title of the presentation: **Study effect whoever metal work-function and power density of light and bulk defect on IZTO/β-Ga2O3 Schottky photodetector by Silvaco-Atlas**

General Chair
Dr. ROGUAI Sabrina

General Chair

Certificate
of Participation

الملتقى الوطني الثالث للفيزياء والكيمياء

This certificate is awarded to **Rima Cherroun**
For participation in **3rd** National Conference **on** Applied **Physics & Chemistry** (3rdNCAPC23) held on March 12th &13th, 2023 in Laghouat
For speaking on **Modeling and analysis simulation of Schottky Diode based on an IZTO/β-Ga2O3/ITO**
Co-authors: Afak Meftah

3rdNCAPC23 chairman
Dr. KAOUKA ALA EDDINE

https:// ncapc23enslaghouat/

133

Publications and conferences

134